creative commons
COMMONS DEED

저작자표시 2.0 대한민국

이용자는 아래의 조건을 따르는 경우에 한하여 자유롭게

- 이 저작물을 복제, 배포, 전송, 전시, 공연 및 방송할 수 있습니다.
- 이차적 저작물을 작성할 수 있습니다.
- 이 저작물을 영리 목적으로 이용할 수 있습니다.

다음과 같은 조건을 따라야 합니다:

**저작자표시**. 귀하는 원저작자를 표시하여야 합니다.

- 귀하는, 이 저작물의 재이용이나 배포의 경우, 이 저작물에 적용된 이용허락조건을 명확하게 나타내어야 합니다.
- 저작권자로부터 별도의 허가를 받으면 이러한 조건들은 적용되지 않습니다.

**저작권법에 따른 이용자의 권리는 위의 내용에 의하여 영향을 받지 않습니다.**

이것은 이용허락규약(Legal Code)을 이해하기 쉽게 요약한 것입니다.

Disclaimer

dCollection

이학박사학위 논문

# Studies on magnetoelectric effects in $Fe_3O_4$ nanoparticles and $S = 1/2$ frustrated spin systems

## $Fe_3O_4$ 나노입자와 $S$=1/2 쩔쩔매는 스핀시스템에서의 자기전기 효과에 관한 연구

2017년 8월

서울대학교 대학원

물리천문학부

유 경 준

# Studies on magnetoelectric effects in $Fe_3O_4$ nanoparticles and $S = 1/2$ frustrated spin systems

지도 교수 김 기 훈

이 논문을 이학박사 학위논문으로 제출함
2017년 8월

서울대학교 대학원
물리천문학부
유 경 준

유경준의 이학박사 학위논문을 인준함
2017년 8월

위 원 장 노 태 원 (인)

부위원장 김 기 훈 (인)

위 원 최 석 봉 (인)

위 원 양 범 정 (인)

위 원 장 지 훈 (인)

# Abstract

Magnetoelectric (ME) effect is the phenomenon in which the electric polarization (*P*) is controlled by magnetic field (*H*) or the magnetization is controlled by electric field. From early 2000s, the magneto-electric properties have attracted tremendous interest due to fundamental interests on the physics of ferroelectricity induced by spin order and great application potential for numerous low-power electronic devices. Therefore, thousands of reports on extensive experimental results and theoretical models have well established the understandings on the ME effect. However, there has been lack of extensive and quantitative investigations on the ME effect in nano-sized particles and spin $S = 1/2$ systems in which the high quantum effects are expected.

In this thesis, I focus on the nanoparticles of $Fe_3O_4$ and two new discovered ME materials with $Cu^{2+}$ ($S = 1/2$) ions, $PbCu_3TeO_7$ and $Cu_3TeO_6$. First, we investigate quantitatively the magnetoelectric coupling of spherical $Fe_3O_4$ nanoparticles with uniform diameters from 3 to 15 nm embedded in an insulating host, using a sensitive ME susceptometer. The intrinsic ME susceptibility is measured, exhibiting a maximum value of ~0.6 ps/m at 5 K for $d = 15$ nm. We found that the ME susceptibility is reduced with reduced $d$ but remains finite until $d = \sim 5$ nm, which is close to the critical thickness for observing the Verwey transition. Moreover, with reduced diameter the critical temperature below which the ME susceptibility becomes conspicuous increased systematically from 9.8 K in the bulk to 19.7 K in the nanoparticles with $d = 7$ nm, reflecting the core−shell effect on the ME properties.

In addition, we report the observation of $H$ induced $P$ in a $Cu^{2+}$ ($S$=1/2) based staircase kagome compound $PbCu_3TeO_7$, in which anisotropic magnetic exchange interaction and spin frustration result in two Neel temperatures at $T_{N1}$=35 K and $T_{N2}$=24 K. Below $T_{N2}$, both pyroelectric and ME current measurements reveal that a finite $P//a$ up to 15 μC/m$^2$ develops under $H$//c of ~ 8.3 T at which the field induced spin flop transition occurs as verified by the magnetization curve. Furthermore, measurements under $H$//$a$ uncover that the $P$ =14 μC/m$^2$ appears at ~16 T and disappears at ~38 T. Monte-Carlo simulations reveals that the two antiferromagnetic spin ordering exhibit a sinusoidal modulation below $T_{N1}$ and an incommensurate proper screw type spin rotation below $T_{N2.}$ The simulation results uncover an *ab* plane type spiral order under $H$//a and $H$//c, while the successive transition to form spiral spin order rotating in bc-plane for $H$//a. In combination with the experimental and theoretical results, we propose field-induced phase diagram along the two applied $H$ directions.

Finally, we study the ME properties in cubic $Cu_3TeO_6$ which is first discovered linear ME compound with $Cu^{2+}$ ($S$=1/2). The $P$ increases linearly under $H$ below $T_N$=62 K and the sign of $P$ does remains same upon changing the $H$ direction. The spin structure without spatial inversion symmetry support the linear ME effect.

These results are meaningful since they opened new possibility of successive researches on the ME effect by providing new technique of ME measurement and discovering new ME materials.

**Keyword :** magnetoelectric, ferroelectric, nanoparticles, magnetic frustration, $S$=1/2 spin, linear magnetoelectric

**Student Number :** 2010 - 23148

# Table of Contents

# List of figures

# List of tables

# Chapter 1

# Introduction

## 1.1 Multiferroics and magnetoelectric effect

In the modern era, electricity and magnetism have been inevitable in our daily life. The electronic devices we always use such as computer and fluorescent light have been developed on the fundamental understanding of electromagnetism. In that sense, the electromagnetism developed until 19$^{th}$century changed many aspects of mankind.

According to the Maxwell equations [1], which were formulated by James Clerk Maxwell in 1860s, the electric current generates the magnetic field and the change of magnetic flux gives rise to the electric voltage. They indicate that the dynamics of electricity (magnetism) affects the magnetic (electric) property. Meanwhile, the static relation, called magnetoelectric (ME) coupling, was first postulated by Pierre Curie [2] in 1890s. The ME coupling is defined by the changes the magnetization $M$ (electric polarization $P$) under electric field $E$ (magnetic field $H$). The prediction of this new phenomenon showed a possibility on further understand and development of electromagnetism. After several decades, the ME coupling was first theoretically proposed in 1959 [3] and experimentally realized in 1960 [4] in a solid state material, $Cr_2O_3$.

Meanwhile, the term ‘Multiferroics’ was first used by H. Schmid [5], and this indicates the materials which shows more than one ‘ferroic’ properties such as ferro-electricity, ferromagnetism, ferroelasticity. In the 21 century, the

multiferroics usually means the materials which have both magnetic ordering and electric polarization simultaneously. Even though the meaning of multiferroics and magnetoelectric materials has different meaning, they are closely related since the two phenomena usually occur in a same material and have same microscopic origin.

However this ME coupling and multiferroicity have been nontrivial issue, because the symmetry for generation of *P* and *M* is different; i.e., *P* requires break of inversion symmetry while *M* requires invariance upon the time reversal. Therefore, they usually have been realized only by the mediation of electrons on the crystalline lattice in which the properties of spin, lattice, and orbital are closely related for reducing the symmetries of the systems. Indeed, in the earlier ages of researches on ME effect ($20^{th}$ century), there were only few ME materials were found and their ME coupling were also small.

In 2003, ME coupling in a frustrated spin system, terbium manganite perovskite ($TbMnO_3$) was reported by T. Kimura [6]. In $TbMnO_3$, huge ME coupling was realized from the concept of spin-driven ferroelectricity. This discovery triggered revival and surge on the researches, not only on the physical origins [7-8] but also on the application for the devices [9]. From then, a number of ME materials such as $RMnO_3$ ($R$ = Tb, Dy…) [10], $CoCr_2O_4$, [11], $Ni_3V_2O_8$ [12], $MnWO_4$ [13], $Ca_3CoMnO_6$ [14], $CuFeO_2$ [15], $Ba_2CoGe_2O_7$ [16] have been discovered and the

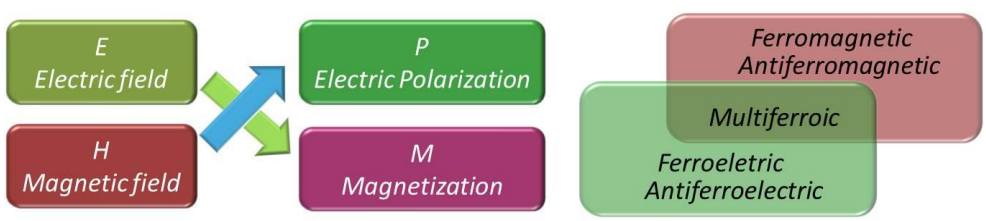


**Figure 1.1** Magnetoelectric coupling (left) and multiferroics (right)

underlying physics have been investigated with various experiment tools like, neutron [17], terahertz spectroscopy [18], and Lorentz TEM [19].

In this chapter, I will first briefly explain the underlying physical theory and microscopic origins on the ME effect and I will focus on the ME materials with spin 1/2 ($Cu^{2+}$) systems.

### 1.1.1 Linear magnetoelectric coupling

Generally, the free energy of a system can be expressed by the Landau expansion of electric field (*E*) and magnetic field (*H*).

$$F(E,H) = -PE - \mu_0 MH + \frac{1}{2}\varepsilon_0 \varepsilon E^2 + \frac{1}{2}\mu_0 \mu H^2 + \alpha EH + \frac{1}{2}\beta EH^2 + \gamma E^2 H + \frac{1}{2}\pi E^2 H^2 + \cdots \quad (1.1)$$

where $\varepsilon$ and $\mu$ ($\varepsilon_0$ and $\mu_0$) are the dielectric permittivity and magnetic permeability of the material (vacuum) and $\alpha$, $\beta$, $\gamma$, and $\pi$ are linear ($\alpha$), quadratic ($\beta$) and higher order ME coefficients. By minimizing $F$ with respect to $E$, the modulation of *P* at *E* = 0 under low magnetic field regions can be described as

$$\Delta P(E,H) = P(E,H) - P(E,0) = \alpha H + \frac{1}{2}\beta H^2 + (\gamma H + \pi H^2)E + \cdots \quad (1.2)$$

With the same way, the magnetization *M* induced by *E* with the condition of *H* = 0 can be written as

$$\Delta M(E,H) = M(E,H) - M(0,H) = \alpha E + \gamma E^2 + (\beta H + \pi EH)E + \cdots \quad (1.3)$$

The linear ME coefficient $\alpha$ represents the linear ME effect in which the *P* (or *H*) increase linearly upon increasing the *H* (or *E*). Since the *P*, *M*, *E*, and *H* are vector form, $\alpha$ has second order tensor form and is called linear ME tensor. It is noteworthy that the *H* and *E* break time reversal and spatial inversion symmetry, respectively, while the *P* and *M* appears in the systems without spatial inversion and time reversal symmetry, respectively. Therefore, the ME tensor $\alpha$ becomes nonzero only when both of the space-inversion symmetry and time reversal symmetry are broken. Meanwhile, the free energy should be invariant in symmetry. Thus, according to the term '$\alpha EH$', the symmetry of space inversion and time reversal together should not be broken.

One of the important examples in which the linear ME effect is realized is magnetic multipole [20]. In the magnetic monopole, quadrupole, and the toroidal moment, each of space-inversion and time reversal symmetry of spin structure is

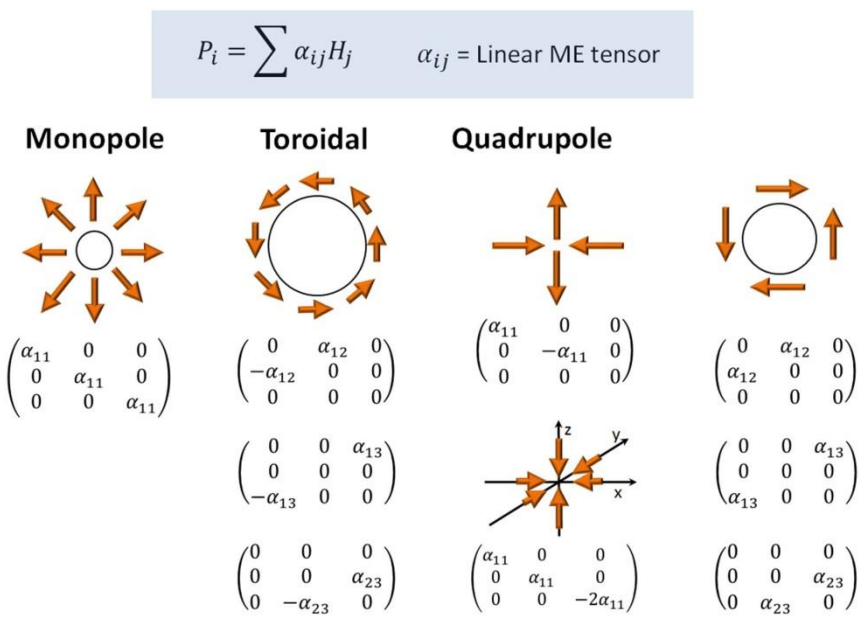


**Figure 1.2** Magnetic multipoles which generate the linear ME effect, and the resultant linear ME tensors.

broken. However, if we take both of them, space-inversion and time reversal, the spin symmetry remains same, thus these can give rise to the linear ME effect. Meanwhile, the magnetic dipole moment does not break the inversion symmetry. The available 9 linear ME tensors in the magnetic multipoles are shown in Figure 1.2. The monopole gives rise to the only isotropic and diagonal ME effect, whereas the toroidal moment generate the asymmetric and off-diagonal ME effect. The toroidal moment $t$ is defined as $t = \sum_i r_i \times S_i$ where the $r_i$ is displacements of spins $S_i$ [21]. The linear ME tensor from magnetic quadrupole can have five forms according to the shape of quadrupole. Recently, a kind of the magnetic quadrupole was realized in the $Ba(TiO)Cu_4(PO_4)_4$ with Cu-based $Cu_4O_{12}$ square cupolas and its magneto-dielectric properties were investigated [22].

Another way to predict the ME tensor is to consider the magnetic point group [23]. According to the symmetries of magnetic structures on the crystal lattice positions, there are 122 possible point groups [24]. Among them, only 58 magnetic point groups in which the space inversion symmetry is broken can have non zero linear ME tensor [25]. The linear ME tensors can be obtained from the applying the symmetry operation of the magnetic point groups [23].

The linear ME coupling have been experimentally observed on several compounds including $Cr_2O_3$ [4, 26] and $GaFeO_3$ [27]. The multipole and ME tensor analyses are applicable to the representative linear ME materials (Fig 1.3). The $Cr_2O_3$ has corundum lattice structure and $Cr^{3+}$ ions have antiferromagnetic order along the c-direction. However each two spins along c-direction are close to each other, thus the inversion symmetry is broken. The dimerized spin configuration can be expressed by combination of magnetic monopole and quadrupole, which

verifies the diagonal linear ME tensor [20]. In addition, the magnetic point group of $\bar{3}'m'$ also derives the diagonal linear ME tensor [23]. Meanwhile, $GaFeO_3$ has magnetic point group of $\mathrm{m'm2'}$ which allows the ME tensor with off diagonal components. The magnetic ion $Fe^{3+}$s form four layers along the b-direction, and each two layers are closer each other. The spins indicate c-direction in the first layer and the opposite direction in the second layer and vice versa. In this system, the toroidal momentum of $t = \sum_i r_i \times S_i$ becomes nonzero, thus also allowing the off-diagonal ME effect [27]. It is noteworthy that the spins does not need be in 'doughnut' shape to form a toroidal moment $t$.

By the way, the magnitude of linear ME materials ($\alpha$) has upper bound which is provided by the ordinary electric ($\chi^e$) and magnetic ($\chi^m$) susceptibilities.

$$\chi^e \chi^m > \alpha^2 \qquad (1.4)$$

This is obtained by calculating the change in the free energy that occurs when

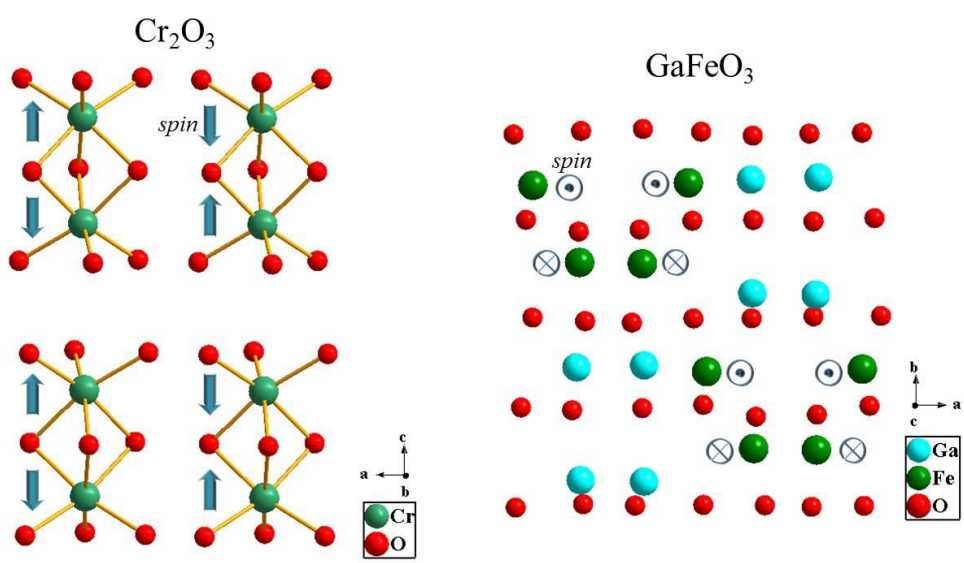


**Figure 1.3** Lattice and spin structure of $Cr_2O_3$ (left) and $GaFeO_3$ (right).

electric and magnetic fields are simultaneously applied to a magnetoelectric medium [20].

### 1.1.2 Phase controlled multiferroicity and magnetoelectric coupling

In general, coexistence of magnetic and electric ordering in a material is quite rare. This is because the magnetism comes from the partially filled d-shell electrons, while the electric polarization from noncentrosymmetric lattice requires the empty d-shell. Therefore the magnetism and ferroelectricity are mutually exclusive. In several magnetoelectric multiferroic compounds such as $BiFeO_3$ [28] and $BiMnO_3$ [29], the magnetism (from the transition metal) and the ferroelectricity come from other atoms. Since the origin of magnetic and electric properties are different, they does not occur at the same time and the ME coupling is relatively small even though they exhibit huge electric and magnetic order parameters.

Another strategy to realize huge ME coupling is the employment of phase control. If there are materials with special magnetic order which induce the electric polarization, so-called spin-driven ferroelectric materials, they can exhibit strong ME coupling. In that case, the magnetic and electric transitions occur concurrently. In addition, since they show nonlinear ME coupling at the phase transition, the magnitude of ME coupling does not bound by other properties as shown in Eq. (1.4).

An important example of the phase controlled ME effect is observed in a distorted perovskite compound $TbMnO_3$. The $TbMnO_3$ shows concurrent transition into ferroelectric and incommensurate magnetic phase. In addition, as the magnetic field is applied along b-direction, the polarization c-direction suddenly rotate to the

b-direction. The successive neutron diffraction studies revealed that the plane of spiral magnetic order, which give rise to *P*, rotates at the same magnetic field of the *P* rotation [30]. Since the discovery of the giant ME effect by controlling phase in $TbMnO_3$, many ME materials of spin origin have been discovered and underlying origins have been investigated [11-16].

It is noteworthy that most of the recently reported spin-driven ferroelectricity have been realized in spin-frustrated system, in which the nearest neighbor interaction (NNI) and the next nearest neighbor interaction (NNNI) compete each other [31]. The spin-frustrations usually come from special lattice structures such as triangle [10], pyrochlore [11], and Kagome lattices [12].

## 1.2 Microscopic origins of the spin-mediated magneto-electric effect

As we considered the in previous section, special spin, orbital and lattice orders, in which the space-inversion symmetry is broken, should be realized to achieve the large ME coupling. Most of the spin-mediated magnetoelectric couplings are realized in oxide-materials with transition metal. In this section, we deal with three major origins according to the orderings of the oxygen and transition metal; exchange striction model, Inverse DM model, and spin-dependent *p-d* hybridization model. The first model comes from the interacting spins coupled with a polarizable chemical lattice. The Second model originates from interacting non-collinear spins under the influence of relativistic spin-orbit coupling. The last

model originates from the spin-direction dependent hybridization of *p*- and *d*-orbitals via spin-orbit coupling.

### 1.2.1 Exchange Striction model

It is known that the dimerized ions with different valence give rise to electric polarization. The dimerization can be realized by special spin order through the Heisenberg exchange interaction between the two neighbor spins. This exchange striction model describes electric polarization in the dimerized ion due to the spin – induced striction along a crystallographic direction. The induces local polarization $P_{ij}$ in two spin sites of $S_i$ and $S_j$ is expressed by

$$P_{ij} = \pi_{ij}(S_i \cdot S_j). \qquad (1.5)$$

The $\pi_{ij}$ mainly depends on the positions of the underlying ions. Therefore, this model does not require the spin-orbit interaction (SOC), however, requires specific chemical lattices and spin ordering. For example, let us assume the spin sites on the

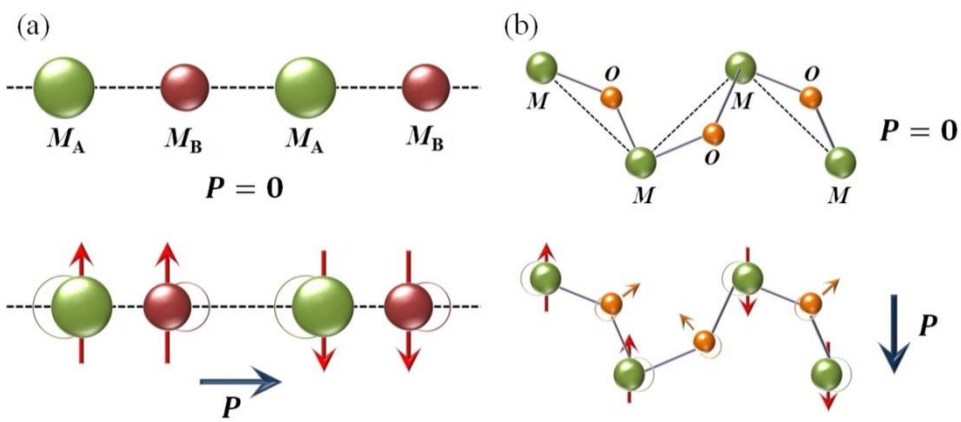


**Figure 1.4** Exchange-striction mechanism from (a) the collinear magnetic ions with alternative valence ($M_A$, $M_B$) and (b) the zig-zag displacement of *M* and oxygen (*O*) ions.

alternating A-B type ions with different valence show sequence of up-up-down-down. The special spin order is usually stabilized in the Ising spin chain in which the ferromagnetic NNI ($J_{NNI}$) and antiferromagnetic NNNI ($J_{NNNI}$), is competing with $|J_{NNNI}/J_{NNI}| > 1/2$. Then the lattice will be dimerized because the spins of same direction attract each other and that of opposite direction repel, thus giving rise to the electric polarization (Fig 1.4(a)).

One of the simplest ways to design ferroelectricity from this mechanism is to put ↑↑↓↓ spins on the 'AB' lattice. This situation indeed realized in the $Ca_3Co_{2-x}Mn_xO_6$ (x = 0.96) in which the $Mn^{4+}$ ion is replaced in the $Co^{2+}$ ion position from $Ca_3Co_2O_6$ [14]. In $Ca_3Co_{2-x}Mn_xO_6$, $Mn^{4+}$ and $Co^{2+}$ ions with different valence are stacked alternatively along c-direction, and have spin order of ↑↑↓↓ below the magnetic transition temperature, thus showing ferroelectricity.

Another example is from the *M-O-M* bond (*M* is transition metal and *O* is oxygen ) which is not in straight line but in zigzag line and spins order in up-up-down-down sequence (Fig 1.3 (b)). Because of the displacement of the magnetic ions, the angle between *M-O-M* ions changes, resulting in the displacement of *O* ion as well. Therefore, the *O* displacement gives rise to the electric polarization. The scenario was realized in the perovskite rare earth manganites, $RMnO_3$ (*R* = Ho, Er, Tm, Yb, and Lu) [32-34].

### 1.2.2 Spin current model (Inverse DM model)

The magnetic frustration usually makes the spin ordering non-collinear. For example, if the spins lie on the one-dimensional lattice structure and the ferro (antiferro) magnetic NNI and antiferro (ferro) magnetic NNNI compete each other

with ratio of $|J_{NNNI}/J_{NNI}| > ¼$ , then the spiral magnetic order is more stable than the ferro(or antiferro) magnetic order. H. Katsura *et al.* [34] explained that the spiral magnetic order give rise to electric polarization with a mechanism called 'spin current model'. The spin current has attracted interest as one of essential concepts of spintronics in semiconductor [36]. In an insulator, the spin current is rather identical to the vector spin chirality [31] and it gives rise to electric polarization since its space-inversion and time-reversal symmetry are broken simultaneously. By using a simple three-atom model the electric polarization can be expressed by

$$P_{ij} = Ae_{ij} \times (S_i \times S_j) \propto e_{ij} \times \vec{j}_s \ . \qquad (1.6)$$

The *A* is determined by the spin-orbit interaction, spin-exchange interaction, and the possible spin-lattice coupling term, while the $\vec{j}_s$ is spin current which is proportional to the $S_i \times S_j$. As we can see from the Eq (1.6), the sign of *P* depends on whether the spins rotate clock-wise or counter clock-wise (called helicity) in proceeding along the propagation axis.

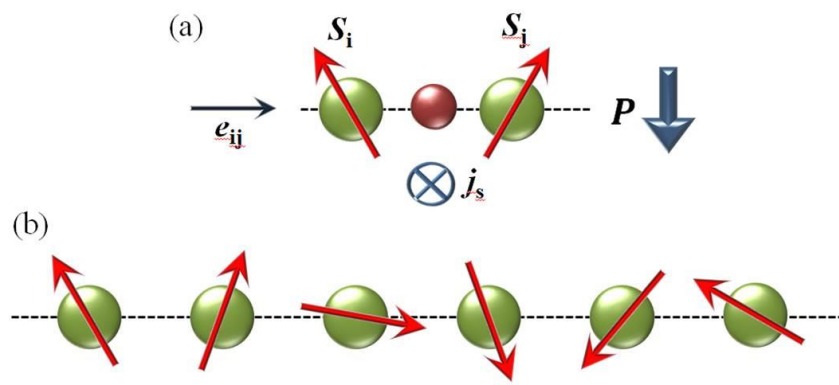


**Figure 1.5** (a) Spin current model with the spin current ($j_s$) flowing between the two magnetic ions and (b) the spiral magnetic ordering giving to electric polarization *P*.

However, the spin current model does not consider the displacement of ions which also can be an origin of electric polarization. I. A. Sergienko *et al.* [37] investigated the ion displacements and showed that the same formula of Eq (1.6) can be derived from the inverse Dzyaloshinskii-Moriya (DM) interaction. We assume a situation that two magnetic ions (*M*) and one ligand ion (e.g. oxygen, *O*) are in order of *M*-*O*-*M*. The DM interaction shows that the displacement of ligand ion induces the canting of the neighboring spins via spin-orbit coupling. This DM interaction occurs by maximizing the energy gain of

$$H_{DM} = D^{DM} \cdot (S_i \times S_j), \qquad (1.7)$$

where $D^{DM}$ is a vector dependent on the local symmetry. On the contrary, the inverse DM interaction describes that the canted two spins induce the displacement of the ligand ion, thus giving rise to the electric dipole.

The two models of spin current (from electron distribution) and inverse DM

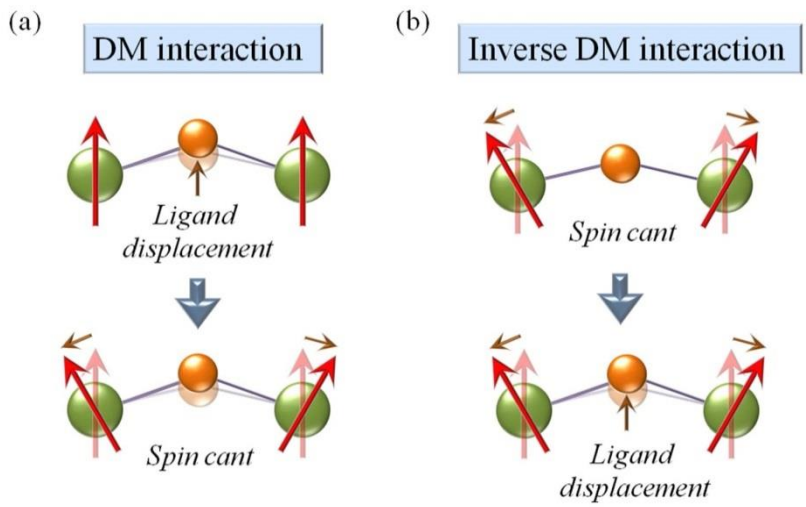


**Figure 1.6** (a) Dzaloshinskii-Moriya (DM) interaction in which the ligand displacement induce the spin cant and (b) Inverse DM interaction in which the spin canting induces the ligand displacement.

interaction (from ion displacement) mentioned above suggest different origins of polarization, however, both of them contribute to the electric dipole in real matter with the Eq (1.7). If the outer products of neighboring spins along the propagation direction have same direction, they produce electric dipoles with same direction which is macroscopically electric polarization *P*.

There are several non-linear spin ordering realized in condensed matters as shown in Fig (1.7), however, not all of the ordering exhibit ferroelectricity. Even though the all spin orders in Fig (1.7) have nonzero spin current of $\vec{J}_s \propto S_i \times S_j$, the screw and longitudinal conical order have the spin current parallel to the propagation vector, $\vec{J}_s \,//\, e_{ij}$, thus does not satisfy condition to generate electric polarization with this model. Some compound with proper screw order (e.g. $CuFeO_2$[15]) shows electric polarization, however, the origin is spin-dependent p-d hybridization, not the spin current. Therefore, only the cycloidal and transverse conical ordering generate the ferroelectricity through the spin current model by satisfying the condition of the spin current perpendicular to the propagation vector, $\vec{J}_s \perp e_{ij}$.

A number of the cycloidal and transverse conical spins have been shown in frustrated magnetic systems. The cycloids were realized in the frustrate channel of Kagome ($Ni_3V_2O_8$ [12]), triangle ($RMnO_3$[10]), (quasi) one-dimensional chains ($MnWO_4$[13], $LiCu_2O_2$[38]) and so on.

Meanwhile, the transvers conical state is induced by magnetic field in the $CoCr_2O_4$[39] and hexaferrites.[40-41]. Unlike the cycloid, this order gives rise to spontaneous magnetization as well as electric polarization, thus realizing the

ferromagnetic ferroelectric state. In addition, very small magnetic field can control large electric polarization of in the transverse conical state in the hexaferrites.

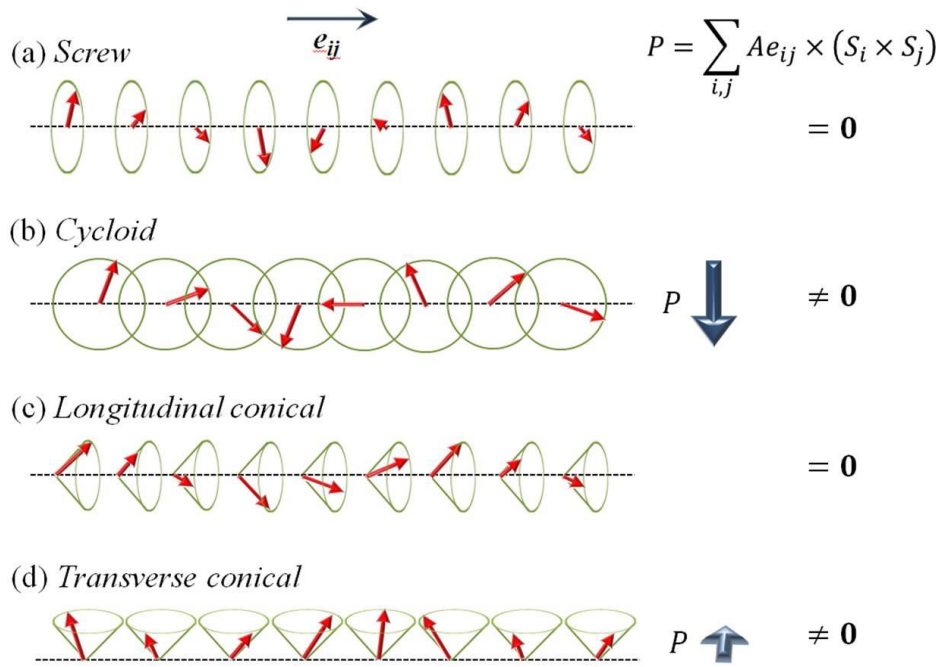


**Figure 1.7** Schematic illustrations of the non-collinear spiral spin orders including (a) proper screw, (b) cycloid, (c) longitudinal conical, and (d) transverse conical magnetic structure.

### 1.2.3 Spin-dependent *p-d* hybridization model

In this model, unlike the exchange striction and spin-current model, we consider only a pair of a transition metal magnetic ion and a ligand ion which produce the local electric dipole. In most magnetic oxide materials, the transition metal ion and oxygen ion have bonding through the hybridization of the electrons from the outer shell of *d*-orbital and *p*-orbital respectively. We call this '*p-d* hybridization'. By the way, the perturbation by the spin-orbit interaction, which is spin-direction dependent, changes the energy difference between the *p* and *d* orbitals. Therefore, the change of the *p-d* hybridization gives rise to local electric dipole along the bonding direction (Fig 1.8(a)) [42]. This local dipole can survive as a macroscopic electric polarization only when they are not cancelled out over the crystal lattice. The polarization from this model is formulated as

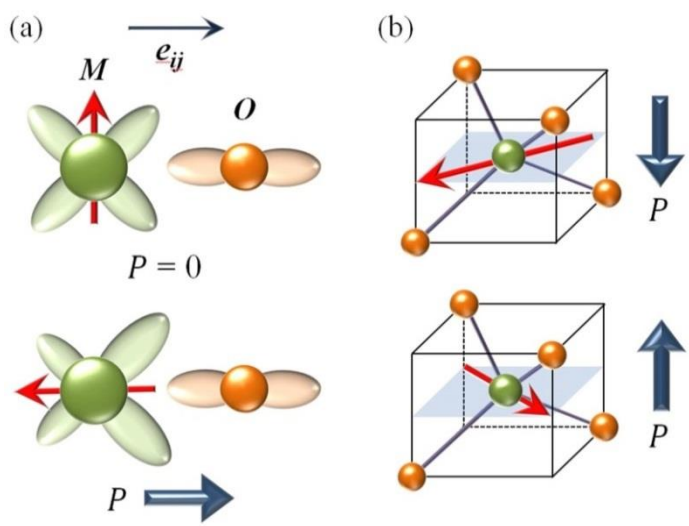


**Figure 1.8** Schematic illustrations of (a) spin direction dependent modulation of hybridization between the d-orbital of magnetic ion (*M*) and p-orbital of oxygen ion (*O*) model and (b) the lattice of $MO_4$ tetrahedra in which the polarization does not cancel.

$$P_{pd} \propto e(S \cdot e)^2 \qquad (1.8)$$

where the $e$ is the vector connecting the magnetic ion and oxygen ion.

An effective tactic to avoid the cancellation of the electric dipole from *p-d* hybridization is to use crystal structure without space-inversion symmetry. One of the representative examples is the $Ba_2CoGe_2O_7$ with noncentrosymmetric point group of $P\bar{4}2_1m$ [16]. It has two inequivalent magnetic sites of Co which is surrounded by tetrahedron of oxygens. By the spin-orbit coupling, when the spin direction is along the lower-lying oxygens, the electric dipole is formed downward and vice versa (Fig. 1.8(b)). Since the tetrahedrons in the two magnetic sites are tilted slightly each other, the electric dipoles in each sites does cancel out, thus giving rise to macroscopic polarization.

## 1.3 Magnetoelectric effects in Spin ½ ($Cu^{2+}$) systems.

The most magnetoelectric compounds reported so far are transition metal oxide materials. Usually, they include magnetic atoms of Fe, Mn, Co, and Ni which are called ferrite, manganite, cobaldate, and nickelate, respectively. The magnetic atoms have spin of $S \geq 1$. However, the magnetoelectric (ME) effects in the spin $S$ = 1/2 systems have not attracted huge interest due to the lack of huge ME effect. This is partially because of the isotropic nature of $S$ = 1/2 spins and small spin-orbit coupling [43].

Meanwhile, $S$ = 1/2 spin systems are expected to provide new aspects of physics induced by quantum effects different from these of classical spins of Fe and Mn ions. According to the quantum mechanics, classical fluctuation is rather dominate

in the large spin systems with much larger than $S$ = 1/2 because the spins are considered to be oriented randomly due to the almost continuous energy levels. However, in the spin $S$ = 1/2 system, the uncertainty principle give rise to the quantum fluctuation which is proportional to only the size of spin down to 0 K. Therefore, the maximized quantum fluctuation spin $S$ = 1/2 combined by the geometrical frustration prevent the magnetic long range ordering, thus giving rise to the 'quantum spin liquid' phase [44]. In addition, the quantum fluctuation is also expected to affect the ME effects. For example, some recent theoretical report suggested that the quantum fluctuation appreciably reduce the amplitude of chiral ordering, thus reduce the effective magnitude of electric polarization from the spin-orbit coupling [45].

The table 1.1 lists the representative magnetoelectric compounds with the $Cu^{2+}$ (spin ½) ions. Interestingly, many of the Cu based ME compound (the first five compounds in the table 1.1) commonly include quasi-one-dimensional frustrated spins with the $CuX_2$ ($X$ = O, Cl, Br) chains along the b-direction (Fig 1.9). The figure 1.10 illustrates how the spins on the $CuO_2$ chains are frustrated. The nearest-neighbor exchange is expected to be ferromagnetic because the binding angle of Cu-O-Cu is almost 90°, according to the Anderson-Kanamori-Goodenough rules [53]. The next-nearest-neighbor exchange is antiferromagnetic according to the rule for super-super-exchange interaction since the interaction is done through two oxygens. The frustration from the two interactions is ideal model system to realize the spin current mechanism with cycloidal magnetic ordering.

By the way, some of the quasi-one-dimensional systems are reported to show magnetoelectric effect inconsistent with the prediction of the spin current model.

For example, $LiCu_2O_2$ shows *P*//c with the cycloidal magnetic ground state [38]. Several successive reports on diffraction studies proposed more complex spin orders than the simple cycloid [55-56], and the spin structure as an origin of ferroelectric nature is still under controversy.

**Table 1.1 List of magnetoelectric compounds with the spin ½ ($Cu^{2+}$) system**

| | Structure | Spin order | $T_{FE}$ (K) | $P$ ($\mu C/m^2$) | Origin* | Ref. |
|---|---|---|---|---|---|---|
| $LiCu_2O_2$ | Orthorhombic | Cycloid | 23 | 8 | SC | [38] |
| $LiCuVO_4$ | Orthorhombic | Cycloid | 2 | 30 | SC | [46] |
| $PbCuSO_4(OH)_2$ | Monoclinic | Cycloid | 2.8 | 4 | ? | [47] |
| $CuCl_2$ | Monoclinic | Cycloid | 24 | 25 | SC | [48] |
| $CuBr_2$ | Monoclinic | Cycloid | 73.5 | 22.5 | SC | [49] |
| CuO | Monoclinic | Cycloid | 230 | 150 | ? | [50] |
| $Cu_2OSeO_3$ | Cubic | Helical | 59 | 16 | p-d | [51] |
| $CuB_2O_4$ | Tetragonal | Canted AFM | 21 | 1.3 | p-d | [52] |
| $SrCuTe_2O_6$ | Cubic | ? | 5.5 | 0.018 | ? | [43] |
| $PbCu_3TeO_7$ | Orthorhombic | Cycloid? | 24 | 15 | ? | |
| $Cu_3TeO_6$ | Cubic | Toroidal? | 62 | 20 | ? | |

* SC = Spin current
p-d = p-d hybridization

The structure includes the Cu-O chains along the [101] and $[10\bar{1}]$ directions, which give rise to ferromagnetic and antiferromagnetic interaction, respectively. The competition between the two interactions gives rise to the helical ordering at such a high temperature, 230K, due to the strong antiferromagnetic interaction along $[10\bar{1}]$ direction.

$CuB_2O_4$ and $Cu_2OSeO_3$ show magnetoelectric properties from p-d hybridization due to their non-centrosymmetric lattice structure [51] and proper screw magnetic structure [52], respectively. Note that the application of magnetic field in $Cu_2OSeO_3$ leads to a special spin texture of 'Skyrmion' and this is first reported multiferroic compound which shows Skyrmion [57].

Recently, three magnetoelectric materials with $Cu^{2+}$ ions have been discovered in our laboratory. The $SrCuTe_2O_6$ have cubic structure, and the strongest exchange interactions of spins form the quasi-1 dimension. In this materials, the magnetoelectric coupling is too small, thus it is observable only in the measurement with poling electric field [43]. Meanwhile, $PbCu_3TeO_7$ and $Cu_3TeO_6$ show unique phase controlled and linear magnetoelectric effects, respectively. In this thesis, we will deal with the detailed experimental results and analyses to understand the origin of magnetoelectric effect.

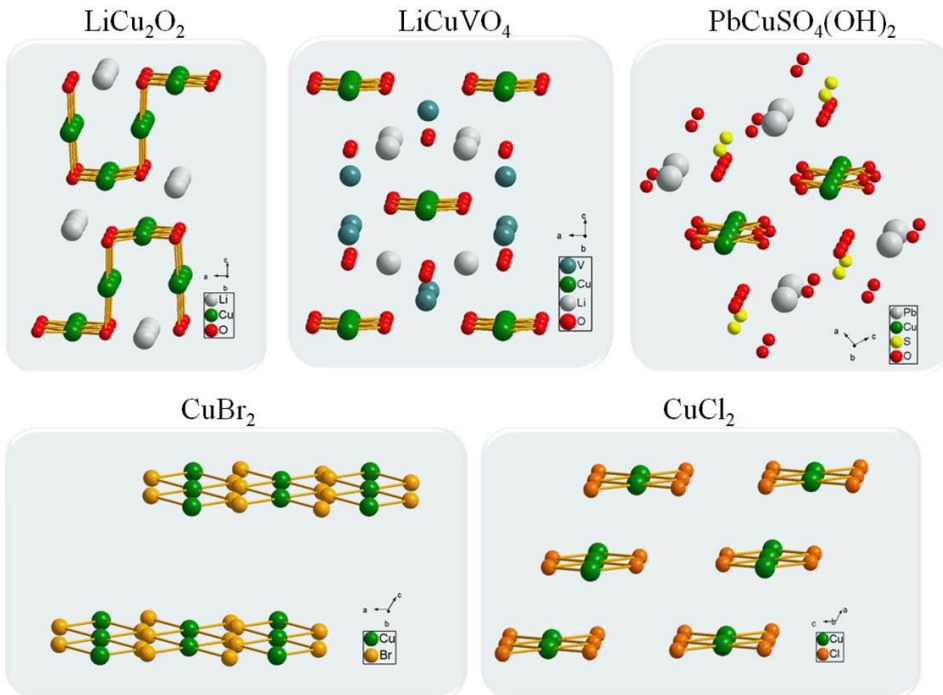


**Figure 1.9** Lattice and spin structure of several ME compounds with quasi-one-dimensional $Cu^{2+}$ chains.

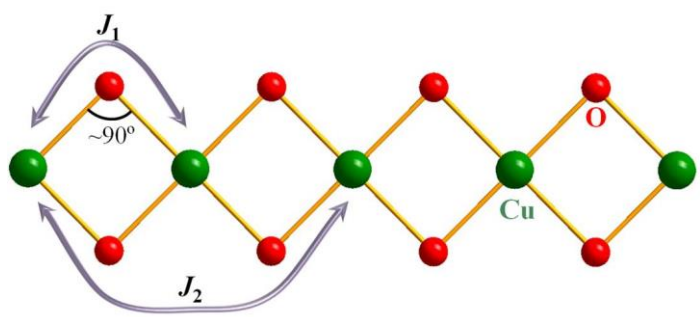


**Figure 1.10** Exchange interactions between the magnetic $Cu^{2+}$ ions in the edge-shared $CuO_2$ chain

## 1.4 Magnetoelectric and magneto-dielectric effects in nanostructures

Recently, the nanotechnologies have being developed tremendously, which enables us to manipulate matters on an atomic, molecular, and supramolecular scale. This triggered the development of devices such as memory and bio-medical devices to be miniaturized and highly integrated. Following the trends of the miniaturization of devices, magnetoelectric/magneto-dielectric and multiferroic properties in nanostructures have been intensively investigated since H. Zheng *et al* [58] reported the multiferroic properties in the nanostructures of $BaTiO_3/CoFe_2O_4$ composites.

The Figure 1.11 show the list of nanostructures which have ME effect. From the view of material components, ME nanomaterials can be divided into two types: single-phase materials and composites. Many attempted to investigate ME coupling in nanocomposite ME materials which are usually composed of magnetostrictive and piezoelectric materials. For examples, the strain coupling between $CoFe_2O_4$ nanopillars and $BiFeO_3$ matrix can generate the electric polarization under magnetic field [59]. The main advantage of the composite materials is large ME coupling at room temperature. According to the connection shape of the two materials, the ME composites can be divided into 3-1, 2-2, 3-0, and 0-0 types. The 3-1 type represents the piezoelectric nanopillars embedded in the magnetic thin file, and the 2-2 type is shown in the multilayer laminates. The 3-0 type is made by mixing the piezoelectric and magneto-strictive particles with nano-size, and 0-0 type represents the core-shell nanoparticles.

On the other hand, the single-phase ME nanostructures can be divided into

## Composite

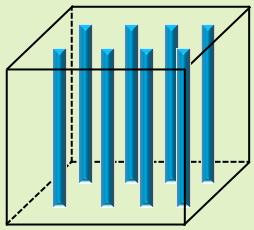

***3-1 type***

$BaTiO_3/CoFe_2O_4$, MF* [58]

$BiFeO_3/CoFe_2O_4$, ME [59]

$PbZr_{0.52}Ti_{0.48}O_3/CoFe_2O_4$, ME [60]

….

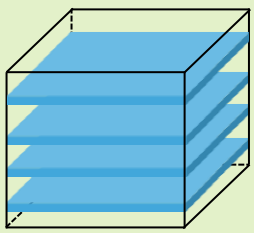

***2-2 type***

$PbZr_{0.52}Ti_{0.48}O_3/CoFe_2O_4$, ME [61]

$PbZr_{0.6}Ti_{0.4}O_3/Ni_{0.8}Zn_{0.2}Fe_2O_4$, ME [62]

$PbZr_{0.52}Ti_{0.48}O_3/ La_{0.7}Sr_{0.3}MnO_3$, ME [63]

….

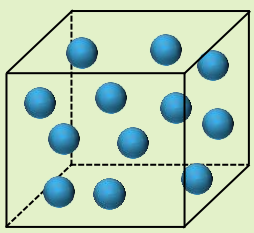

***3-0 type***

$PbZr_{0.52}Ti_{0.48}O_3/NiFe_2O_4$, ME [64]

$PbZr_{0.52}Ti_{0.48}O_3/CoFe_2O_4$, ME [65]

$Bi_{3.15}Nd_{0.85}Ti_3O_{12}/CoFe_2O_4$, ME [66]

…

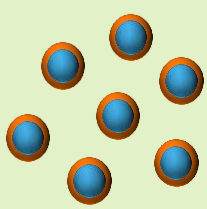

***0-0 type (core-shell)***

$PbZr_{0.52}Ti_{0.48}O_3/NiFe_2O_4$, ME [67]

$BaTiO_3/CoFe_2O_4$, ME [68]

$BaTiO_3/La_{0.7}Sr_{0.3}MnO_3$, ME [69]

…..

## Single materials

***Nanoparticles***

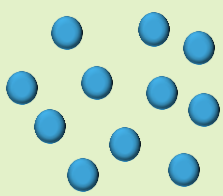

$Fe_3O_4$, ME [70]

$BiFeO_3$, ME [71]

ε-$Fe_2O_3$, MD [72]

γ-$Fe_2O_3$, MD [73]

***Thin film***

$BiFeO_3$, ME [74]

$TbMnO_3$, ME [75]

$DyMnO_3$, ME [76]

$YMnO_3$, MF [77]

* ME = Magnetoelectric, MD = Magneto-dielectric, MF = Multiferroic

**Figure 1.11** Selected list of magnetoelectric/multiferroic nanostructures

nanoparticles and thin films. Usually, the materials with ME properties in bulk phase are made nano-size. However, because of scarcity of the single-phase ME materials as well as technical challenge to measure ME properties in single nanostructure due to their ME signal and high electric leakage, there have been just few report on the nanoparticles and films. Some of reports [72-74] show magneto-dielectric (MD) effects which does not guarantee the intrinsic ME effects. On the other hand, quantitative intrinsic ME coupling under various magnetic fields and temperatures have been investigated in $Fe_3O_4$ nanoparticles [70, Chapter 5] and $BiFeO_3$ thin film [74].

## 1.5 Purpose

As we discussed in the previous sections, the magnetoelectric effects in the spin $S$ = 1/2 systems and nanostructures have special interests. However, still there is lack of extensive and quantitative investigations on the materials of the two groups. In this thesis, we focus on the nanoparticles of $Fe_3O_4$ and two new discovered magnetoelectric materials with $Cu^{2+}$ ($S$ = 1/2) ions, $PbCu_3TeO_7$ and $Cu_3TeO_6$. In Chap. 3, we report quantitative measurement of the magnetoelectric effect in the $Fe_3O_4$ nanoparticles with various particle diameters. In Chap. 4, we study the magnetic field induced ferroelectric properties on poly and single crystals on the $PbCu_3TeO_7$ including analysis on the possible magnetic structures to explain the ferroelectric properties. Finally in Chap. 5, we study the linear magnetoelectric properties in $Cu_3TeO_6$ with establishing possible scenarios to explain the linear magnetoelectric effect. Finally in the appendix, we added the experimental manual of a pulsed magnet system development in the laboratory.

## 1.6 References


[1] J. C. Maxwell, Phil. Trans. R. Soc. Lond. **155,** 459 (1865).

[2] P. Curie, J. Phys. 3(Ser.III), 393 (1894).

[3] I. E. Dzyaloshinskii, Sov. Phys. JETP **10,** 628 (1959).

[4] D. N. Astrov, Sov. Phys. JETP **11,**708 (1960).

[5] H. Schmid, Ferroelectrics **162,** 317 (1994).

[6] T. Kimura *et al.,* Nature **426,** 55 (2003).

[7] S. –W. Cheong *et al.,* Nature **6,** 13 (2007).

[8] Y. Tokura *et al.,* Rep. Prog. Phys. **77,** 076501 (2014).

[9] J. Ma *et al.,* Adv. Mater. **23,** 1062 (2011).

[10] T. Goto *et al.,* Phys. Rev Lett. **92,** 257201 (2004).

[11] Y. Yamasaki *et al.,* Phys. Rev. Lett. **96,** 207204 (2006).

[12] G. Lawes *et al.,* Phys. Rev. Lett. **95,** 087205 (2005).

[13] K. Taniguchi *et al.,* Phys. Rev. Lett. **97,** 097203 (2006).

[14] Y. J. Choi *et al.,* Phys. Rev. Lett. **100,** 047601 (2008).

[15] T. Kimura *et al.,* Phys. Rev. B **73,** 220401 (2006).

[16] H. Murakawa *et al.,* Phys. Rev. Lett. **105,** 137202 (2010).

[17] S. Lee *et al.,* Phys. Rev. B **71,** 180413 (2005).

[18] Y. Takahashi *et al.,* Phys. Rev. Lett. **101,** 187201 (2008).

[19] S. Seki *et al.,* Science **338,** 198 (2012).

[20] 有馬　孝尚‘マルチフェロイクス’、共立出版（２０１４）.

[21] N. A. Spaldin *et al.,* J. Phys.: Condens. Matter **20,** 434203 (2008).

[22] K. Kimura *et al.,* Nat. Comm. **7,** 13039 (2016).

[23] S. H. Chun, Ph. D. thesis (Seoul National University, 2013).

[24] D. B. Livin, Acta. Cryst. A **64,** 419 (2008).

[25] J. –P. Rivera, Eur. Phys. J. B **71,** 299 (2009).

[26] A. Iyama *et al.,* Phys. Rev. B **87,** 180408 (2013).

[27] T. Arima *et al.,* Phys. Rev. B **70,** 064426 (2004).

[28] G. Catalan *et al.,* Adv. Mater. **21,** 2463 (2009).

[29] J. Y. Son *et al.,* Appl, Phys. Lett. **84,** 4971 (2004).

[30] T. Arima *et al.,* Phys. Rev. Lett. **96,** 097202 (2006).

[31] T. Arima *et al.,* J. Phys. Soc. Jpn. **80,** 052001 (2011).

[32] D. Okuyama *et al.,* Phys. Rev. B **84,** 054440 (2011).

[33] A. Munoz *et al.,* J. Phys.: Condens. Matter **14,** 3285 (2002).

[34] V. Y. Pomjakushin *et al.,* New J. Phys. **11,** 043019 (2009).

[35] H. Katsura *et al.,* Phys. Rev. Lett. **95,** 057205 (2005).

[36] V. Zayets, Phys. Rev. B **86,** 174415 (2012).

[37] I. A. Sergienko *et al.,* Phys. Rev. B **73,** 094434 (2006).

[38] S. Park *et al.,* Phys. Rev. Lett. **98,** 057601 (2007).

[39] Y. Yamasaki *et al.,* Phys. Rev. Lett. **96,** 207204 (2006).

[40] S. H. Chun *et al.,* Phys. Rev. Lett. **108,** 177201 (2012).

[41] S. H. Chun *et al.,* Phys. Rev. Lett. **104,** 037204 (2010).

[42] T. Arima, J. Phys. Soc. Jpn. **76,** 073702 (2007).

[43] B. Koteswararao *et al.,* APL Materials **4,** 036101 (2016).

[44] L. Balent, Nature **464,** 199 (2010).

[45] S. Furukawa *et al.,* J. Phys. Soc. Jpn. **77,** 123712 (2008).

[46] Y. Yasui *et al.,* J. Phys. Soc. Jpn. **77,** 023712 (2008).

[47] Y. Yasui *et al.,* J. Phys. Soc. Jpn. **80,** 033707 (2011).

[48] S. Seki *et al.,* Phys. Rev. B **82,** 064424 (2010).

[49] L. Zhao *et al.,* Adv. Mater. **24,** 2469 (2012).

[50] T. Kimura *et al.,* Nature Mater. 7, 291 (2008).

[51] M. Belesi *et al.,* Phys. Rev. B **85,** 224413 (2012).

[52] N. D. Khanh *et al.,* Phys. Rev. B **87,** 184416 (2013).

[53] S. Blundell, Magnetism in Condensed Matter Oxford University Press (2001).

[54] T. Masuda *et al.,* Phys. Rev. Lett. **92,** 177201 (2004).

[55] A. Rusydi *et al.,* Appl. Phys. Lett. **92,** 252506 (2008).

[56] Y. Kobayashi *et al.,* J. Phys. Soc. Jpn. **78,** 084721 (2009).

[57] S. Seki *et al.,* Science **336,** 198 (2012).

[58] H. Zheng *et al.,* Science **303,** 661 (2004).

[59] Y. S. Oh *et al.,* Appl. Phys. Lett. **97,** 052902 (2010).

[60] J. X. Zhang *et al.,* J. Phys. D: Appl. Phys. **41,** 235405 (2008).

[61] Z. Li *et al.,* Phys. Rev. B **79,** 180406 (2009).

[62] S. Ryu *et al.,* Appl. Phys. Lett. **91,** 142910 (2007).

[63] Y. G. Ma *et al.,* Appl. Phys. Lett. **90,** 152911 (2007).

[64] H. Ryu *et al.,* Appl. Phys. Lett. **89,** 102907 (2006).

[65] J. G. Wan *et al.,* Appl. Phys. Lett. **86,** 122501 (2005).

[66] X. L. Zhong *et al.,* Appl. Phys. Lett. **90,** 152903 (2007).

[67] R. A. Islam *et al.,* J. Appl. Phys. **104,** 104111 (2008).

[68] K. Raidongia *et al.,* Appl. Phys. Lett. **97,** 062904 (2010).

[69] C. Nayek *et al.,* Mater. Res. Bull. **48,** 1308 (2013).

[70] K. Yoo *et al.,* Nano Letters **16,** 12 (2016).

[71] G. S. Lotey *et al.,* Mater. Lett. **111,** 55 (2013).

[72] M. Gich *et al.,* Nanotechnology **17,** 687 (2006).

[73] T. Bonaedy *et al.,* Appl. Phys. Lett. **91,** 132901 (2007).

[74] K. –T. Ko *et al.,* Nat. Comm. **2,** 567 (2011).

[75] N. Hu *et al.,* ACS Appl. Mater. Interface **7,** 26603 (2015).

[76] C. Lu *et al.,* Sci. Rep. **6,** 20175 (2016).

[77] M. Nakamura *et al.,* Appl. Phys. Lett. **98,** 082902 (2011).

# Chapter 2

# Experimental details

In this chapter, we will explain several measurement methods used for investigating the magnetoelectric properties in both static field (up to 14 T) and pulsed field (up to 60 T). The measurements listed below are essential and fundamental method to observe direct and indirect magnetoelectric properties and to estimate their physical origins.

## 2.1 Physical property measurements in static field

We used two kinds of cryostats of the static magnet, one is the physical property measurement system (PPMS$^{TM}$, Quantum Design) with 9 T magnet and the other is Janis cryostat with the 14 T magnet (Cryogenic Ltd). The PPMS$^{TM}$ is pot type cryostat in which the temperature control impedance and sample place is separated and the temperature control is easily done automatically by the software. However in the Janis cryostat, impedance is directly connected to the sample space and the temperature is controlled by hand with the needle valve which controls the impedance flow and with the power of pumping the sample space. Therefore, lower temperature (~1.3 K) can be reached in Janis cryostat than the PPMS$^{TM}$ (1.8 K), while more care is needed to control temperature and magnetic field. Meanwhile, for PPMS$^{TM}$, the automatic temperature and magnetic field control is possible, thus more effective to measure the physical properties.

### 2.1.1. Dielectric constant

The dielectric constant ($\varepsilon$) measurement is a basic tool to investigate electric properties of insulating materials. Actual dielectric constant has form of complex number of $\tilde{\varepsilon} = \varepsilon + i\varepsilon"$, in which the $\varepsilon$ (usually we call dielectric constant) is dielectric constant of perfect insulator and $\varepsilon"$ is dielectric loss showing the quantity of electric leakage current. We can observe clues of multiferroic and ME property by searching the anomaly or huge changes of $\varepsilon$ under various temperatures and magnetic fields. For the dielectric constant (and pyro/ME current, magnetoelectric susceptibility) measurement, the sample is shaped into a thin plate shape with thickness of 0.1 ~ 0.4 mm and electrodes are made on the both sides with the silver epoxy. We measured capacitance ($C$) of the samples with a capacitance bridge AH 2550 (Andeen-Hagering) with 1 kHz and an Agilent LCR meter with frequencies in 500 Hz – 1 MHz. The capacitance bridge performs with high resolution, but it cannot change the frequency like LCR meter, thus we can use one of them according to our purpose. They measure two quantities, the capacitance $C$ and $\varepsilon"/\varepsilon = \tan\ \delta$. The $\varepsilon$ can be calculated with the $C = \varepsilon\varepsilon_0 \frac{A}{d}$ ($\varepsilon_0$= electric permittivity in vacuum, A = electrode area, $d$ = thickness of the sample).

It is noteworthy that not all of the dielectric anomalies and magneto-dielectric effects come from intrinsic magnetoelectric effect. One major extrinsic effect is due to the combination of magnetoresistance and Maxwell Wagner effect [1]. We can diagnose this effect from two phenomena. One is the magneto-dielectric effect in which the sign of dielectric loss is opposite. Another one is a broad peak in the temperature dependent measurement whose peak position is frequency dependent.

### 2.1.2. Pyrocurrent/magnetoelectric (ME) current

The pyrocurrent and ME current measurements are easy and the most popular method to investigate temperature and magnetic field dependence of electric polarization which are essential information on the multiferroics and ME materials. The prefix 'pyro' came from a Greek word which means fire, thus it represent meaning of 'fire' or 'heat'. Therefore, the pyrocurrent is the current flow during the change of the temperature; i.e., during the heat transfer. In the ferroelectric (FE) materials, which usually show FE phase at low temperature, the depolarization current (pyrocurrent) flows as the FE material is warmed up from FE phase to paraelectric (PE) phase. Meanwhile, the ME current means the current flows under the change of magnetic field. The reason why it is called 'ME current' is that it is one of the direct measurements of ME property. The polarization can be calculated by integrating the current with the function of time.

$$\Delta P(t) = P(t) - P(0) = \frac{1}{sample\ area}\int_0^t I(t')dt' \qquad (2.1)$$

And the linear ME coefficient can be calculated from the ME current by

$$\alpha_{ME} = \frac{dP}{dH} = \frac{\frac{dP}{dt}}{\frac{dH}{dt}} = \frac{\frac{dQ}{dt\cdot A}}{\frac{dB}{\mu_0 dt}} = \frac{ME\ current/sample\ area}{field\ sweep\ rate} \cong \left[\frac{A/m^2}{A/m\cdot s}\right] = \frac{4\pi}{10^3}\left[\frac{A/m^2}{Oe/s}\right]. \qquad (2.2)$$

The current measurement is done by sensitive electrometer, KE 617 or KE 6517 with sensitivity of few femto-amperes ($10^{-15}$A). Since the charge of electron, 1.6 x $10^{-19}$ C, only few ten thousand electrons are flowing in this measurement. Therefore, we should remove all vibration near the cryostat and connect a clean ground.

In addition, especially for the pyrocurrent measurement, we should careful to monitor the sample temperature properly. Since the signal in the pyrocurrent is proportional to the sweep rate of temperature, we should sweep fast to measure small polarization. In the case of fast sweep, the temperature of sample and the thermometer is becomes inconsistent. For example, in the PPMS™ measurement, the position of sample and thermometer is not close each other resulting in variation of temperature of few kelvin when we sweep the temperature fast (~10 K/min). In order to solve this problem, it is better to set another thermometer close to the sample to monitor the sample temperature properly. If the pyroelectric current signal is big enough, it is better to sweep the temperature slowly to reduce the temperature inconsistency and obtain better data.

By the way, the pyrocurrent and ME current do not always represent the ferroelectric transitions since the extrinsic effects also come from electric leakage and trapped charge carriers. Let me explain several clues to distinguish the intrinsic and extrinsic pyrocurrent. First, examine the dielectric loss at the temperature range of pyrocurrent measurement. In the insulating enough samples, for example the $PbCu_3TeO_7$ and $Cu_3TeO_6$ single crystals, the value of dielectric loss is order of $10^{-3}$ or $10^{-4}$ at the FE phase which is favorable for the FE measurement. However, if the dielectric loss is more than 0.1, it becomes difficult to observe small polarization

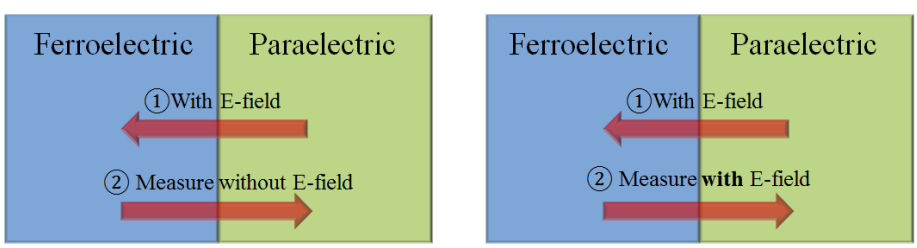


**Figure 2.1** Measurement procedure of the pyrocurrent/ME current, conventional method (left) and new method (right)

due to the huge background signal from the electric leakage. In the hexaferrite samples with huge polarization at room temperature, the polarization is measureable with loss of ~0.5, however, we should subtract the background as well. Second, we can carefully look at the shape of pyrocurrent. If the pyrocurrent shows asymmetric lambda (λ) shape, it is usually intrinsic FE transition, while broad and symmetric peaks usually come from trapped charge carrier.

The third clue is to measure the pyrocurrent/ME current in the presence of electric field. Most ferroelectric measurement should include poling procedure in which we apply electric field at paraelectric (PE) phase and move to ferroelectric (FE) phase by changing the temperature or magnetic field. In the conventional way, we turn off the electric field at the FE phase and measure the depolarizing current moving back to PE phase. In this case, we measure not only the depolarizing current but also the current from trapped charge carrier in the grain boundary. A. Sundaresan [2] suggested that the application of electric field during the measurement can remove the trapped charge effect and observe only intrinsic ferroelectric polarization. In addition, this can also enhance the small pyro/ME current and thus make it measureable [3].

Finally, in some materials such as $Ni_3TeO_6$, the sign of pyroelectric signal does not change upon changing the poling direction [4]. We call this kind of materials ‘pyroelectric’ material. Therefore, in order to confirm the ferroelectric property, we should measure for both poling directions and check whether the pyroelectric signal is reversed by the poling direction.

### 2.1.3. AC Magnetoelectric susceptibility (MES)

For the sensitive ME measurement, we used a lab-made ac ME susceptometer which is composed of a special solenoid coil [5]. We apply small ac magnetic field of 0.02-2 mT with 171 Hz by applying ac current to the coil with the lock-in amplifier. The induced change of the ac polarization flow out of the electrodes in the form of current, and the current is amplified to the voltage form in a high impedance charge amplifier with a gain factor of $10^{12}$ V/C. The voltage from the charge amplifier is measured from the lock-in amplifier with sensitive frequency and phase. The applied ac magnetic field is accurately measured from the voltage pick-up coil inside the solenoid using another lock-in amplifier. This measurement also includes same poling procedure as the pyro/ME current measurement. The unit of ME coefficient obtained from this measurement is written as

$$\alpha_{ME} = \frac{dP}{dH} \cong \left[\frac{C}{m^2}\right]\left[\frac{m}{A}\right] = \left[\frac{C}{m^2}\right]\left[\frac{s \cdot m}{C}\right] = \left[\frac{s}{m}\right] \quad (2.3).$$

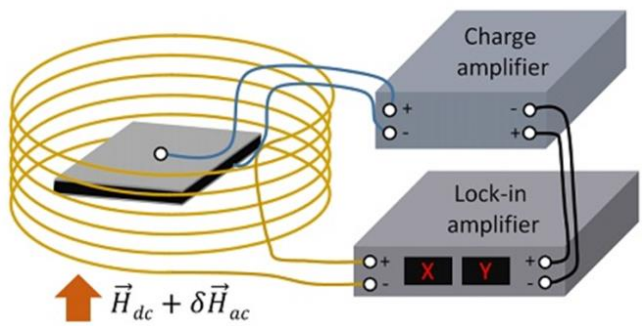


**Figure 2.2** Schematic illustration of the configuration of the ME measurements employed in the magnetoelectric susceptometer

### 2.1.4. Magnetic property

To investigate the magnetic properties, we used the vibrating sample magnetometer (VSM) which is one of the options in the 9 T PPMS$^{TM}$, whose resolution is ~$10^{-5}$ to $10^{-6}$ emu. The temperature dependent magnetic susceptibility ($\chi$) is a quantity of magnetization under a small magnetic field, thus it should be measured under the smallest magnetic field as long as it is measureable. For example, 0.01 T is enough to measure the unit of $\chi$ is usually expressed by [emu/g], [emu/mol], or [$cm^3$/mol] for the magnetic materials like $Fe_3O_4$. However, when we measure the materials with small $\chi$, we have to apply larger magnetic field. The unit of magnetization under magnetic field ($M$) is expressed by [$\mu_B$/f.u.] which means how many Bohr Magnetons per unit cell. The units are calculated from the magnetic moment (emu) we measure, as below.

$\chi_{mass} \cong$ [emu/g] = [ $m$ (emu) / magnetic field (Oe) / mass of sample (g)] (2.4)

$\chi_{mol} \cong$ [emu/mol] = [$cm^3$/mol]

= [ $m$ / magnetic field / mass of sample / molar mass] (2.5)

$M \cong$ [$\mu_B$/f.u.] = [ $m$ x molar mass / $\mu_B$ / Avogadro number / mass ]

= [ $m$ x molar mass / 5580.54 / mass ] (2.6)

## 2.2 Physical property measurements in pulsed field

The high magnetic field measurement up to 60 T is done for the $PbCu_3TeO_7$ single crystals in the National High Magnetic Field Laboratory (NHMFL) in Los Alamos. Since the high magnetic field is applied in short time of less than 1 s (details on the pulse field generation is explained in the Appendix A), we need

special care for the measurements; sometimes use totally different scheme from that of static field.

### 2.2.1. Electric polarization measurement

The polarization measurement is one of the easiest measurements in the pulsed field because the signal, which is proportional to the sweep rate of magnetic field, is generally high. From this measurement, we can investigate the magnetoelectric properties of samples in the high magnetic field. As the polarization in the sample changes under magnetic field, corresponding current flows out. We use a current amplifier SR 570 to amplify the current and convert to voltage with certain ratio. Then the voltage from the output is measured by the digitizer. The polarization can be calculated by the same method as that of pyro/ME current in static field.

We should set the sensitivity (input current-output voltage ratio) of the current preamplifier properly for the clear and correct measurements. If the sensitivity is too high (~1 nA/V), the signal to noise ratio is high, but response to the magnetic field change is slow. Meanwhile, if the sensitivity is too low (~1 μA/V), the signal to noise ratio is low, but response to the magnetic field is fast enough. We would better use the sensitivity of 20 nA/V or 50 nA/V in the pulsed field measurement.

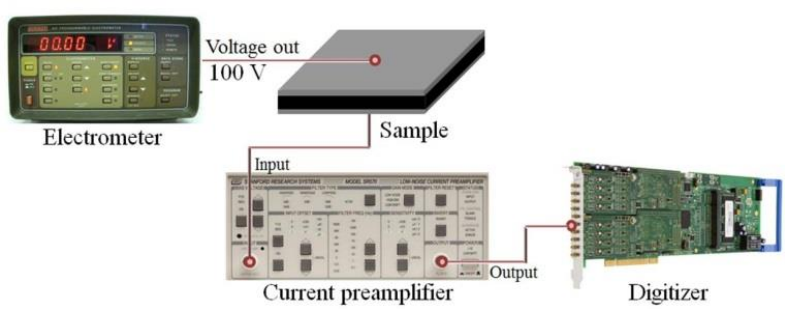


**Figure 2.3** Connection scheme for the electric polarization measurement in the pulsed field

We do not use the function of bias voltage, input offset and filters for this polarization measurement and use the gain mode of high BW.

In the case of general multiferroics in which there is finite electric polarization at zero magnetic field, we can pole the sample from above the transition temperature ($T_c$) to the target temperature below $T_c$. Then we turn off the poling voltage and measure the depolarizing current in the pulsed field. However, in the case that there is no polarization at zero magnetic fields, we cannot pole the sample before the measurement. Therefore we should cool down to target temperature, and measure polarization under the poling electric field. We apply electric voltage of 100 V on one side electrode of sample and measure the current from another side of electrodes. Then, crossing the ferroelectric phase boundary in the high magnetic field, we can measure the polarizing current. If the polarizing current under the rising field is intrinsic magnetoelectric responds, depolarizing current at same (or similar) magnetic field will be observed with opposite sign.

### 2.2.2. Magnetization measurement

In the pulsed field, we cannot use the squid magnetometer and vibrating sample magnetometer (VSM) due to the short time of application of the magnetic field. Therefore, magnetometers with cantilever [6] or pick-up coil [7] are usually used. We used the pick-up coil method to measure magnetization in this thesis.

The magnetometer is made of pick-up coils and compensation coil. The compensation coils compensate the voltage signal from the change of magnetic field, which is not intrinsic sample property. Before putting the sample inside the pick-up coil, we measure without sample, and we change the variable resistor

which is connected to the compensation coil until the signal becomes almost zero.

Then, we put the sample inside the pick-up coil and measure again. Finally, we subtract the signal with sample to the signal without sample, in order to obtain the intrinsic magnetization data.

The magnetization change under the magnetic field can be obtained by expression below.

$$\Delta M(t) = M(t) - M(0) = A\int_0^t V_{sample}(t') - V_{without\ sample}(t')dt' \qquad (2.7)$$

A is the calibration factor, which is not available in this measurement. Therefore, we need low field magnetization data with absolute value from squid or VSM to calibrate the magnetization in high magnetic field.

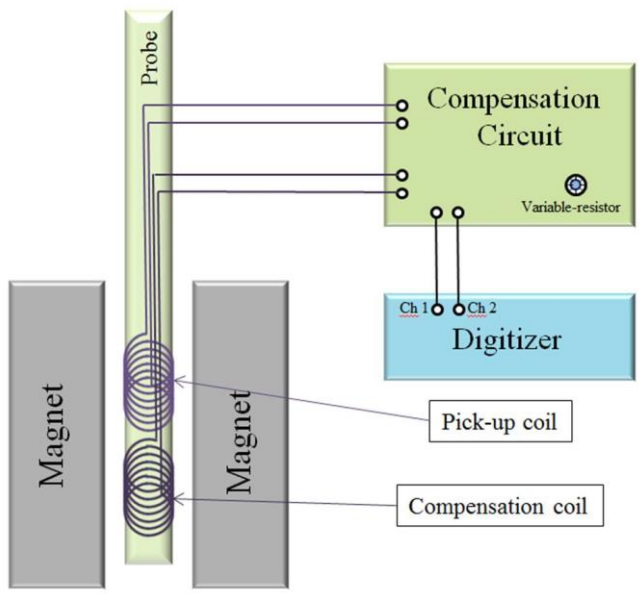


**Figure 2.4** Connection scheme for the magnetization measurement in the pulsed field

## 2.3 References


[1] G. Catalan, Appl. Phys. Lett. **88,** 102902 (2006)

[2] C. De *et al.,* Solid State Commun. **205**, 61 (2015)

[3] B. Koteswararao *et al.,* APL Materials **4,** 036101 (2016).

[4] Y. S. Oh *et al.,* Nat. Comm. **5,** 3201 (2014).

[5] Y. S. Oh, Ph. D. thesis (Seoul National University, 2010)

[6] E. Ohmichi *et al.,* Rev. Sci. Instrum.**73,** 3022 (2002).

[7] J. H. Espina-Hernandez *et al.,* Physica B **346,** 543 (2004).

# Chapter 3

# Quantitative measurements of size-dependent magnetoelectric coupling in $Fe_3O_4$ nanoparticles

## 3.1 Introduction

Magnetic nanoparticles have been extensively studied for the last decades due to their diverse biomedical applications, such as contrast agents for magnetic resonance imaging, hyperthermia, drug delivery, and bio separation [1-4]. However, their magnetoelectric (ME) properties, which allow for the modulation of electric polarization *P* (magnetization *M*) by a magnetic field *H* (electric field *E*) [5-6], have seldom been explored. The lack of work on ME properties mainly originates from the difficulties in determining the intrinsic ME coupling, particularly in the case of nanoparticles, due to their high electrical leakage and weak ME signals. Most previous studies on ME properties have thus been limited to bulk materials and thin composite films [7-9]. Meanwhile, ME nanoparticles, once realized, are expected to be useful for various applications, e.g., applying electrical stimuli for cell proliferation [10], preparing electrically responsive surface for functionalization [11], developing stimuli-responsive photonic crystals [12], and so on.

To search for possible ME nanoparticles, it is first necessary to understand the behavior of an archetypal ME material, namely the magnetite ($Fe_3O_4$), in nanoparticle form. As the oldest known loadstone material and with a ferrimagnetic

Curie temperature of 858 K, $Fe_3O_4$ exhibits an intriguing metal-insulator transition, known as the Verwey transition, at $T_v$ = ~123 K. The Verwey transition is accompanied by an intriguing charge ordering between $Fe^{2+}$ and $Fe^{3+}$ ions in the inverse spinel structure and a concomitant structural transition from a cubic to a monoclinic phase [13-15]. However, this unique but complex phase transition, involving entangled spin-charge-lattice degrees of freedom is not fully understood, and remains one of the long-standing conundrums in material physics [15]. Apart from this Verwey transition, bulk $Fe_3O_4$ has been known to become ME below its ferroelectric transition, located at around 10-38 K [16-18], at which point a triclinic phase transition also seems to occur [19]. Rado *et al*. [7-8] were the first to observe the linear and bilinear ME effects in bulk $Fe_3O_4$ at 4.2 K. Several subsequent studies on the ME effect [20], heat capacity [21] and magnetization [22] have uncovered an anomaly in the vicinity of 10 K, below which the ME coupling becomes sufficiently sizable to be measured. There have also been theoretical predictions that the ME effect arises from the peculiar charge/orbital ordering pattern involved in the Verwey transition and from the *p-d* hybridization mechanism related to the intrinsic spin-orbit interaction [23-24].

On the other hand, mainly due to the experimental difficulties described above, there has been no systematic study of the size dependence of ME properties in spherical $Fe_3O_4$ nanoparticles to date. However, progress in synthesis techniques has produced uniform, diameter-controlled nanoparticles, allowing for quantitative investigations of diameter-dependent physical properties [25-28]. For instance, a recent report [27] by Lee *et al*. showed that the Verwey transition temperature starts to decrease for $d \leq 20$ nm and eventually disappears for $d \leq 6$ nm.

In this chapter, we deal with the ME susceptibility (MES) of spherical $Fe_3O_4$ nanoparticles with a controlled, uniform diameter at various temperature and magnetic field conditions. In order to overcome the leakage currents arising from the conductivity of the nanoparticles, we mixed them into an insulating host material (Stycast$^{TM}$ 1266). Furthermore, we employed a custom-designed ME susceptometer with a high charge oscillation sensitivity of $10^{-17}$C [29-31]. The maximum MES (d*P*/d*H*) of 0.6 ps/m could be measured for nanoparticles with $d$ = 15 nm at 5 K. The MES is generally reduced as $d$ is decreased, but remains finite for $d \geq \sim 5$ nm. Moreover the temperature at which MES starts to appear is increased in the smaller nanoparticles, which could be explained by the core-shell effect.

## 3.2 Experimental method and results

### 3.2.1. Sample preparation for the measurements.

$Fe_3O_4$ nanoparticles with an averaged diameter ($d$ = 3, 5, 7, 12, and 15 nm) were prepared through one-pot thermal decomposition method by the Jinwoo Cheon's laboratory. The procedure to synthesize 15 nm $Fe_3O_4$ nanoparticles is as follows. $FeCl_2$ (3.25 mmol) and $Fe(acac)_3$ (5.00 mmol) were added to mixture of oleylamine (60.8 mmol), oleic acid (15.8 mmol) and trioctylamine (34.3 mmol) in a round-bottom flask under Ar atmosphere. Oleylamine and oleic acid was used as surfactants in the reaction. The reaction mixture was heated up to 300℃ and maintained at 300℃ for 1 hr. The resulting solution was cooled down to room temperature and added with excess ethanol to precipitate nanoparticles. The precipitated nanoparticles were re-dispersed in toluene and then washed with

ethanol and toluene several times. The sizes of the $Fe_3O_4$ nanoparticles were controlled by using different ratios of metal precursors and surfactants. To remove surfactants which act as insulating layer, ligand exchange was conducted with tetramethylammonium hydroxide (TMAOH) as following. The $Fe_3O_4$ nanoparticles were precipitated by centrifugation and 1M TMAOH/BuOH solution was added. The mixture was sonicated for few minutes and then the black precipitate was collected by centrifugation. The black precipitate was dried under vacuum for 60 mins. For a comparative study, we also investigated two commercially available $Fe_3O_4$ bulk powders with different impurity levels; one (bulk #1) is from Sigma-Aldrich (310069-Iron(II,III)oxide powder, <5 μm, 95%) with average particle diameter of $d$ = 3 ±1 μm, and the other (bulk #2) is from Alfa Aesar (12962-Iron(II,III)oxide powder, 99.997%) with particle diameters distributed from ~10 to 50 μm, denoted as $d$ > 10 μm.

For MES and dielectric constant measurements, the $Fe_3O_4$ nanoparticles and bulk powders were mixed with an insulating host matrix (Stycast™ 1266) and solidified under $H$ = 0.4 T in order to align them along the magnetic easy axis (Fig. 3.1). The volume fractions of the bulk powder and the nanoparticles in the insulating matrices were estimated from the measured density of the solidified Stycast™ with and without guest particles, and were later used for normalization of

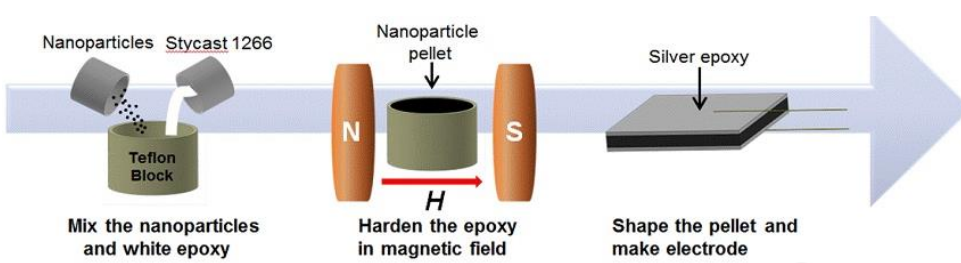


**Figure 3.1** Schematic illustration of the preparation of the nanoparticles

the obtained MES data. The solidified specimens were cut into thin plates with surface parallel to the initial *H* direction, to align the nanoparticles. Silver electrodes were painted on both sides of the plate, in order to make parallel capacitors.

### 3.2.2. Dielectric constant

Figure 3.2 shows the (a) dielectric constant and (b) loss tangent of $Fe_3O_4$ nanoparticles with $d$ = 15 nm as a function of magnetic field at various temperatures (5 -30 K). We added an offset to the data at each temperature for a

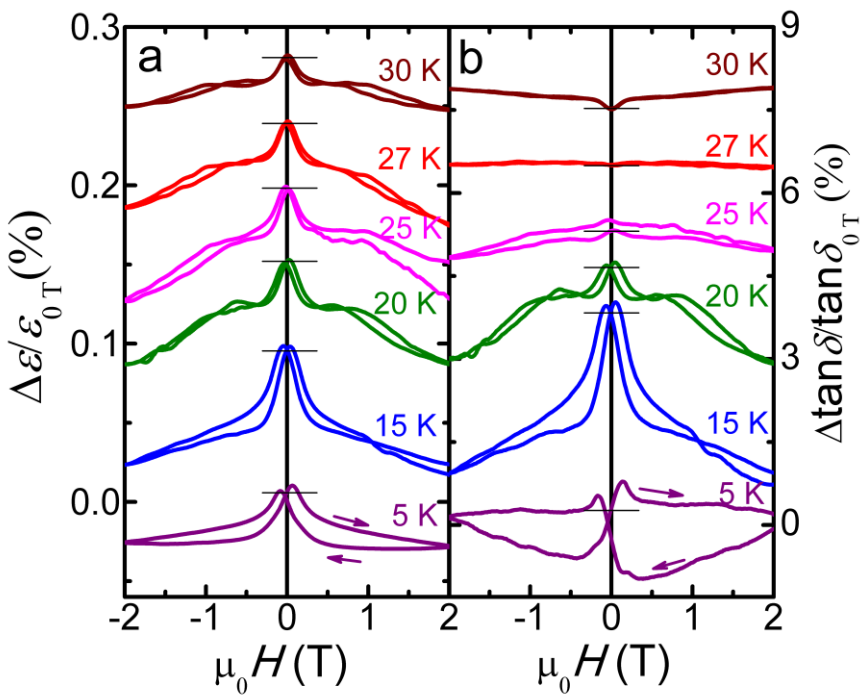


**Figure 3.2** Magnetic field dependence of (a) dielectric constant and (b) loss tangent curves of the $Fe_3O_4$ nanoparticles of $d$ = 15 nm at selected temperatures. The offset of each data is shown as a horizontal bar.

clear view. At all of the temperatures, there exists negative magnetodielectric (MD) effect and the variation is less than 0.1 % between $H$ = -2 and 2 T. In contrast, the sign of magnetoloss (ML), which is positive at above 27 K, changes into negative at the lower temperatures. The sign of MD and ML effect provides a clue to judge whether the MD effect is intrinsic or not. G. Catalan [32] claimed that MD effect can arise from the Maxwell-Wagner effects (magnetoresistance of magnetic materials), which indeed should result in the opposite signs of MD and ML effect. Based on this calculation result and the observation of the opposite signs between the MD and ML effect above 27 K in Figure 3.2., the MD effect above 27 K can be attributed to the extrinsic Maxwell-Wagner effect, which stems from the leakage and magnetoresistance of nanoparticles. On the other hand, the MD effect below 27 K seems to be intrinsic due to the ME properties of the nanoparticles. A similar phenomenon was reported in the $SiO_2$-coated $Fe_3O_4$ nanocomposites [33]. This data thus support that the leakage effect is negligible below 27 K so that the intrinsic ME effects can be investigated.

In addition, the temperature dependent dielectric constant is measured at zero magnetic fields in several frequencies. There are dielectric constant drop and dielectric loss peak at ~29.4 K for the frequency of 1 kHz [Fig 3.3]. The drop and peak position move to the 33.4 K and 38.4 K at 10 kHz and 100 kHz respectively. In comparison with conventional ferroelectrics, which exhibit frequency-independent dielectric constant peak at the critical temperature, the frequency dependent responds are not from ferroelectric phase transition but from the dynamic process. There are two possible origins of this frequency dependence; one is Maxwell-Wagner effect and another is relaxor ferroelectricity [18,34]. This kind

of phenomenon has been also shown both in the $Fe_3O_4$ thin film [18] and single crystals [34].

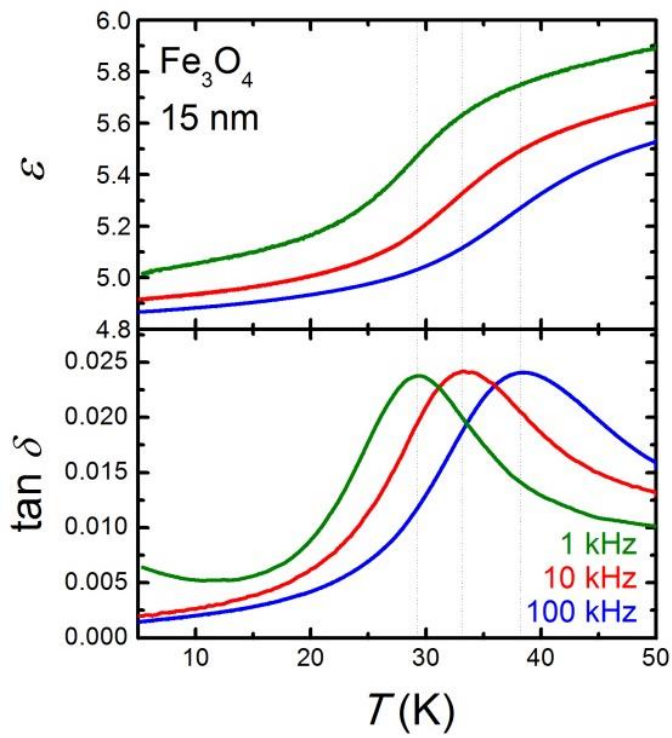


**Figure 3.3** Temperature dependence of dielectric constant (upper) and loss tangent (lower) curves of the $Fe_3O_4$ nanoparticles of $d$ = 15 nm at selected frequencies.

### 3.2.3. Magnetoelectric susceptibility (MES) and magnetic properties in 15 nm $Fe_3O_4$ nanoparticles.

In order to investigate tiny ME coupling in the $Fe_3O_4$ nanoparticles, we measured the MES with high sensitivity. Figure 3.4a shows the variation of MES (≡d*P*/d*H*) as a function of the bias magnetic field $H_{dc}$ for $Fe_3O_4$ nanoparticles with *d*=15 nm at *T*=5 K. When a positive electric field poling (+$E_P$) is applied and the magnetic field is reduced from 2 T, the MES increases up to the maximum of ~0.6 ps/m at 0.09 T and then decreases almost linearly to cross the intercepts of d*P*/d*H* (0.41 ps/m) and $H_{dc}$ (-0.06 T) axes. The MES behavior can be generally understood from a free energy $F(E,H)$ expansion under the application of electric field and magnetic fields (Equation 1.1, 1.2). The equation 1.2 shows that $\Delta P(0,H)$, in low field regions, can be approximately described by the *H*- linear and quadratic terms, if both $\alpha$ and $\beta$ are finite values. Note that, in the expression for d*P*/d*H*, the linear ME coefficient $\alpha$, if allowed in a material, remains as a constant, and the quadratic term $\beta$ is linear for a low *H* bias.

$$\frac{dP}{dH}(0,H) = \alpha + \beta H + \cdots \qquad (3.1)$$

The MES in figure 3.4a shows linear behavior for a low *H* bias which is often observed in a medium with a dominant strain-induced quadratic ME effect [29]. However, the shape of MES is not exactly asymmetric with respect to the *H* sign reversal, as expected only in the quadratic ME media; the absolute value of the maximum in d*P*/d*H* is clearly larger than that of the minimum in *dP*/*dH*, indicating that a linear ME coupling effect ($\alpha$) should also exist. Another noticeable feature in

Figure 3.4a is that the sign of d$P$/d$H$ is reversed with the change of the electric poling from a positive (+$E_P$) to a negative (-$E_P$) value. This is an expected behavior in ferroelectric media.

Figures 3.4b and 3.4c show the $H$-dependence of dielectric constant $\varepsilon$ and the square of the magnetization $M^2$ at 5 K for $Fe_3O_4$ nanoparticles with $d$=15 nm. The $\varepsilon$ data forms a hysteresis loop with butterfly shape, exhibiting maximum values at $H \approx \pm 0.06$ T. Similar butterfly loops have been observed in materials such as $Mn_3O_4$ [35], $NiCr_2O_4$ [36], and $BiMnO_3$ [37], in which the magneto-dielectric effects satisfying the relation $\varepsilon \propto M^2$ exist due to the presence of spin-phonon coupling. It is noteworthy that the hysteresis appearing in the $M^2$-$H$curve is much smaller than that of $\varepsilon$-$H$ curve. Furthermore, to determine whether the quadratic ME coupling, i.e., $P \propto M^2$, is sufficient to explain the ME coupling, we carefully compare the d$P$/d$H$ and d$M^2$/d$H$ curves [38]. The d$P$/d$H$- $H$ curve is indeed markedly different from the d$M^2$/d$H$ – $H$ curve in Fig. 3.4d; in particular, it shows a less perfectly asymmetric line shape with respect to $H$-direction change (Fig 3.4a). This observation also supports that the idea that $Fe_3O_4$ nanoparticles with $d$ = 15 nm should have both linear and quadratic effects as known for the bulk magnetite. The polycrystalline $Fe_3O_4$ pellet studied here (bulk #1) also exhibited almost same line shape as that of $Fe_3O_4$ nanoparticles, further supporting the presence of both linear and quadratic ME effect (Figure 3.9).

Figure 3.4e presents the MES data for $Fe_3O_4$ nanoparticles ($d$ = 15 nm) measured at 10, 15, 30 and 50 K. As temperature is increased, the MES value as well as the highest field at which MES disappears decrease rapidly, but the small MES signal with a maximum value of ~0.03 ps/m was persistently observable up to

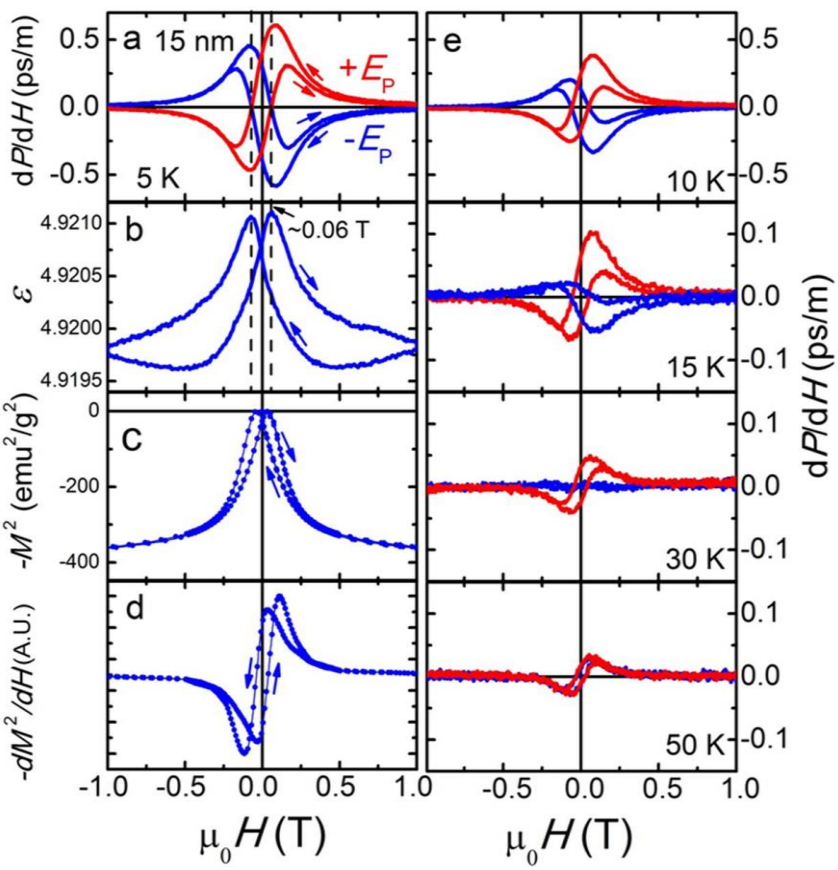


**Figure 3.4** Magnetic field dependence of (a) magnetoelectric susceptibility (MES) (=*dP*/*dH*), (b) dielectric constant ($\varepsilon$), (c) square of magnetization at 5 K, (d) field derivative of square of magnetization at 5 K and (e) MES of the $Fe_3O_4$ nanoparticles with $d$ = 15 nm at selected temperatures

50 K.

As the MES at 50 K shows an almost perfectly asymmetric line shape with respect to the sign reversal of *H*, the ME coupling is likely to be purely quadratic. However, for the negative poling ($-E_P$) at 50 K, the MES signal did not exhibit a perfect sign reversal as compared with the $+E_P$ case.

This implies that the specimen is not in a perfect ferroelectric state or a perfect magnetoelectric state at 50 K. The MES vs. *H* curve at 30 K looks quite similar to that at 50 K. Therefore, the small quadratic-like ME signals observed at 30 and 50 K for the $+E_P$ case might come from the magneto-striction of the $Fe_3O_4$ nanoparticles and resultant length modulation of Stycast™ via interface strain coupling between the Stycast™ and the $Fe_3O_4$, which have small piezoelectric [39]

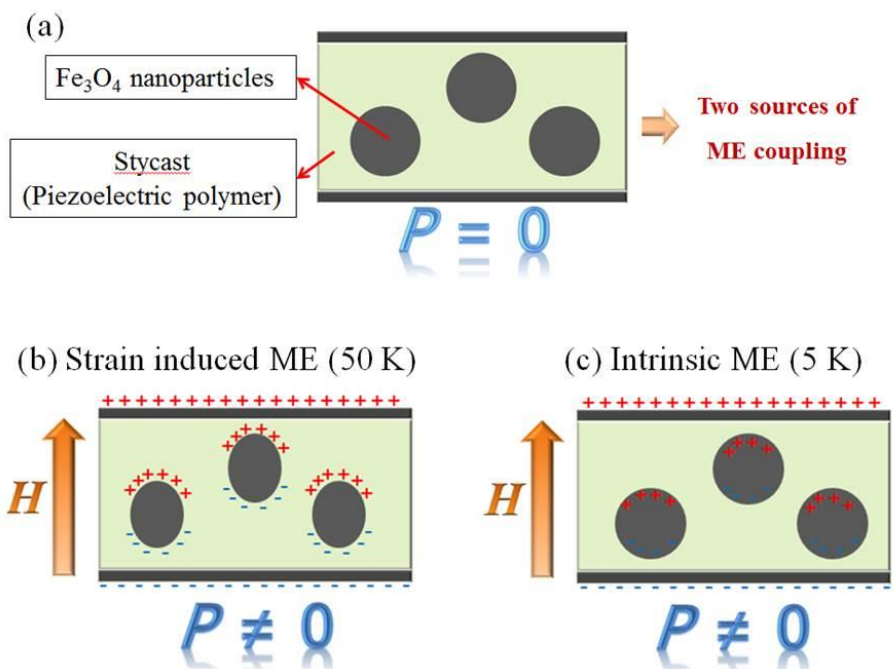


**Figure 3.5** Schematic illustration of the (a) $Fe_3O_4$ nanoparticles in the Stycast and (b) strain induced ME effect and (c) intrinsic ME effect in the $Fe_3O_4$ nanoparticles embedded in Stycast™.

and magnetostriction properties, respectively (Fig. 3.5(b)). On the other hand, we note that the d*P*/d*H* curves below 15 K exhibit a sudden increase in the overall MES magnitude as well as a noticeable difference in the absolute values of the maximum and minimum value of d*P*/d*H*. Moreover, the MES shows the sign reversal with respect to the poling direction change as expected in ferroelectric or linear ME media. This represents clear evidence of the drastically enhanced linear ME effect that is inherent to the $Fe_3O_4$ nanoparticles ($d$ = 15 nm) below 15 K (Fig 3.5(c)). Therefore, the MES data measured at low temperatures below 15 K should reflect the intrinsic ME coupling of the nanoparticles.

In order to analyze the *H*-dependent electric polarization, we integrated the MES (d*P*/d*H*) with *H*-field (Fig 3.6). The polarization decreases as sweeping down the *H*-field from 2 T and shows minimum value at -0.06 T before increasing again. It is noteworthy that variation of polarization value is asymmetric respect to the sign of

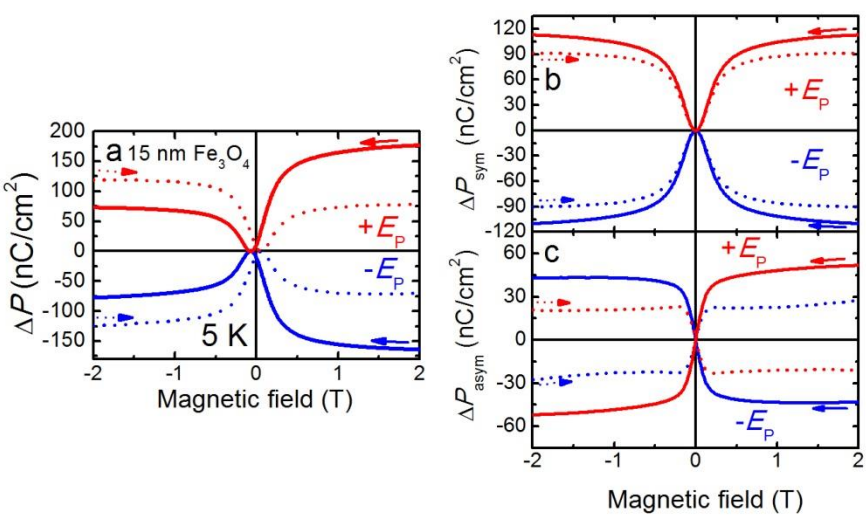


**Figure 3.6** Magnetic field dependence of (a) electric polarization of the $Fe_3O_4$ nanoparticles with $d$ = 15 nm at 5 K. Symmetry component (b) and asymmetry component (c) were calculated.

*H*-field. This indicates that both symmetric $\Delta P_{sym}$ (=($P(H)+P(-H)$)/2) and asymmetric $\Delta P_{asym}$ (=($P(H)-P(-H)$)/2) polarizations coexist in the $Fe_3O_4$ nanoparticles, similar to the case of the $Fe_3O_4$ single crystals. $\Delta P_{sym}$ and $\Delta P_{asym}$ indeed do correspond to the quadratic and linear ME effects, respectively, in the low *H* bias regime.

As *H*-field increases again from -2 T to 2 T, the polarization shows similar asymmetric shape with minimum value at 0.06 T. However, in comparison to the first down sweep (solid line), the polarization in the up sweep (dotted line) becomes smaller both for the symmetry and asymmetry components. When we sweep the *H*-field back and forth several times, the polarization decreases continuously (the data is not shown here). This phenomenon suggests that the polarization is depolarized whenever the *H*-field passes through the 0 T.

### 3.2.4. Magnetoelectric coupling of $Fe_3O_4$ nanoparticles with various diameters

Since we have confirmed that the MES data below 15 K reflects the intrinsic ME properties of nanoparticles, we next investigate the MES evolution with various *d* at 5 K, as summarized in Figure 5.7a. The maximum MES value for microparticles with $d > 10$ μm and $d = 3$μm, and nanoparticles with $d$=15, 12, 7, and 5 nm, all of which were embedded in Stycast™, were found to be 0.44, 0.48, 0.6, 0.25, 0.16 and 0.03 ps/m, respectively. The data implies that the maximum MES signals are more or less similar for a diameter range of 15 nm < $d$ < ~10 μm. Most importantly, the MES maximum starts to decrease systematically from $d = 15$ to $d = 7$ nm before almost disappearing for $d \leq 5$ nm.

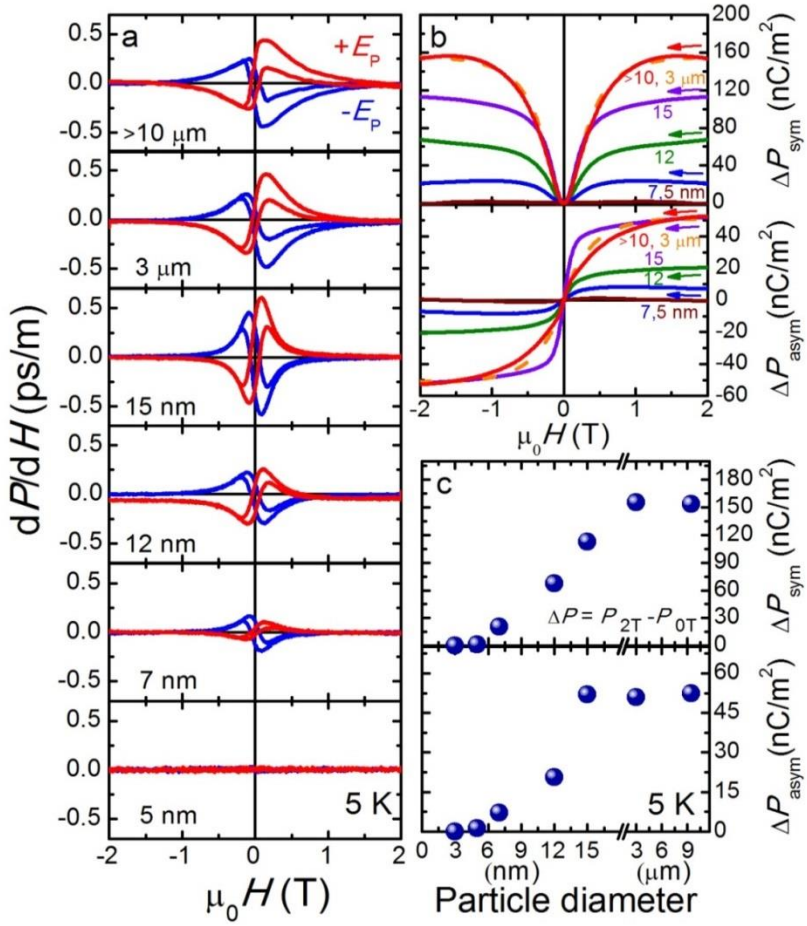


**Figure 3.7** Magnetic field dependence of (a) d*P*/d*H* and (b) polarization integrated from d*P*/d*H* curve resulting in symmetric and asymmetric shapes with respect to *H* in the $Fe_3O_4$ particles of various diameters. (c) The polarization difference between 0 and 2 T for the symmetric and asymmetric cases.

Based on the integration of the d$P$/d$H$ vs.$H$ data, we can extract $H$-dependent variation of the electric polarization ($\Delta P$-$H$) in the particles with various diameters. Figure 3.7 b,c summarizes the $\Delta P$-$H$ curves obtained from first sweep data for $+E_p$ in Fig. 3.7a. It is found that $\Delta P_{sym}$ starts to decrease monotonically from $d$ = 3 μm, whereas $\Delta P_{asym}$ decreases from $d$ =15 nm. Eventually, both $\Delta P_{sym}$ and $\Delta P_{asym}$ are suppressed such that they become negligibly small in nanoparticles with $d$ = 5 nm and completely disappear for $d$ = 3 nm.

The critical diameter for having an appreciable ME effect is then at least 5 nm. Interestingly, Lee *et al.* recently found that the Verwey transition disappears in nanoparticles with $d \leq 6$ nm, which is quite close to the critical diameter for observing the ME effect [27]. Therefore, our experimental findings corroborate the theoretical prediction that the ME effect in magnetite is linked to the peculiar charge-orbital-spin ordered state realized by the Verwey transition.

In sharp contrast to the decrease in the MES signal in nanoparticles with smaller diameters, we found that the MES signal survives for higher temperatures. Figure 3.8 (a) presents the MES of the nanoparticles as a function of temperature from 5 to 50 K, measured at the magnetic field where MES shows a maximum at 5 K. As clearly seen in Fig. 3.8a, the temperature $T_{ME}$ below which the MES starts to be significant, has systematically increased with reduced $d$ for both $+E_p$ and $-E_p$ cases. To estimate $T_{ME}$ consistently for each nanoparticle, we chose the temperature at which a base line and a linearly extrapolated line from the steeply increasing part of the d$P$/d$H$ curve meet. The dashed lines in Fig. 3.8a summarize $T_{ME}$'s values; 9.8, 15.6, 18.5, and 19.7 K for the micro-particles (bulk #2) with $d$ = 3 μm, and nanoparticles with $d$ = 15, 12, and 7 nm, respectively [the corresponding curves for

bulk #1 with $d > 10$ μm were almost same as that with $d = 3$ μm].

To understand the physical origin of the increase in $T_{ME}$ with reduced $d$, we measured $M$ vs $T$ curves at 10 mT and plotted their temperature derivative d$M$/d$T$ in Figure 3.8b. An anomalous peak (or maximum) in the derivative of magnetization (d$M$/d$T$) appears at 9.9 K for the $Fe_3O_4$ microparticles, indicating that the magnetization sharply decreases at the temperature. It turns out that the peak temperature is indeed close to the $T_{ME}$ = 9.8 K, below which the triclinic structural transition presumably occurs, increasing the ME effects in bulk $Fe_3O_4$. Upon decreasing the particle diameter, the temperature of the d$M$/d$T$ maximum

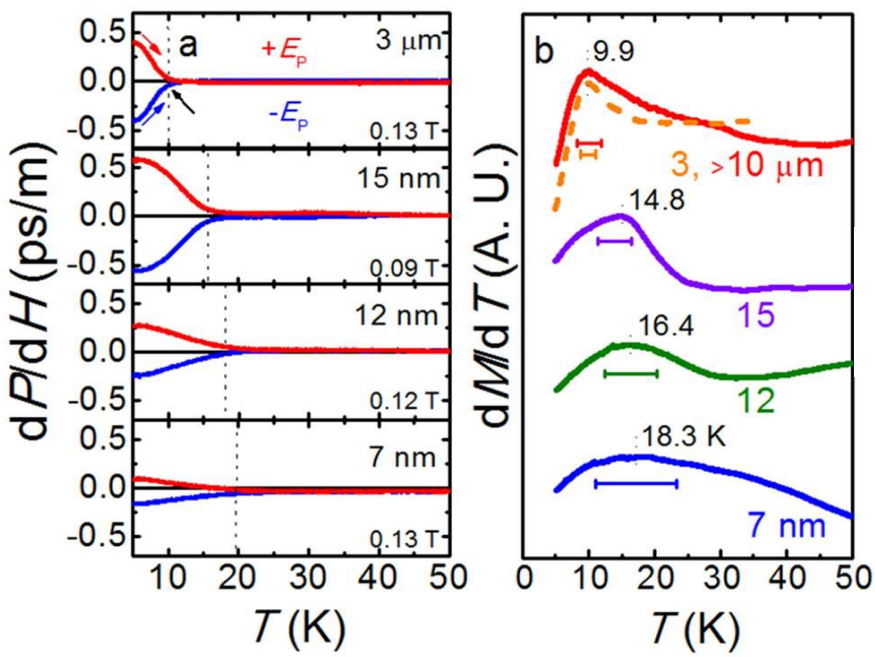


**Figure 3.8** (a) Temperature dependence of d$P$/d$H$ for $Fe_3O_4$ particles with $d$ = 3 μm, 15 nm, 12 nm, and 7 nm, all embedded in the Stycast™.(b) Temperature derivative of the magnetization (d$M$/d$T$) measured at $H$= 10 mT. The horizontal bar in each plot represents a temperature window that shows 3 % variation from the maximum value.

increases monotonically in rough proportion to $T_{ME}$; microparticles, the d$M$/d$T$ maximum almost coincides with $T_{ME}$, while for nanoparticles, it becomes slightly smaller overall. A close look at Fig. 3.8b reveals that the d$M$/d$T$ curves become progressively broader and exhibit weaker anomalies as the particle size is reduced. This indicates that the drop in magnetization gets shallower and broader. Therefore, the magnetization drop seems to occur in a broader temperature window as the surface effects become more important with the reduction of the particle diameter.

One appealing scenario to explain the above findings is the "core-shell" model expected in magnetic nanoparticles. In a recent study of related spinel $CoFe_2O_4$ nanoparticles which display a ferrimagnetic ordering at 860 K in their bulk state,

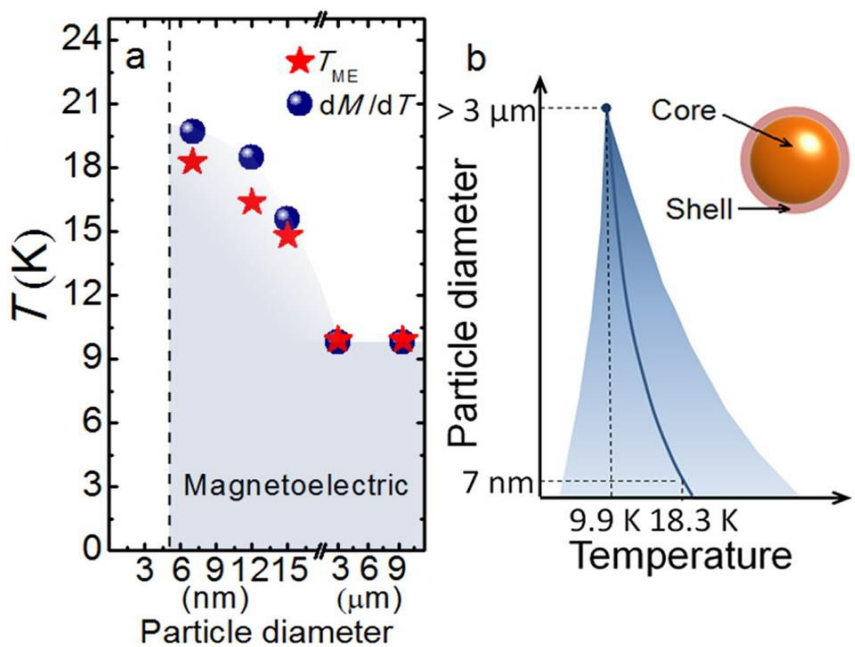


**Figure 3.9** (a) The maxima from the d$M$/d$T$ curve (asterisks) and $T_{ME}$ (solid circles) where the ME effect starts to increase steeply. (b) Illustration of the core-shell effect on the ME effect, resulting in the effective increase of $T_{ME}$ and the broadening of the d$M$/d$T$ curves in smaller particles.

Sun *et al* [40] found spectroscopic (phonon vibration modes) evidence that a core with aligned spins is surrounded by magnetically disordered shell.

Moreover, the vibrational mode analyses showed that the shell thickness of 0.4 nm in $d$ = 14 nm particles increased to 0.8 nm in 5 nm particles, demonstrating that an associated local distortion of the lattice takes place on the length scale of the unit cell. These experimental results by Sun *et al.* can be directly applied to understanding the size-dependent ME effect as well as the magnetization drop in the $Fe_3O_4$ nanoparticles. As the particle diameter is reduced, the magnetically disordered shell should increase in thickness. Moreover, the magnetically disordered shell seems to favor the stabilization of the triclinic structure over the monoclinic one at higher temperatures, possibly because the lower crystal symmetry becomes more compatible with the magnetically disordered spin state. As a result, the shell regions can display a concomitant structural and magnetic transition at high temperatures, the value which will have a distribution depending on the distance of each structural unit from the surface. The smaller the particle diameter, the broader can be the range of transition temperatures in the shell. Combined with the original magnetic transition in the core, the effective center temperature for the magnetic transition can be shifted toward higher temperatures, as illustrated in Fig. 5.8b. The conspicuously enhanced $T_{ME}$ in nanoparticles can then be attributed to the increased shell volume, which favors the stabilization of the magnetically disordered spin state and the triclinic phase at higher temperatures. We note that the present mechanism of the core-shell effect on ME properties is generally applicable to other nanomagnets exhibiting the ME effects.

### 3.2.5. Evidence of short range magnetoelectric interaction from the temperature dependent MES

In the temperature ($T$) dependent MES (= $dP/dH$) data (Fige 3.7a), the transition at $T_{ME}$ in which the ME coupling drastically decreases is not sharp. If we carefully zoom up the d$P$/d$H$ curves above $T_{ME}$ (Figure 3.10), which was determined by the linear extrapolation of the steeply increasing part, we can find that there exists a bifurcation between the two curves measured for $+E_p$ and $-E_p$ poling at high temperatures above $T_{ME}$. This small $dP/dH$ signals up to higher temperatures (~40 K) strongly indicate presence of the short range magnetoelectric coupling. We believe that this signal showing two different MES values with poling sign changes can only exist when there are ME domains (even if short-ranged) at high

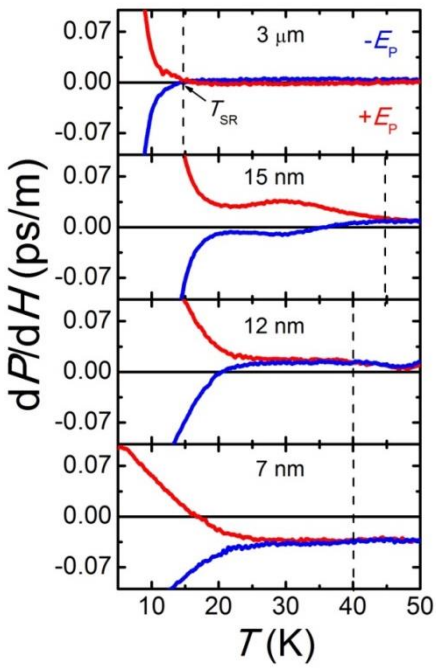


**Figure 3.10** Zoomed up temperature-dependent MES for each diameter of particles from Figure 4a, $T_{SR}$ represents the temperature in which the bifurcation of $+E_p$ and $-E_p$ data starts.

temperatures.

Therefore, if we take the temperature for having the bifurcation of the blue and red curves as the starting temperature of the short-ranged interaction ($T_{SR}$), the particles with $d$ = 3 μm, 15, 12, and 7 nm seem to have $T_{SR}$ = 15, 45, 40, and 40 K, respectively. Note that $d$ = 10 mm particles show almost same MES curves as that of $d$ = 3 μm. Our data thus indicate that the short range ME coupling at $T > T_{ME}$ is maximized in the nanoparticles with $d$ = 15 nm while for $d$ < 15 nm, the short range coupling seems to be much smaller than that of $d$ = 15 nm. The maximized short range interaction for 15 nm might originate from the core-shell effect in that the disordered shell part favors the short range magnetoelectric interaction. In further smaller particles, the reduced ME coupling at $T < T_{ME}$ may also weaken the short range interaction.

### 3.2.6. Magnetoelectric susceptibility (MES) of a $Fe_3O_4$ polycrystalline pellet

For comparison with the $Fe_3O_4$ nanoparicles mixed with Stycast™, a $Fe_3O_4$ pellet (bulk #1) was prepared without embedding in Stycast™. The $Fe_3O_4$ pellet is conducting at room temperature ($\rho$ = ~ a few Ωcm) and the resitivity increases with temperature lowering. The dielectric loss (tan $\delta$) was still high (>1) down to 30 K so that the sample could be poled only at $E_p$ = 125 kV/m, less than half of $E_p$ applied to the nanoparticle sample embedded in the Stycast. The magnetic field dependence of MES at 5 K exhibited almost the same line shape with the nanoparticles in Stycast™ (Fig 3.11). The MES data were not completely reversed by changing the poling direction, which is likely due to the highleakage in the

pellet and resultant insufficient poling voltage.

In the temperature dependence of MES, the large finite offset was found above 10 K, which again corroborates the existence of high leakage currents. On the other hand, the drops of MES between 5 K and 10 K seems quite consistant with the MES data of the samples embedded inthe Stycast™. Therefore, the observed ME effects in the samples embedded in the Stycast™ should be intrinsic properties of nanoparticles rather than coming from the mere strain coupling between $Fe_3O_4$ and Stycast™.

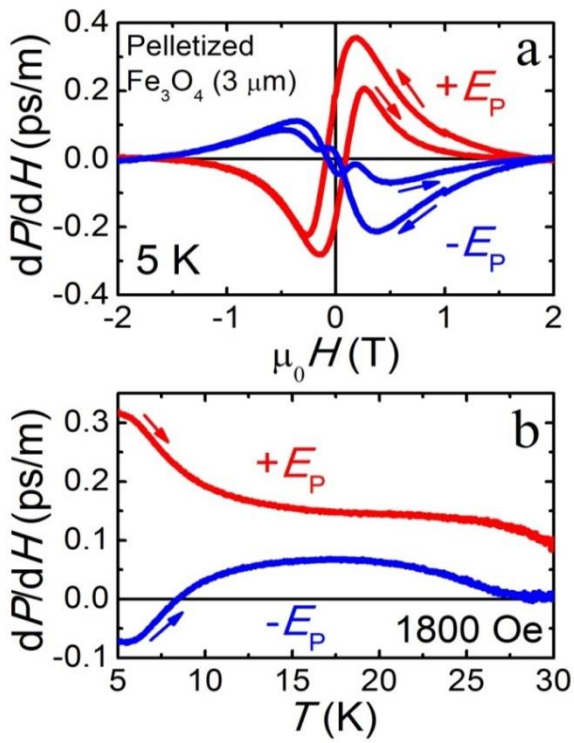


**Figure 3.11** (a) Magnetic field and (b) temperature dependent MES ($dP/dH$) of a pelletized $Fe_3O_4$ powder (not mixed with Stycast). The finite offset appearing in the $dP/dH$ curves is likely due to the presence of leakage currents in the pellet, which should distort the shape of $dP/dH$ vs $H$ curves in (a), showing a bit different shape between $+E_p$ and $-E_p$ poling cases.

### 3.2.7. In-phase and out-of-phase component of the MES data

Since the MES measurements generally employs an AC technique as we have stated in the text, there should exist in- and out-of-phase components. The actual MES data should thus have a complex form as

$$\tilde{\alpha}_{ME} = \alpha_{ME} + i\alpha''_{ME} \qquad (3.2)$$

where $\alpha_{ME}$ (defined as d$P$/d$H$ in the manuscript) is the in-phase component which represents the intrinsic ME coupling and can be proportional to the in-phase voltage signal with respect to ac magnetic field. Besides, $\alpha''_{ME}$ is proportional to an out-of-phase voltage signal in the phase-sensitive lock-in technique. The out-of-phase delta ($P$), i.e., the integration of $\alpha''_{ME}$ with $H$ can arise from two major

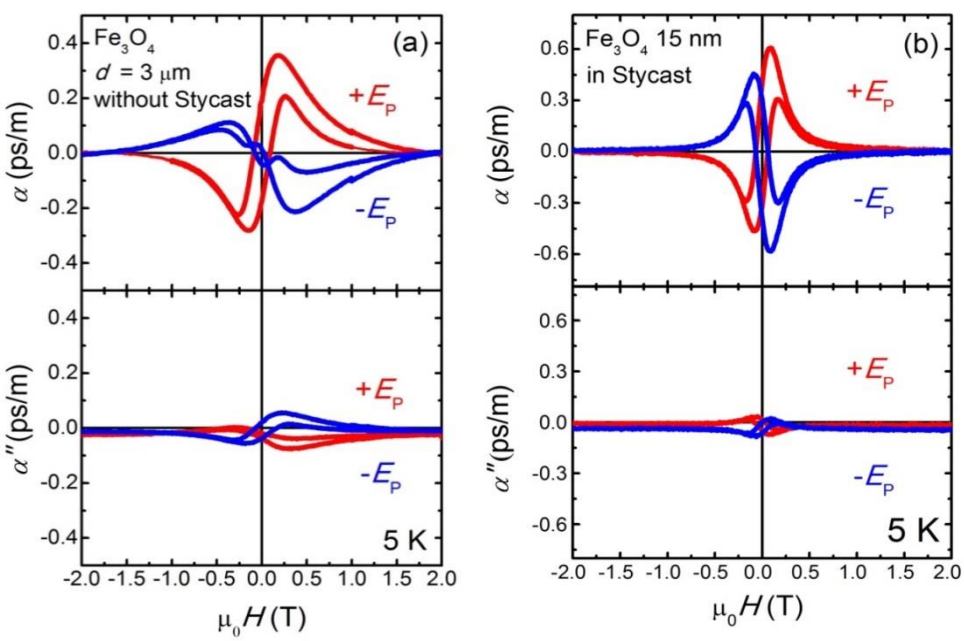


**Figure 3.12** In and out of phase of $H$ dependent MES of (a) the $Fe_3O_4$ bulk powder without Stycast and (b) $Fe_3O_4$ nanoparticles with $d$ = 15 nm in Stycast™

sources, i.e., the electric leakage of the sample itself and the eddy current mainly coming from the electrodes. An easy way of understanding the first origin is to consider that delta $P$ = delta $(\tilde{\varepsilon}E) =$ delta $(\tilde{\varepsilon}Vd)$, leading to the delta $V$ = delta $P/\tilde{\varepsilon}d$. Therefore, the out of phase of delta $V$ can arise when the imaginary part of $\tilde{\varepsilon}$, proportional to the leakage (conductivity) of the specimen, exists in the sample. Besides, the eddy current in the electrode or metallic region of the samples is proportional to the $i_{eddy} = v_{eddy}/R = \mathrm{d}H/\mathrm{dt}$. Therefore, the voltage output from the eddy current should be out of phase to the $H$ oscillation because d$H$/dt should change the phase by 90 deg with respect to that of the $H$ oscillation. In the actual experiments, we could reduce such an out-of-phase component of delta $P$ or delta $V$ because the nanoparticles in the Stycast™ have resulted in reduced leakage current inside the specimen and also minimized the possible eddy current effect coming from the wide conducting sample surface. Figure 3.12(a) shows that the MES of a $Fe_3O_4$ bulk powder without Stycast™ showed that the maximum out-of-phase value is ~16 % of the in-phase component, whereas the maximum out-of-phase component in the $Fe_3O_4$ nanoparticles in Stycast™ is only ~7 % of the corresponding in-phase value (Fig 3.12(b)). We have thus verified that the out-of-phase of the delta ($P$) in a leaky bulk sample can be reduced significantly in the insulating nanoparticles embedded in the Stycast™.

### 3.2.8. Magnetic susceptibility curves and oxygen stoichiometry

In $Fe_3O_4$, the physical properties are known to be very sensitive by the oxygen stoichiometry [41,42]. Especially, just ~1% of off-stoichiometry of oxygen can drastically change the Verwey transition temperature to ~85 K and make it broad

[41] and the 3 % even gets rid of the Verwey transition. In addition, a drop in ac susceptibility at ~40 K in stoichiometric sample becomes ~20 K with 0.2 % of off-stoichiometry. In our results, the magnetic susceptibility curve in bulk sample shows obvious drop at the Verwey temperature of 124 K, however, the drop is not observable in the nanoparticles. This claims that the nanoparticles have oxygen off-stoichiometry of more than 3 %.

In that sense, the ME properties can become untrustworthy if it is sensitive to the oxygen stoichiometry. In order to examine this effect, we compared MES of bulk $Fe_3O_4$ with low purity (95 %, bulk #1) and high purity (99.997 %, bulk #2). The Figure 3.7 (a) shows that the MES of the two samples has almost same line shape. This support that the ME effect is not sensitive to the oxygen stoichiometry and the ME properties are intrinsic properties of $Fe_3O_4$ nanoparticles.

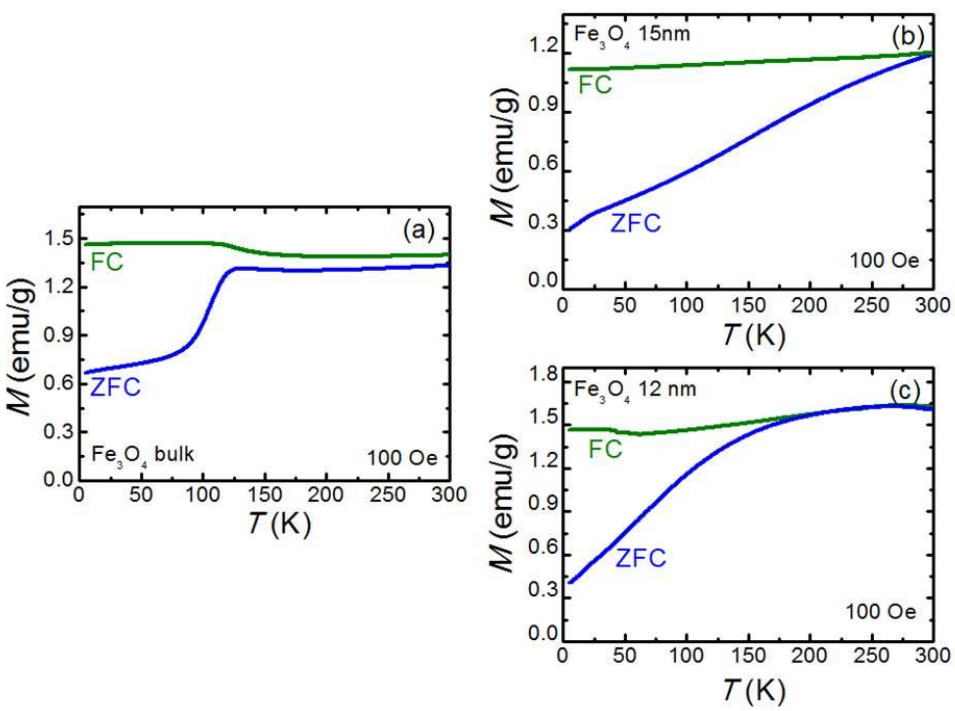


**Figure 3.13** The magnetic susceptibility of the $Fe_3O_4$ particles with Stycast with diameter of 3 μm, 15 nm, and 12 nm.

## 3.3 Summary

In summary, we successfully measured the ME coupling of spherical $Fe_3O_4$ nanoparticles with systematic variation of the diameter from $d$ = 15 nm to 3 nm, by embedding the particles into a polymer host. When the diameter of $Fe_3O_4$ nanoparticles is reduced, at the lowest temperature of 5 K, the ME coupling becomes weaker and eventually disappears at a critical diameter of 5 nm. On the other hand, the ME coupling persists to higher temperatures up to ~ 20 K in the nanoparticles with $d$ = 7 nm, which could be understood as a result of the core-shell effect with the magnetically disordered spin state in the shell. The observation of size-dependent ME properties in $Fe_3O_4$ nanoparticles should further stimulate the exploration of new ME effects and their applications in other nanomaterials.

## 3.4 References


[1] S. Laurent *et al.,* Chem. Rev. **108,** 2064 (2008).

[2] W. Wu *et al.,* Nanoscale Res. Lett. **3**, 397 (2008).

[3] Y.-W. Jun *et al.,* Acc. Chem. Res. **41,** 179 (2008).

[4] N. Lee *et al.,* Chem. Soc. Rev. **41,** 2575 (2012).

[5] T. Kimura *et al.,* Nature **426,** 55 (2003).

[6] N. Hur *et al.,* Nature **429,** 392 (2004).

[7] G. T. Rado *et al.,* Phys. Rev. B **12,** 5166 (1975).

[8] G. T. Rado *et al.,* Phys. Rev. B **15,** 290 (1977).

[9] H. Zheng *et al.,* Science **303,** 661 (2004).

[10] C. Ribeiro *et al.,* Colloids Surf. B **140,** 430 (2016).

[11] E. Cantini *et al.,* Acc. Chem. Res. **49,** 1223 (2016).

[12] T. Lu *et al.,* Nanotechnology **27,** 122001 (2016).

[13] E. J. Verwey, Nature **144,** 327 (1939).

[14] F. Walz *et al.,* J. Phys.: Condens. Matter **14,** R285 (2002).

[15] M. S. Senn *et al.,* Nature **481,** 173 (2012).

[16] Y. Miyamoto *et al.,* J. Phys. Soc. Japan **55,** 660 (1986).

[17] M. Alexe *et al.,* Adv. Mater.**21,** 4452 (2009).

[18] M. Ziese *et al.,* J. Phys.: Condens. Matter **24,** 086007 (2012).

[19] C. Medrano *et al.,* Phys. Rev. B **59,** 1185 (1999).

[20] Y. Miyamoto *et al.,* J. Phys. Soc. Japan **46,** 1947 (1979).

[21] S. Todo *et al.,* J. Phys. Soc. Japan **43,** 1091 (1977).

[22] M. Matsui *et al.,* J. Phys. Soc. Japan **43,** 47 (1977).

[23] J. Brink *et al.,* J. Phys.: Condens. Matter **20,** 434217 (2008).

[24] K. Yamauchi *et al.,* Phys. Rev. B **85,** 085131 (2012).

[25] S. Sun *et al.,* J. Am. Chem. Soc. **126,** 273 (2003).

[26] J. Park *et al.,* Nat. Mater. **3,** 891 (2004).

[27] J. Lee *et al.,* Nano Lett. **15,** 4337 (2015).

[28] S.-H Noh *et al.,* Nano Lett. **12,** 3716 (2012).

[29] Y. S. Oh *et al.,* Appl. Phys. Lett. **97,** 052902 (2010).

[30] H. Ryu *et al.,* Appl. Phys. Lett. **89,** 102907 (2005).

[31] K. –T. Ko, *et al.,* Nature Commun. **2,** 567 (2011).

[32] G. Catalan, Appl. Phys. Lett. **88,** 102902 (2006).

[33] C. Chang *et al.,* J. Appl. Phys. **108**, 094105 (2010).

[34] F. Schrettle *et al.,* Phys. Rev. B **83,** 195109 (2011).

[35] R. Tackett *et al.,* Phys. Rev. B **76,** 204409 (2007).

[36] T. D. Sparks *et al.,* Phys. Rev. B **89,** 204405 (2014).

[37] T. Kimura *et al.,* Phys. Rev. B **67,** 180401 (2003).

[38] Y. Zhou *et al.,* Appl. Phys. Lett. **101,** 232905 (2012).

[39] A. Troge *et al.,* J. Acoust. Soc. Am. **128,** 2704 (2010).

[40] Q. –C. Sun *et al.,* ACS nano **6,** 4876 (2012).

[41] J. P. Shepherd *et al.,* Phys. Rev. B **43** 8461 (1991).

[42] Z. Svindrych *et al.,* Phys. Rev. B **86** 214406 (2012).

# Chapter 4

# Magnetically-induced ferroelectricity in the *S*=1/2 staircase kagome compound $PbCu_3TeO_7$

## 4.1 Introduction

There has been a revived surge of research activity on multiferroics and magnetoelectric (ME) materials since early 2000s due to the fundamental interests on the physics of strong coupling between spin and lattice degrees of freedom and application potential for numerous low-power electronic devices [1-5]. In particular, ferroelectric polarization induced by spin order realized in magnetic ferroelectrics has drawn particular attention due to their strong spin-lattice (phonon) coupling and related mechanisms. In those magnetically induced ferroelectrics, spin frustration plays a key role to induce uncommon spin structure such as noncollinear spin order, which breaks inversion symmetry and thus induces an electric polarization (*P*) [4-5]. Numerous magnetic ferroelectrics have now been discovered in various spin frustrating networks such as triangular, kagome, spinel, quasi-one-dimensional lattices; e.g. $CuFeO_2$ [6-7], $Ni_3V_2O_8$ [8-16], $CoCr_2O_4$ [17], $MnWO_4$ [18]. All those structural motifs contain competition between the nearest- and next nearest-neighbor spin interactions to cause the spin frustration.

Among those spin frustrated networks, the kagome spin structure has been archetypal as its high degree of spin frustration can induce a new spin ground state, i.e., a quantum spin liquid state [19]. Therefore, many researchers have explored a

possibility of realizing 2D quantum spin liquids in the kagome structure. On the other hand, multiferroic properties in the kagome structure have been rarely known. To our knowledge, the first renowned kagome multiferroic compound is $Ni_3V_2O_8$, in which $Ni^{2+}$ ($S$=1) spins form a buckled form of the kagome structure called kagome staircase. Extensive studies on $Ni_3V_2O_8$ have now made significant progresses in understanding its intriguing ME coupling and complex phase diagram [8-16]. Upon cooling, $Ni_3V_2O_8$ exhibits four magnetic phases below 9.3 K, known as two high and low temperature incommensurate phases (named as the HTI and LTI phases) and two commensurate phases. Ferroelectricity is found only in the LTI phase, in which several neutron diffraction studies have uncovered stabilization of a spin cycloid in the *ab* plane. Therefore, the origin of spontaneous $P$ could be understood by the inverse Dzyaloshinskii-Moriya (IDM) interaction [28].

In terms of multiferroics/ME materials with spin frustration, the $S$=1/2 systems containing $Cu^{2+}$ ions have drawn particular interests mainly due to several reasons such as the opportunity of achieving high ordering temperatures from the large exchange interaction [20-21] and observing quantum fluctuations in the multiferroic properties [22-23]. A number of multiferroic/ME compounds with $S$=1/2 chains have been indeed found: CuO [20], $CuBr_2$ [21], $LiCu_2O_2$ [22], $SrCuTe_2O_6$ [23], $LiCuVO_4$ [24], $CuCrO_4$ [25], $CuCl_2$ [26], and $PbCuSO_4(OH)_2$ [27]. These compounds mostly share a common feature of $CuO_2$ ribbons with edge-sharing $CuO_4$ square planes. Therefore, the nearest neighbor spin interaction through Cu-O-Cu path can compete with the next nearest neighbor interaction through Cu-O-O-Cu path, resulting in a cycloidal spin order. Spontaneous electric

polarization ($P$) can be then induced by IDM interaction [28-30]. However, the realization of ME effect or multiferroics in the staircase kagome spin structure with $S$=1/2 Cu ions has not been reported so far.

We have recently found that $Cu^{2+}$ ($S$=1/2) ions in $PbCu_3TeO_7$ [31-32] forms the kagome staircase structure. The previous studies of magnetization [31], heat capacity [31], and nuclear magnetic resonance (NMR) studies [32] showed that $PbCu_3TeO_7$ had two antiferromagnetic transitions at $T_{N1}$ = 36 K and $T_{N2}$ = 24 K, and finally a small change in magnetic susceptibility assigned as $T_{N3}$ = 17 K. The Curie-Weiss temperature of $\theta_{CW}$ = -150 K obtained from the magnetic susceptibility indicated the presence of moderate spin frustration. In addition, strong interlayer interaction through the Cu-O-Te-O-Cu path was evident in the NMR measurement [32]. However, multiferroic and magnetoelectric properties have not been found so far.

In this chapter, we report the observation of magnetic field-induced ferroelectricity in $PbCu_3TeO_7$, a new staircase kagome system with $S$=1/2 ($Cu^{2+}$) ions. We find that below $T_{N2}$ = 24 K, $P_a$ is generated under $H_c$ > 8.3 T and 16 T < $H_a$ < 38 T, both of which are accompanied by the spin-flop (SF) transitions. We establish the phase diagram of $PbCu_3TeO_7$ for each $H$ direction based on the electric and magnetic properties. Based on the exchange interactions obtained by the first principles calculation, Monte Carlo simulations have been performed to uncover the spin configurations in each phase. Our calculations suggest that the $P_a$ generation under $H_c$ > 8.3 T stems from the spin-flop-induced cycloid phase rotating in the *ab*-plane.

## 4.2 Lattice structure

$PbCu_3TeO_7$ crystalize in a Pnma space group in orthorhombic structure. $PbCu_3TeO_7$ consists of Cu atoms forming the staircase kagome planes which are stacked along the a-direction and separated by Pb, Te atoms with small interlayer distance of ~4 Å (Fig 4.1). The lattice parameters were obtained from the Rietveld refinement of powder XRD pattern as $a$ = 10.484 Å, $b$ = 6.347 Å, and $c$ = 8.807 Å [31]. Figure 4.1(d) shows the possible intra-plane exchange interactions labeled from $J_1$ to $J_8$ in order of distance between two Cu atoms.

The first-principle density functional theory (DFT) calculation revealed that the hoping energy of $J_3$ is the strongest and that of $J_8$ is the second strongest [31]. It is noteworthy that the interlayer distance is not long, thus the interlayer interaction is not negligible.

## 4.3 Experimental method and results

### 4.3.1. Sample preparation

Single crystals of $PbCu_3TeO_7$ were grown using flux method. First, $PbCu_3TeO_7$ polycrystalline sample was prepared by solid-state reaction method using the starting materials of PbO, CuO and Te. They were ground with a molar ratio of 1:3:1, and heated at 750 ℃ for five days with 3 intermediate grindings. In order to grow single crystals, the polycrystalline of $PbCu_3TeO_7$ and NaCl/KCl flux (molar ratio 1:1) were mixed with mass ratio of 1:2. The mixture was heated at 800 ℃ for 24 h and then cooled to 650 ℃ at a rate of 1 ℃/h. The single crystals were extracted by washing with hot water. For the electric measurements, we shaped the

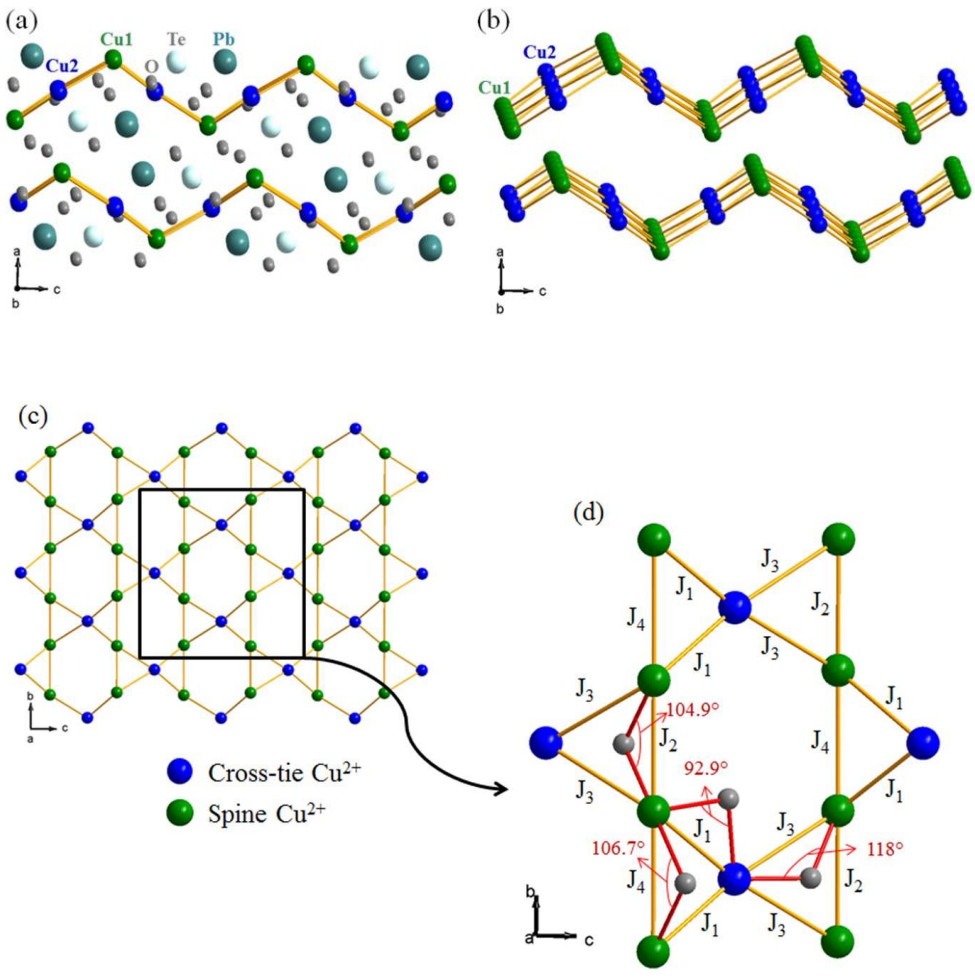


**Figure 4.1** The crystal structure of $PbCu_3TeO_7$ viewed along the b-direction including (a) all atoms and (b) only Cu and along (c) a-direction shows the staircase kagome lattice which consists of spine Cu ion (green) and cross-tie Cu ion (blue). (d) The possible exchange interactions between the Cu ions in the kagome layer. They were denoted from $J_1$ to $J_8$ in order of distance.

single crystal into the thin plate form whose surface is normal to the crystal a-axis. The shaped crystal size was quite small with area of 0.13 $mm^2$ and thickness of 140 μm. The electrodes on the both sides of the plate were made with silver epoxy.

### 4.3.2. Magnetoelectric effects in $PbCu_3TeO_7$ poly crystal

We first measured magnetoelectric properties of $PbCu_3TeO_7$ as shown in figure 4.2. The peaks in the pyrocurrent were not observed in zero field, but observed only in the magnetic field at $T_{N2}$ ~ 24 K. As the magnetic field is increased, the magnitude of pyrocurrent drastically increased. When we change the poling direction, the sign of pyrocurrent also changed, which verifies the ferroelectric

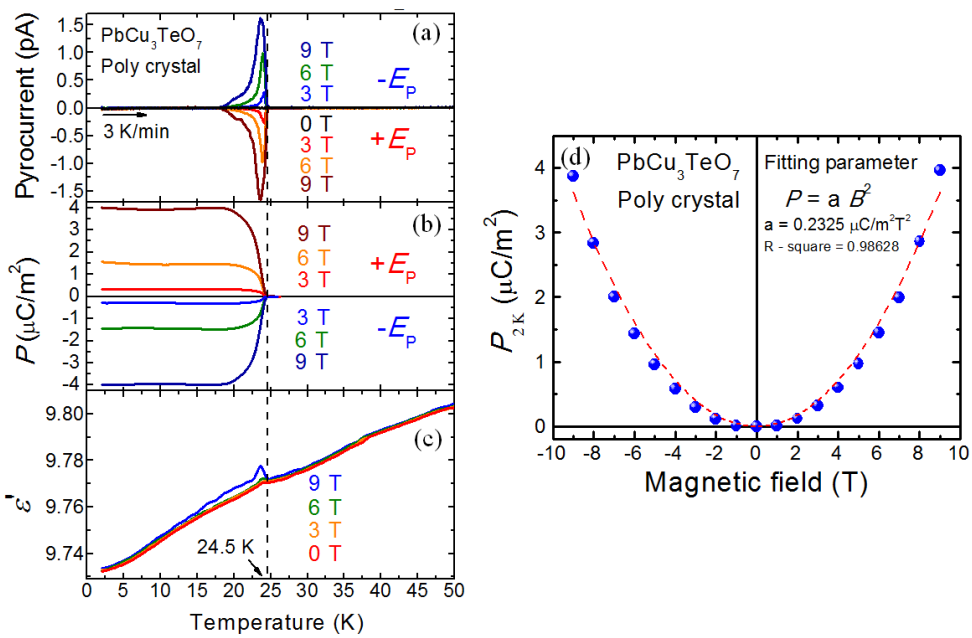


**Figure 4.2** Temperature dependence of (a) pyrocurrent, (b) polarization, and (c) dielectric constant in the $PbCu_3TeO_7$ poly crystal, and (d) magnetic field dependent variation of polarization at 2 K, which show quadratic ME effect.

property. The electric polarization, obtained by the integration of the pyrocurrent, is almost same at low temperature, and drastically decreases from ~20 K until it disappears at $T_{N2}$.

It is noteworthy that the $T_{N2}$ is the antiferromagnetic ordering temperature along the c-direction. We plotted the polarization at 2 K in different magnetic fields (Fig 3.2(d)), and found that the polarization increases quadratically, thus showing quadratic magnetoelectric effect. The quadratic curve fitting was done with the quadratic magnetoelectric coefficient of a = 0.2325 $\mu C/m^2T^2$. In the temperature dependent dielectric constant, there is a small zero field peak at $T_{N2}$ and the peak increases as the field increases.

In order to investigate the magnetic field dependent properties directly, we measured ME current at 2 K (Fig 4.3(a)) sweeping down (red line) and up (blue line). The linear ME coefficient calculated from the ME current shows linear behavior at low field, and shows peaks of 1.43 ps/m at ±8.25 T before decreasing again up to 9 T. The sign of the ME current is reversed as we change the sweep direction, which is reasonable result from same *P-H* curve. The calculated polarization (Fig 4.3(b)) exhibits obvious quadratic behavior at low field and shows small jump at ±8.25 T and maximum polarization of $P$ = 3.85 $\mu C/m^2$ at 9 T. In addition, the magnetization curve (Fig 4.3 (c)) have small jump at ±8.25 T which is shown as peaks in the d$M$/d$H$ curve. The figure 4.3 (d,e) shows that the ME current and polarization shows almost same curve until 20 K, but suddenly starts to decrease until disappearing at $T_{N2}$. The summarized polarization curves in figure 4.3(f) from the field dependent measurement are almost same as the curves from temperature dependent measurements in figure 4.2.

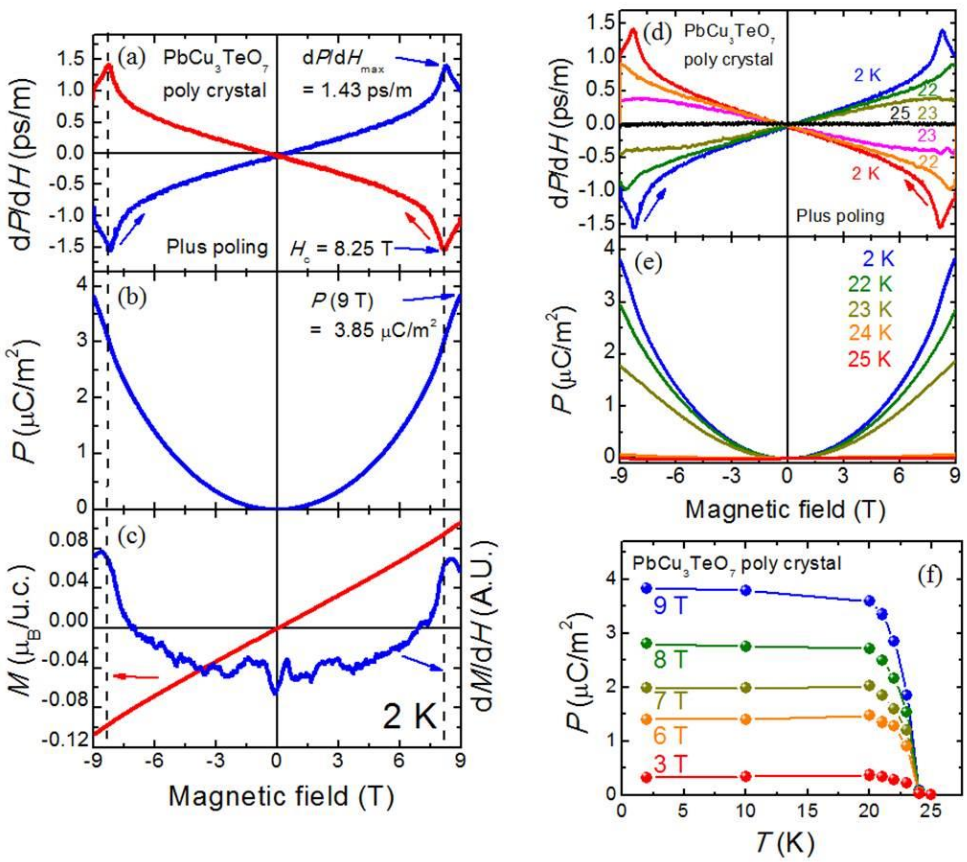


**Figure 4.3** Magnetic field dependence of (a,d) ME current, (b,e) polarization, and (c) magnetization in the $PbCu_3TeO_7$ poly crystal at (a,b,c) 2 K and (d.e) various temperatures and (f) temperature dependent variation of polarization from the (e).

### 4.3.3. Magnetoelectric effects in $PbCu_3TeO_7$ single crystals

The figure 4.4(a) shows the XRD data of the $PbCu_3TeO_7$ single crystal along the [011] direction. As we can see in the inset pictures, the single crystal long rod shape along the *a*-direction with length of ~1 mm, and it has small rhombus shape (<0.5 mm) on the *bc* plane. As the lattice constant of *c*-direction is longer than the b-direction, it is easy to decide the *c*-direction as the longer direction of the rhombus. Note that the *bc*-plane is the plane of Kagome layers. Laue pattern of the crystal also confirmed the crystal axis.

The magnetic susceptibility data along each direction presented in figure 4.4(b) shows the significant anisotropic magnetic properties which are consistent with the previous report [31]. For *H*//*a*, there is a clear evidence of antiferromagnetic (AFM) ordering below $T_{N1}$ ~ 36 K, whereas the AFM ordering realized below $T_{N2}$ ~ 24 K for *H*//*c*. A small anomaly at $T_{N3}$ ~ 17 K is prominent in *H*//*a*. However, there is no obvious magnetic ordering shown for *H*//*b*.

Figure 4.5(a) shows the pyroelectric current for several magnetic fields along the *c* direction. We used the conventional way by electrically poling the sample with $E_p$ = 7.7 kV/cm at 50 K and each magnetic field before cooling to 2 K. Then, we turned off the $E_p$, shorted electrically between the two electrodes, and measured the pyrocurrent warming up with rate of 3 K/min. There was no pyrocurrent visible with noise level of ~3 fA up to 5 T, however, a small peak at ~24 K was observed for 6 T. The peak became larger and sharper at higher field, prominently between 8 T and 9 T. The sign of pyrocurrent was reversed when we applied the negative electric poling ($-E_P$) (not shown here), which is an expected behavior in ferroelectric materials.

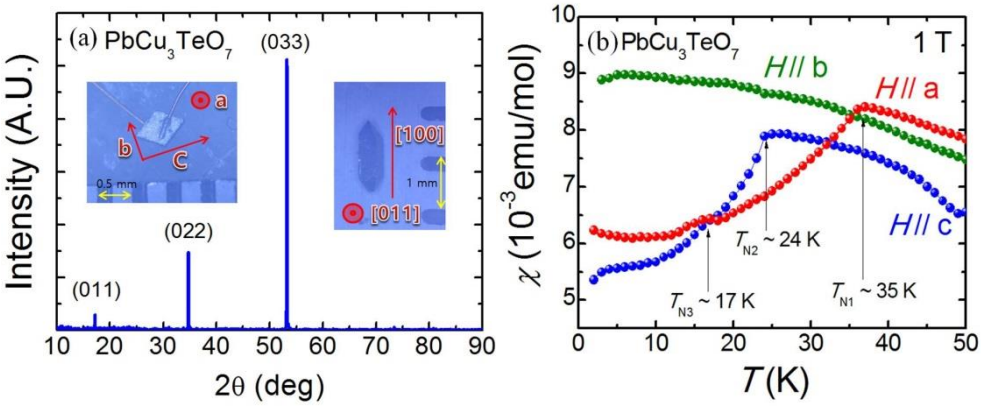


**Figure 4.4** (a) XRD data with the inset pictures of the $PbCu_3TeO_7$ single crystal, and (b) magnetic susceptibility as a function of $T$ along each direction in $PbCu_3TeO_7$ single crystals.

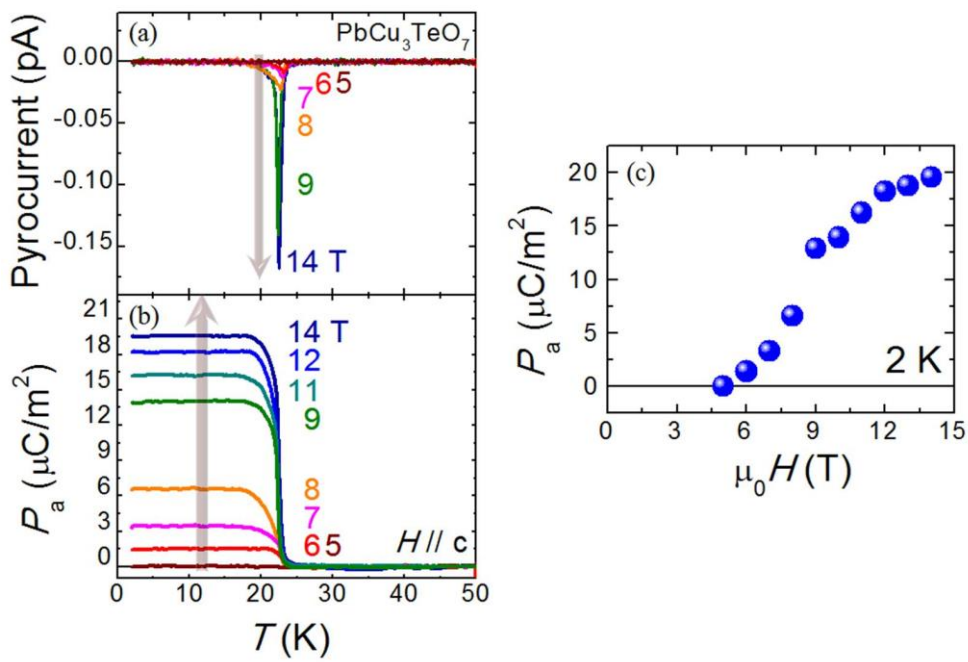


**Figure 4.5** Temperature dependent (a) pyroelectric current, (b) electric polarization for $P$//a and (c) the electric polarization at 2 K at each magnetic field in $PbCu_3TeO_7$ single crystals.

Note that no pyroelectric current was observed, for other directions of magnetic field ($H$) and electric polarization ($P$) up to 14 T. The electric polarization (Fig. 4.5(b)) for each $H$ was calculated by integrating the pyrocurrent with respect to time. The $P$ is almost same between 2 K and 17 K, and drops rapidly at ~22 K before it disappears at $T_{N2}$ = 24 K. Note that AFM ordering and $P$ arises at same temperature $T_{N2}$ for $H$//c. The figure 4.5(c) shows that $P$ at 2 K increases above 5 T, including the huge jump between 8 T and 9 T.

The temperature dependent dielectric constant ($\varepsilon$) also shows anomalies in the vicinity of $T_{N2}$ (Fig. 4.6(a),(b)). The small peak at 0 T becomes bigger upon increasing $H$. Another interesting observation is that additional broad peak was measured at 8 T, 9 T, and 10 T at temperatures 17.1 K, 18.1 K and 19 K respectively. The broad peak increases until 9 T and decreases until finally disappearing at 14 T. Meanwhile, the sharp peak becomes bigger monotonically up

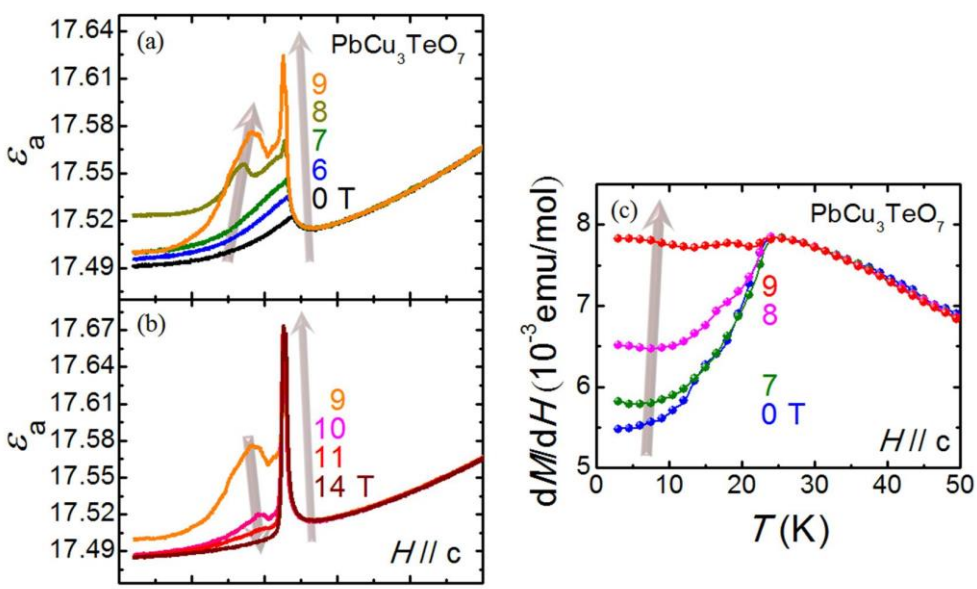


**Figure 4.6** Temperature dependence of (a),(b) dielectric constant $\varepsilon$ and (c) d$M$/d$H$ at selected magnetic fields in $PbCu_3TeO_7$ single crystals.

to 14 T. The $\varepsilon(T)$ for all of the $H$ converges at the peak position of 0 T data, at $T_{N2}$. Figure 4.6(c) shows the temperature dependent magnetization divided by magnetic field ($dM/dH$) at 1 T, 7 T, 8 T and 9 T along c direction. The magnetic moment orders to AFM phase below $T_{N2}$ at 1 T, and shows almost same trajectory up to 6 T. In contrast, the $\chi$ below starts to increase at 7 T before significantly enhancing at 8 T and 9 T. This suggests that the magnetic structure drastically changes in the vicinity of 8 T, which is consistent with the sudden increase of $P$ between 8 T and 9 T. The concomitant anomalies at $T_{N2}$ in $P$, $\varepsilon$, and $\chi$ strongly support that the magnetic structure below $T_{N2}$ is intimately related to the origin of induced $P$.

In order to investigate the $H$ induced $P$ more carefully, we measured the $H$ dependent ME current, magnetization ($M$) and $\varepsilon$ at 2 K under magnetic field up to 14 T (Fig. 4.7). For the ME current measurement, we poled the sample a 50 K and 9 T, and cooled down to 2 K, before short the electrodes and measure during decreasing the magnetic field down to -9 T. The ME current clearly shows a peak at ±8.2 T. By integrating the ME current, we obtained the $P(H)$ curve arises from ~6 T before suddenly increase to ~15 $\mu C/m^2$ at ~ 8.2 T, which is consistent with the $P$ from pyrocurrent measurement. For the other magnetic field direction, the polarization rises at sample field, but the magnitude of the $P$ is ~9 $\mu C/m^2$.

The dielectric constant along the a-direction also shows sharp peaks at ±8.2 T which strongly support the intrinsic ferroelectric property under $H$. Note that the anomalies in the ME current and dielectric constant did not appear when magnetic field was applied along other directions. In the $M$-$H$ data, along $a$- and $b$- directions (fig. 4.7(d)), the magnetization ($M$) linearly increase up to ~0.13 $\mu_B$ at 9 T.

On the other hand, there is a jump in the $M$-$H$ curve along c-direction. The

magnetic field derivative of $M$ (d$M$/d$H$) clearly shows the peaks at ± 8.2 T. This indicated that the polarization $P_a$ at |$H$//c| > 8.2 T originates from magnetic structure change under the magnetic field.

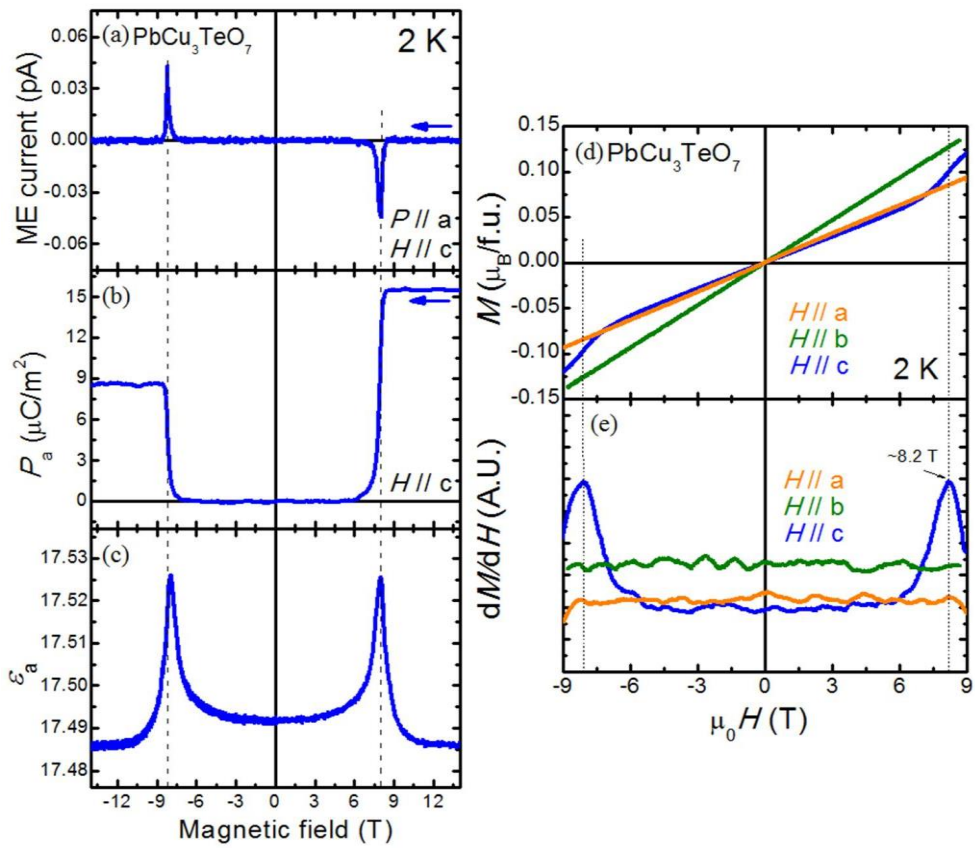


**Figure 4.7** Magnetic field dependence of (a) ME current, (b) electric polarization $P$, and (c) dielectric constant $\varepsilon$ along a-direction, and (d) magnetization and (e) d$M$/d$H$ along each direction in $PbCu_3TeO_7$ single crystals. All data was taken at 2 K.

The pyrocurrent and ME current for *P*//*a* were also measured under magnetic fields along each directions (Figure (4.8)). The pyrocurrent and ME current were measured under the fastest sweep speed of 20 K/min and 200 Oe/s respectively, in order to maximize the current signal. The pyrocurrent under *H*//*c* shows the largest signal. The pyrocurrent for *H*//*a* and *H*//*b* are only ~2.5 % of that of *H*//*c*. These small signals may not be intrinsic but come from misalignment of the sample below 2 degree. In addition, the ME currents show anomaly only for *H*//*c* at ~8.3 T and there is no signal for other *H* directions. According to the sweep direction of *H*, the ME current is reversed, which support the same *P*-*H* curve. These data confirms that the electric polarization along *a*-direction rises only for *H*//*c* up to 9 T.

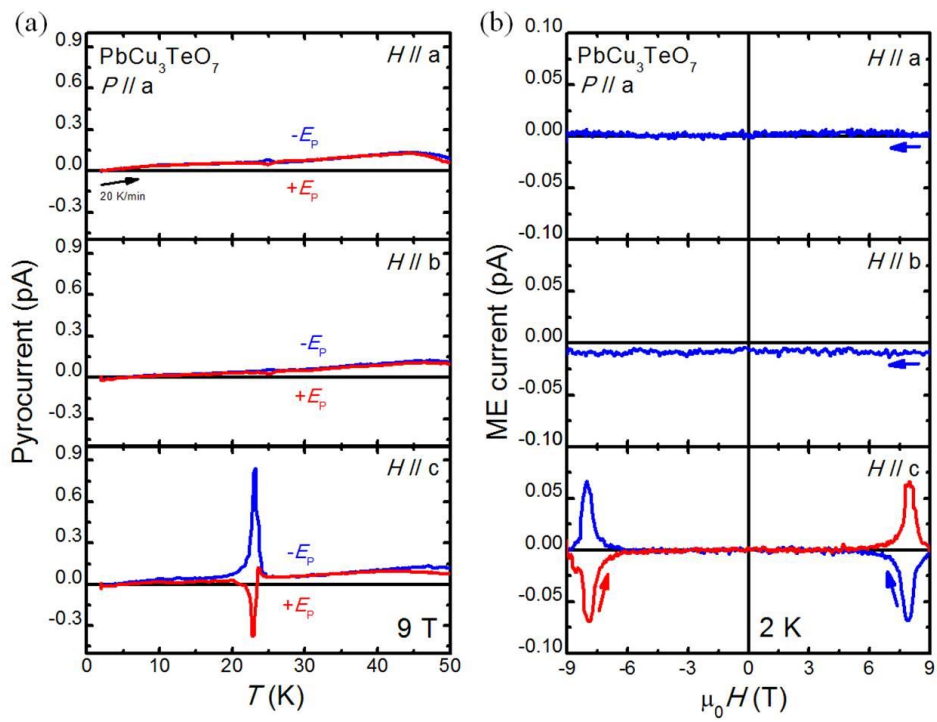


**Figure 4.8** (a) Pyrocurrent and (b) ME current for each directions of magnetic field and for *P*//a in $PbCu_3TeO_7$.

### 4.3.4. Magnetoelectric properties under high magnetic field in $PbCu_3TeO_7$ single crystals

For the further investigation of the magnetic field induced ferroelectricity, we measured the magnetoelectric properties at high magnetic field up to 60 T. In the ME current measurement at 2 K, a single peak was measured at ~8.2 T for *H*//*c* which is consistent with the low field results, meanwhile two peaks for *H*//*a*, one positive and another negative, are observed at ~16 T and ~38 T (Fig. 4.9 (a)). However, we could not observe any anomalies for *H*//*b* up to 60 T. The electric polarization *P*-*H* curves (Fig. 4.9 (b)) were obtained by integrating the ME current. For *H*//*c*, the *P* rises up to ~15 μC/m$^2$ at ~8.2 T and is maintained almost same up to 60 T. On the other hand, for *H*//*a*, the *P* increases up to ~14 μC/m$^2$ at ~16 T, and

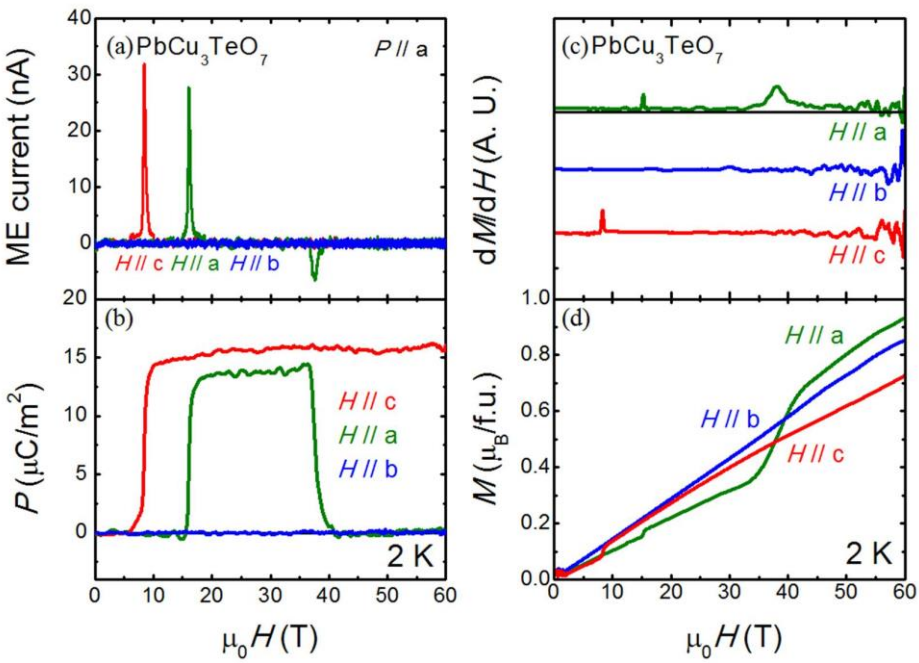


**Figure 4.9** Magnetic field dependence of (a) ME current, (b) electric polarization *P*, (c) d*M*/d*H*, and (d) magnetization *M* along each direction in $PbCu_3TeO_7$ single crystals. All data was taken up to 60 T at 2 K.

it decrease relatively broadly from 36 T before goes down to zero at 41 T, while there is no *P* observed for *H*//*b*.

The d*M*/d*H* curves (Fig 4.9(c)) were calculated from the raw data taken from the pick-up coil magnetometer, and shows peaks along the *a*- and *c*-direction. In the *M*(*H*) data at 2 K (Fig 4.9(d)), *M* increase linearly before the sharp step at 8.3 T and 15.4 T for *H*//*c* and *H*//*a* respectively. The linear extrapolation of *M*(*H*) above the step has the zero intercept at $H = 0$, suggesting the step as spin flop transition. An additional relatively broad step was observed at 38 T only for *H*//*a*. This is another spin flop transition because the linear extrapolation of *M*(*H*) curve at $H > \sim 42$ T passes the zero offset. In contrast, for *H*//*b*, *M* increases linearly up to 60 T without any anomaly. The most striking feature is that the fields of the magnetic transitions are close to that of anomalies in *P* along each direction. The value of *M* at 60 T is 0.93 $\mu_{B,}$ 0.85 $\mu_B$, and 0.72 $\mu_B$ per f.u. for *H*//*a*, *H*//*b*, and *H*//*c*, respectively which are still much smaller than expected saturation magnetization $M_s = 3\ \mu_B$/f.u. for three $Cu^{2+}$ ions with $S = 1/2$.

Figure 4.10 presents the $\varepsilon$ and magnetic field derivative of *P* (d*P*/d*H*) and *M* (d*M*/d*H*) at several temperatures. The peaks in the d*P*/d*H* and d*M*/d*H* represent the electric and magnetic phase transitions. The peak position at 16 T in d*P*/d*H* for *H*//*a* does not change upon warming up from 2 K, while the peak field at becomes lower as warming up to 20 K and 22 K, before both of the peak disappears at 25 K. The oscillations of d*P*/d*H* at higher temperature are not intrinsic effect, but rather from the vibration of sample in the pulsed field due to the high d*H*/dt rate. The d*M*/d*H* peaks follow the similar trend disappearing between 20 K and 30 K.

It is interesting observation that, even for *H*//*a*, the *P* and magnetic transitions do

not appear at 24 K < T < 36 K where the spin orders along *a*-axis. This strongly suggests that the field-induced polarization arises from the change of spins order by the spin flop transitions along both of *a*, and *c* directions. For *H*//*c* (Fig 4.10(c,d,e)), the peak fields in d*P*/d*H*, d*M*/d*H*, $\varepsilon$ becomes higher in higher temperature and eventually disappears at 25 K, which agrees with the temperature dependent measurements in Figure 4.4 and 4.5.

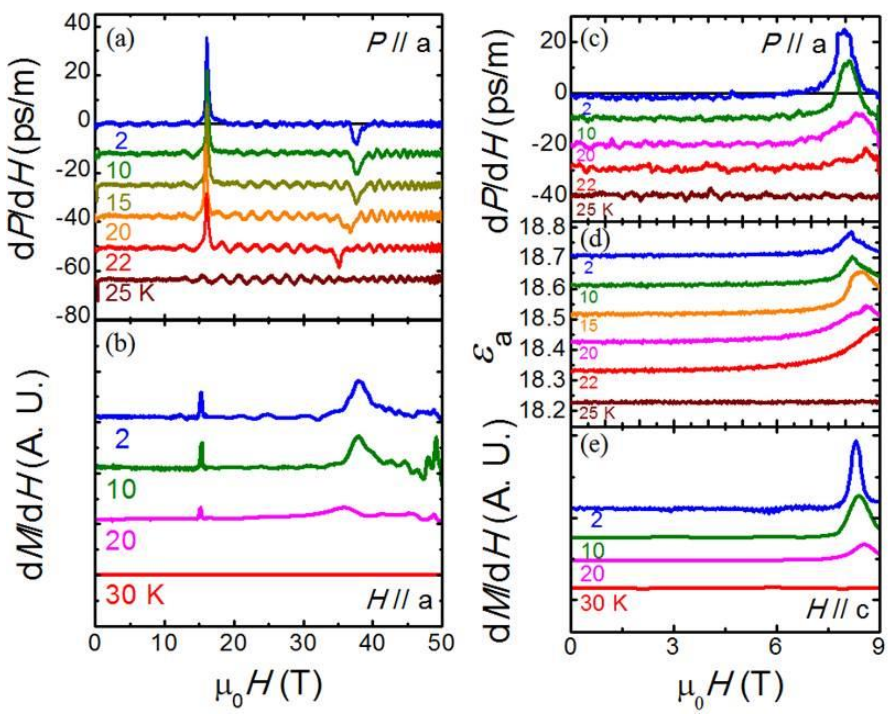


**Figure 4.10** Magnetic field dependence of (a),(c) Magnetoelectric coefficient (d*P*/d*H*), (d) dielectric constant ($\varepsilon$), and field derivative of magnetization (d*M*/d*H*) at selected temperatures for *H*//a and *H*//c in $PbCu_3TeO_7$ single crystals.

## 4.3 Discussion

### 4.3.1. Phase diagram of the $PbCu_3TeO_7$

Based on the data presented in Figs. 4.4-4.10, we plot the phase diagram of the $PbCu_3TeO_7$ for $H$//c and $H$//a in Fig. 4.11(a) and (b), respectively. The peak positions in d$P$/d$H$, d$M$/d$H$, $\varepsilon(H)$, $\varepsilon(T)$, $\chi(H)$, $\chi(T)$ and points in which $P(T)$ appears or disappears are drawn. The phase boundaries from each measurement well agree with each other, separating clearly the paramagnetic, paraelectric phase at high

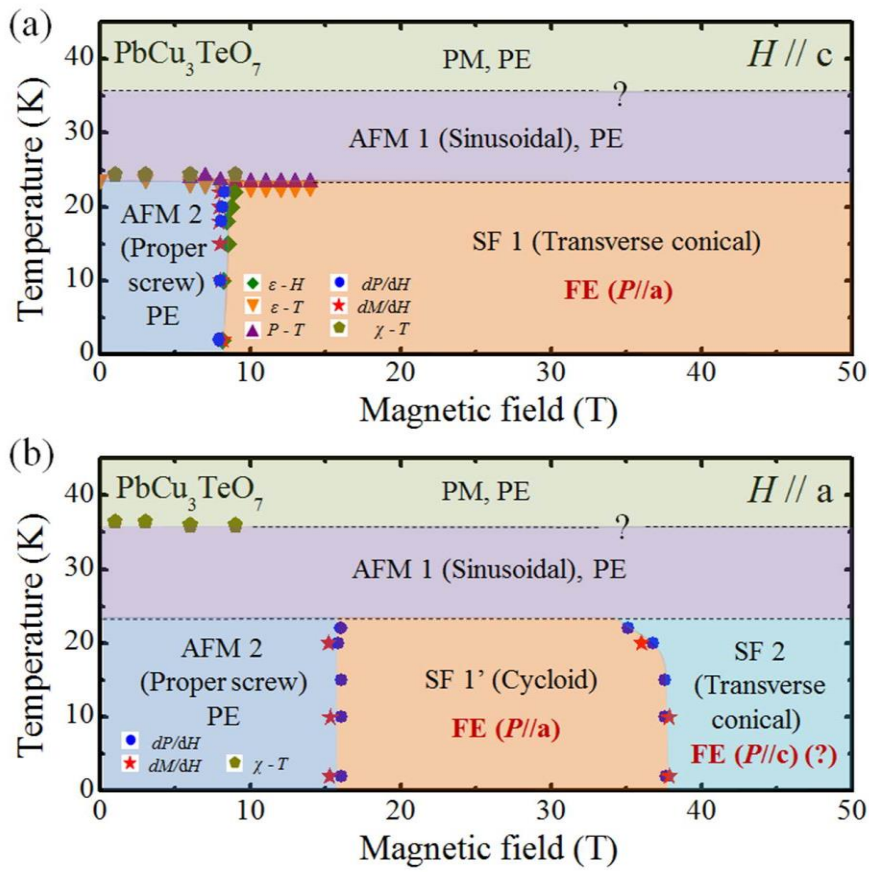


**Figure 4.11** Phase diagram of $PbCu_3TeO_7$ for $H$//c and $H$//a. The data points indicate anomalies in dielectric constant ($\varepsilon$), magnetization ($M$), and electric polarization ($P$).

temperatures from AFM 1, which is stabilized below $T_{N1}$ = 36 K, and AFM 2 phases, which is stabilized below $T_{N2}$ = 24 K. In particular, we found the evidence of finite electric polarization and ferroelectricity for *H//c* above 6 T, where a sharp spin-flop transition occurs. We named the ferroelectric region high magnetic field as SF 1 and FE. Moreover, for *H//a*, we found two spin-flop-like transitions inside the AFM 2 phase, naming the high field regions SF 1' and SF 2. In particular, in the region between the two spin-flop-like transitions, we observed the ferroelectric polarization, as summarized in Fig. 4.11(b).

### 4.3.2. Monte Carlo calculation on the $PbCu_3TeO_7$

In order to understand the nature of the magnetically ordered phases in $PbCu_3TeO_7$ we performed *ab initio* calculations of the exchange constants. First, the DFT calculations of exchange constants in $PbCu_3TeO_7$ were performed using the Vienna Ab initio Simulation Package (VASP) [33]. We have used the GGA+U approach with the on-site repulsion for Cu atoms by the Dudarev method [34]. The value $U_{eff} = U - J = 10$ eV was chosen similar to other DFT studies of Cu-containing magneloelectrics [35-36]. The plane-wave cutoff energy of 500 eV was used, whereas the Brillouin zone was integrated with the $4 \times 6 \times 4$ mesh determined by the Monkhorst–Pack scheme [37]. In the previous work [32] the most important exchange paths were studied identifying 8 ($J_1$ to $J_8$) intra- and 4 ($J_{i1}$ to $J_{i4}$) inter-kagome plane couplings. In the present work we calculate respective exchange constants, which are summarized in Table 1.

| | $J_1$ | $J_2$ | $J_3$ | $J_4$ | $J_5$ | $J_6$ |
|---|---|---|---|---|---|---|
| Cu-Cu distance, Å | 2.901 | 3.066 | 3.264 | 3.287 | 5.433 | 5.616 |
| $J$, meV | -2.4 | 0.57 | 5.1 | 2.1 | 2.0 | 1.1 |
| | $J_7$ | $J_8$ | $J_{i1}$ | $J_{i2}$ | $J_{i3}$ | $J_{i4}$ |
| Cu-Cu distance, Å | 6.353 | 6.696 | 5.918 | 6.117 | 6.278 | 5.279 |
| $J$, meV | 4.9 | 1.9 | 4.0 | 1.0 | -0.18 | -5.3 |

**Table 4.1** Exchange parameters of $PbCu_3TeO_7$ determined by DFT calculation.

The obtained exchange constants were then used as input for Monte Carlo (MC) simulations. The model Heisenberg Hamiltonian has the form

$$\mathcal{H} = \sum_{<ij>} J_{ij} \vec{S}_i \cdot \vec{S}_j + \sum_i \left( K_x S_{ix}^2 + K_y S_{iy}^2 + K_z S_{iz}^2 \right) - \sum_i \vec{H} \cdot \vec{S}_i \qquad (4.1),$$

where the spins $\vec{S}_i$ are classical vectors of unit length, $K_\alpha$ $(\alpha = x, y, z)$ are anisotropy constants. According to the succession of anomalies in the temperature dependent magnetization measurements one can conclude that $K_x < K_y < K_y$ and we find that the values give reasonable correspondence with the experiments.

Preliminary simulations of 20×20×20 unit cells (96000 magnetic ions) have identified that the appearing magnetic structure is modulated along the b direction with the wave vector close to $\vec{k} = \left(0, \frac{1}{3}, 0\right)$. Therefore subsequent studies were performed using the 4×150×4 simulation box.

In order to understand the magnetic structure and its coupling to the electric polarization we performed symmetry analysis. In the $\vec{k} = \left(0, \frac{1}{3}, 0\right)$ point of the

Brillouin zone the Pnma space group has four two-dimensional irreducible representations (IR), $\Delta_i$ ($i$ = 1,2,3,4).

The appearing magnetic structure has been classified as belonging to the $\Delta_2 \otimes V'$ exchange multiplet (here $V'$ is the pseudo-vector representation) [38]. This multiplet splits into the direct sum of IR's $\Delta_4$, $\Delta_1$, and $\Delta_3$, according to which the x, y, and z components of spins transform, respectively, and we denote by $(a_1, a_2)$, $(b_1, b_2)$, and $(c_1, c_2)$ the respective order parameters.

The appearance of modulated magnetic structure is in accordance with macroscopic symmetry since it allows Lifshitz invariants

$$a_1 \frac{a_2}{\partial y} - a_2 \frac{a_1}{\partial y}, \quad b_1 \frac{b_2}{\partial y} - b_2 \frac{b_1}{\partial y}, \quad c_1 \frac{c_2}{\partial y} - c_2 \frac{c_1}{\partial y} \qquad (4.2),$$

which result in modulation of magnetic order along *b*.

According to the zero magnetic field MC simulations upon lowering the temperature the first phase transition at $T_{N1}$ is related to the appearance of spatially modulated order parameters, $(a_1, a_2)$. Thus the spins are sinusoidally modulated along *a*-direction with propagation vector along *b*-direction between $T_{N1}$ and $T_{N2}$ (Fig 4.12(a)). Further cooling results in additional appearance of spatially modulated $(c_1, c_2)$ below $T_{N2}$. Therefore, the spins lie on *ac* plane with antiferromagnetic order. In addition, the spins rotate as they propagate to *b*-direction, showing the incommensurate proper screw order. The $\vec{k}$ vector of the spin structure is close but slightly different from $\vec{k} = (0, \frac{1}{3}, 0)$, thus the spin rotations have rough periodicity of 3 unit cell in *b*-direction but rotate slightly after the 3 unit cell (Fig 4.12(b)).

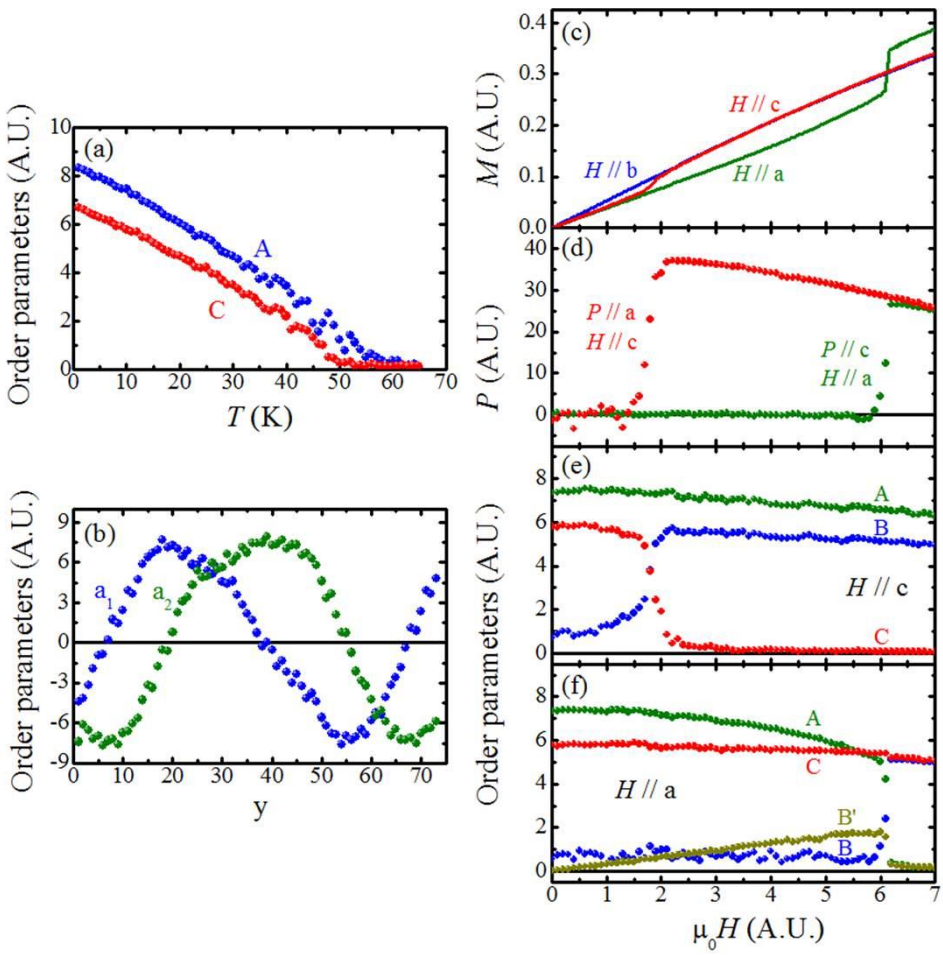


**Figure 4.12** The results of Monte Calro calculation on the $PbCu_3TeO_7$ including (a) the temperature dependence of order parameter amplitudes A and C at zero applied magnetic field, (b) spatial variation of the order parameter ($a_1$,$a_2$), as well as (c) the magnetization, (d) the polarization, and (e-f) the order parameters as function of magnetic field along various directions.

Upon application of magnetic field along *c*, in the SF 1 phase, the plane of spin rotations changes to *ab* as to be perpendicular to magnetic field by the spin flop transition (Fig 4.12(c)). In addition, there appears canted component of spin along c direction. In accordance with experiments the appearing transverse conical magnetic structure described by spatially modulated $(a_1, a_2)$ and $(b_1, b_2)$ possesses electric polarization along *a* due to the magnetoelectric interaction.

$$(a_1 b_1 + a_2 b_2) P_a \qquad (4.3).$$

Application of magnetic field along *a*-direction results in a more complex behavior. The SF 1' phase for 16 T < $H_a$ < 38 T is from our point of view induced by the interaction

$$(a_1 b_1 c_2 + a_1 b_2 c_1 + a_2 b_1 c_1 - a_2 b_2 c_2) M_a \qquad (4.4),$$

where $M_a$ is macroscopic magnetization along *a*. This interaction results in appearance of commensurate magnetic structure with non-zero order parameters $(a_1, a_2)$, $(b_1, b_2)$, and $(c_1, c_2)$, whereas the appearance of $P_a$ in this phase is described by the ME interaction Eq. (4.1) similarly to the phase $H_c$-induced ferroelectric phase.

The theoretical explanation on the microscopic origin and direction of *P* is predicted by the spin current model [30] (or inverse Dzyaloshinskii-Moriya interaction [28]) which is expressed by

$$\boldsymbol{P_{ij}} \propto \boldsymbol{e}_{ij} \times (\boldsymbol{S}_i \times \boldsymbol{S}_j) \qquad (4.5)$$

in which the $\boldsymbol{e}_{ij}$ is the propagation vecter between the $\boldsymbol{S}_i$ and $\boldsymbol{S}_j$.

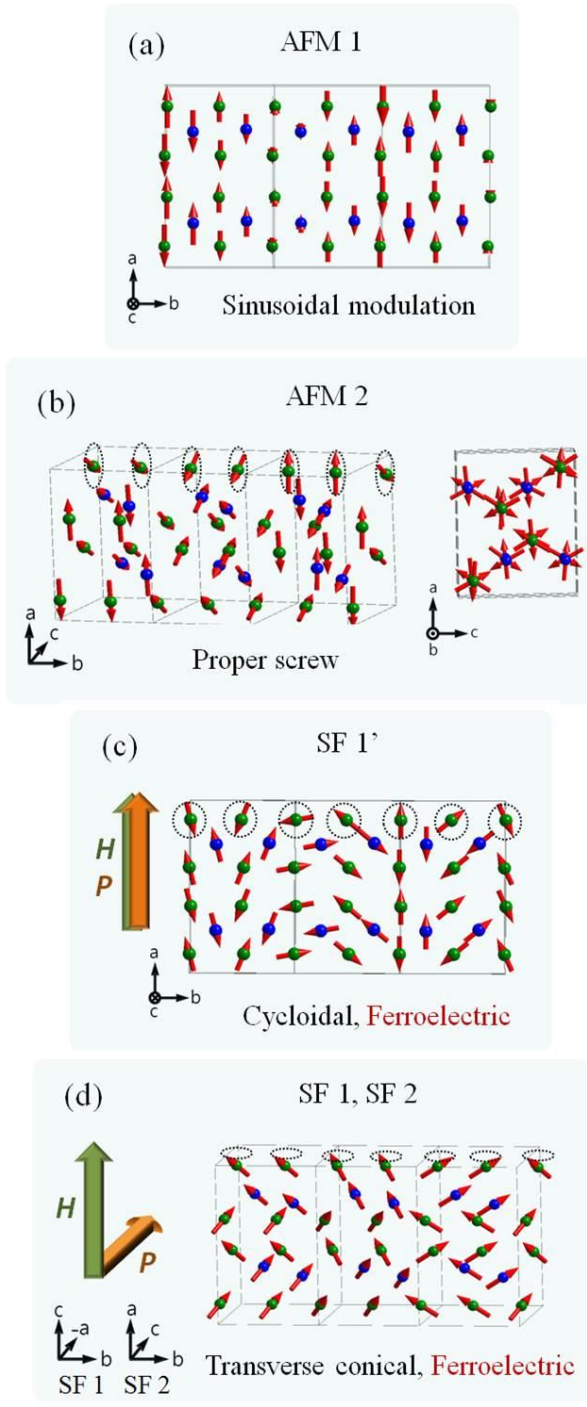


**Figure 4.13** Simplified schematic of the spin arrangements in each phase of (a) AFM 1, (b) AFM 2, (c) SF 1' and (d) SF 1, SF 2 phases.

In the SF 1' phase of $PbCu_3TeO_7$, the $\boldsymbol{e}_{ij}$ is along *b*-direction and the spin current $\boldsymbol{j}_s(=\boldsymbol{S}_i \times \boldsymbol{S}_j)$ is along *c*-direction. Thus, the spin current model well predicts the direction of $\boldsymbol{P}_{ij}$ $(=\boldsymbol{e}_{ij} \times \boldsymbol{j}_s)$ to be along *a*-axis. In addition, the polarization $\boldsymbol{P}_{ij}$ between each two spins have same direction in the cycloidal order, thus result in the macroscopic electric polarization *P*.

There are two other well-known microscopic mechanisms of magnetically induced ferroelectricity, exchange-striction and spin-dependent *p-d* hybridization, however, they do not seem to be more adjustable than spin current model for $PbCu_3TeO_7$. The exchange-striction requires specific lattice of straightly stacked A-B type form ($Ca_3CoMnO_6$ [39]) or zigzag form ($RMn_2O_5$ [40]) so that the spin sites on the lattice show collinear up-up-down-down sequence. But, in $PbCu_3TeO_7$, there is neither an evidence of up-up-down-down, nor collinear spin alignment below $T_{N2}$. The spin-dependent *p-d* hybridization via spin-orbit interaction is realized in the proper screw spin texture in the triangular lattice ($CuFeO_2$ [6-7]) or the noncentrosymmetric lattices ($Ba_2CoGe_2O_7$ [41]). From *p-d* hybridization in the proper screw system, the *P* is allowed to emerge along the direction parallel to the magnetic propagation vector $\boldsymbol{q}$, $P//\boldsymbol{q}$, whereas the spin current model allows $P\perp\boldsymbol{q}$. In $PbCu_3TeO_7$, the *P* is along the a-axis and the $\boldsymbol{q}$ should lie in the bc (intra layer) plane, supporting the spin current model of $P\perp\boldsymbol{q}$. Some special noncentro-symmetric lattices, for example the tilted $CoO_4$ tetrahedra in $Ba_2CoGe_2O_7$, also induce *P* by preventing cancellation of local dipole *p* from spin-orbit interaction. The centrosymmetric $PbCu_3TeO_7$ with orthorhombic space group Pnma at 300 K has still possibility to be distorted to noncentrosymmetric lattice below $T_{N2}$ to give rise to *P* with *p-d* hybridization, however, further detailed lattice and magnetic

structure should be investigated to probe this. Our data in this report supports more the spin current model.

Under *H*//*a* more than 38 T, the spin rotation plane flop to the *bc* plane. However, the spins does not lie only on the *bc* plane but also canted to the *a*-direction, which stands for the transverse conical (TC) spin order. In principle, the TC spin order should give rise to the electric polarization *P* along *c*-direction according to the spin current model. However, the *P*//c at $H > 38$ T was not confirmed by experiment. According to the Monte Carlo calculation, the *P* by the TC spin order cancel not by the symmetry, thus there remain no macroscopic *P*.

## 4.4 Summary

We have investigated the ME properties in a new staircase kagome magnet $PbCu_3TeO_7$ with $S=1/2$ $Cu^{2+}$ spin. The investigations of electric and magnetic properties revealed that $PbCu_3TeO_7$ shows ferroelectric property at >8.3 T and between 15 T and 38 T for *H*//c and *H*//a, respectively, whose on and off are concomitant with SF transitions. By means of Monte Carlo calculations we built a model of spin structures of each phase to understand the origin of the magnetic field induced *P*. In addition, the ME properties were summarized in the phase diagrams for each *H* direction, which divide the phases into PM, AFM 1, AFM 2, SF 1, SF 1', and SF 2. Detailed neutron scattering and X-ray diffraction will be helpful to understand further on the origin of ME coupling in this material.

## 4.5 References


[1] W. Eerenstein *et al.,* Nature **442**, 759 (2006).

[2] S. –W. Cheong *et al.,* Nature **6**, 13 (2007).

[3] D. Khomskii, Physics **2**, 20 (2009).

[4] T. Arima *et al.,* J. Phys. Soc. Jpn. **80,** 052001 (2011).

[5] Y. Tokura *et al., Rep. Prog. Phys.* **77,** 076501 (2014).

[6] T. Kimura *et al.,* Phys. Rev. B **73**, 220401 (2006).

[7] Y. Tanaka *et al.,* Phys. Rev. Lett. **109,** 127205 (2012).

[8] G. Lawes *et al.,* Phys. Rev. Lett. **93,** 247201 (2004).

[9] G. Lawes *et al.,* Phys. Rev. Lett. **95,** 087205 (2005).

[10] A. B. Harris *et al.,* Phys. Rev. B **73,** 184433 (2006).

[11] T. Lancaster *et al.,* Phys. Rev. B **75,** 064427 (2007).

[12] V. Ogloblichev *et al.,* Phys. Rev. B **81,** 144404 (2010).

[13] F. Fabrizi *et al.,* Phys, Rev, B **82,** 024434 (2010).

[14] J. Wang *et al.,* Phys, Rev, B **84,** 220407 (2011).

[15] M. Kenzalmann *et al.,* Phys. Rev. B **74,** 014429 (2006).

[16] I. Cabrera *et al.,* Phys. Rev. Lett. **103,** 087201 (2009).

[17] Y. Yamasaki *et al.,* Phys. Rev. Lett. **96,** 207204 (2006).

[18] K. Taniguchi *et al.,* Phys. Rev. Lett. **97,** 097203 (2006).

[19] L. Balents *et al.,* Nature **464,** 199 (2010).

[20] T. Kimura *et al.,* Nature Mater. **7,** 291 (2008).

[21] L. Zhao *et al.,* Adv. Mater. **24,** 2469 (2012).

[22] S. Park *et al.,* Phys. Rev. Lett. **98,** 057601 (2007).

[23] B. Koteswararao *et al.,* APL Mater. **4,** 036101 (2016).

[24] Y. Yasui *et al.,* J. Phys. Soc. Jpn. **77,** 023712 (2008).

[25] J. M. Law *et al.,* Phys. Rev. B **84,** 014426 (2011).

[26] S. Seki *et al.,* Phys. Rev. B **82,** 064424 (2010).

[27] B. Willenberg *et al.,* Phys. Rev. Lett. **108,** 117202 (2012).

[28] I. A. Sergienko *et al.,* Phys. Rev. B **73,** 094434 (2006).

[29] M. Mostovoy, Phys. Rev. Lett. **96,** 067601 (2006).

[30] H. Katsura *et al.,* Phys. Rev. Lett. **95,** 057205 (2005).

[31] B. Koteswararao *et al.,* J. Phys.: Condens. Mater. **25,** 336003 (2013).

[32] J. Dai *et al.,* Chin. Phys. Lett. **32,** 127503 (2015).

[33] G. Kresse *et al.,* Phys. Rev. B **54,** 11169 (1996).

[34] S. L. Dudarev *et al.,* Phys. Rev. B **57,** 1505-1509 (1998).

[35] X. Rocquefelte *et al.,* Nat. Commun. **4,** 2511 (2013).

[36] C. Lee *et al.,* Phys. Rev. B **86,** 060407 (2012).

[37] H. J. Monkhorst *et al.,* Phys. Rev. B **13,** 5188-5192 (1976).

[38] V. P. Sakhnenko *et al.,* Phys. Solid State **54,** 311-315 (2012).

[39] Y. J. Choi *et al.,* Phys. Rev. Lett. **100,** 047601 (2008).

[40] Y. Noda *et al.,* J. Phys.: Condens. Mater. **20,** 434206 (2008).

[41] J. W. Kim *et al.,* Nat. Comm. **5,** 4419 (2014).

# Chapter 5

# Linear magnetoelectric coupling in $Cu_3TeO_6$

## 5.1 Introduction

Investigation of the magnetoelectric (ME) coupling is one of effective ways to find the magnetic symmetry in magnetic insulators sensitively. In terms of symmetry analysis, as mentioned in Charter 1, the ME coupling is realized only when both time reversal and space inversion symmetries are broken, simultaneously. Some special spin textures and spin-orbit as well as spin-lattice coupling break the inversion symmetry, thus give rise to spin-driven ferroelectricity by three well known models; exchange striction, spin current (or inverse DM effect), and spin dependent *p-d* hybridization [1]. In addition, there are three types of symmetrically distinct multipole moments in which inversion symmetry are broken, thus generate linear ME coupling; the monopole moment, the toroidal moment, and the quadrupole moment. Each ME-active magnetic multipole allows 1, 3, and 5 kinds of linear ME tensors, respectively (Fig. 1.2).

In order to realize the linear magnetoelectric effect, we focused on the corundum related compounds of $A_3TeO_6$ (A = Ni, Mn, Co, and Cu). Interestingly, even though the chemical formula forms are same, $A_3TeO_6$ differ in structure and physical properties according to the ions at A site. $Ni_3TeO_6$ has trigonal structure with polar space group of R3. It shows collinear antiferromagnetic ordering along c-direction and pyroelectric properties [2,3]. $Co_3TeO_6$ crystalize in a monoclinic structure with

space group C2/c exhibiting magnetic-field-induced polarization [4]. $Mn_3TeO_6$ adopts a trigonal structure (space group $R\bar{3}$) and shows complex incommensurate magnetic structure [5] as well as multiferroic properties [6]. Meanwhile, $Cu_3TeO_6$ has cubic lattice structure and $S$ = 1/2 three-dimensional spin web showing antiferromagnetic ordering below $T_N$ = 62 K [7-11,13]. Neutron powder diffraction revealed that the dominant component of the magnetic moment is along one of the ±1±1±1 space diagonals of the cubic unit cell, however the magnetic structure is either collinear or canted. The multiferroic/magnetoelectric properties in $Cu_3TeO_6$ have not been investigated, possibly due to the nonpolar lattice structure.

In this chapter, we report the detailed investigation of linear magnetoelectric effect in $Cu_3TeO_6$. We observe that the electric polarization $P$ increases linearly under magnetic field $H$ up to 14 T for $P \perp H$, below $T_N$ = 62 K. We analyze the possible toroidal moment along diagonal directions and the magnetic structure without spatial inversion symmetry as the origin of linear magnetoelectric effect in $Cu_3TeO_6$.

## 5.2 Lattice structure

$Cu_3TeO_6$ crystalize in an Ia-3 space group in cubic structure with a = 9.537 Å. As shown in the Figure 5.1 (a), the unit cell consists of 8 regular $TeO_6$ octahedra. and 24 Cu ions. Each $TeO_6$ octahedron is surrounded by the six copper ions which form vertices of an almost planar hexagon with side length of 3.18 Å. Each hexagon, whose edges are shared with other hexagons, is perpendicular to the diagonal directions of the cubic unit cell, thus there are four different directions of the hexagons, [111], [11-1], [1-11], and [-111].

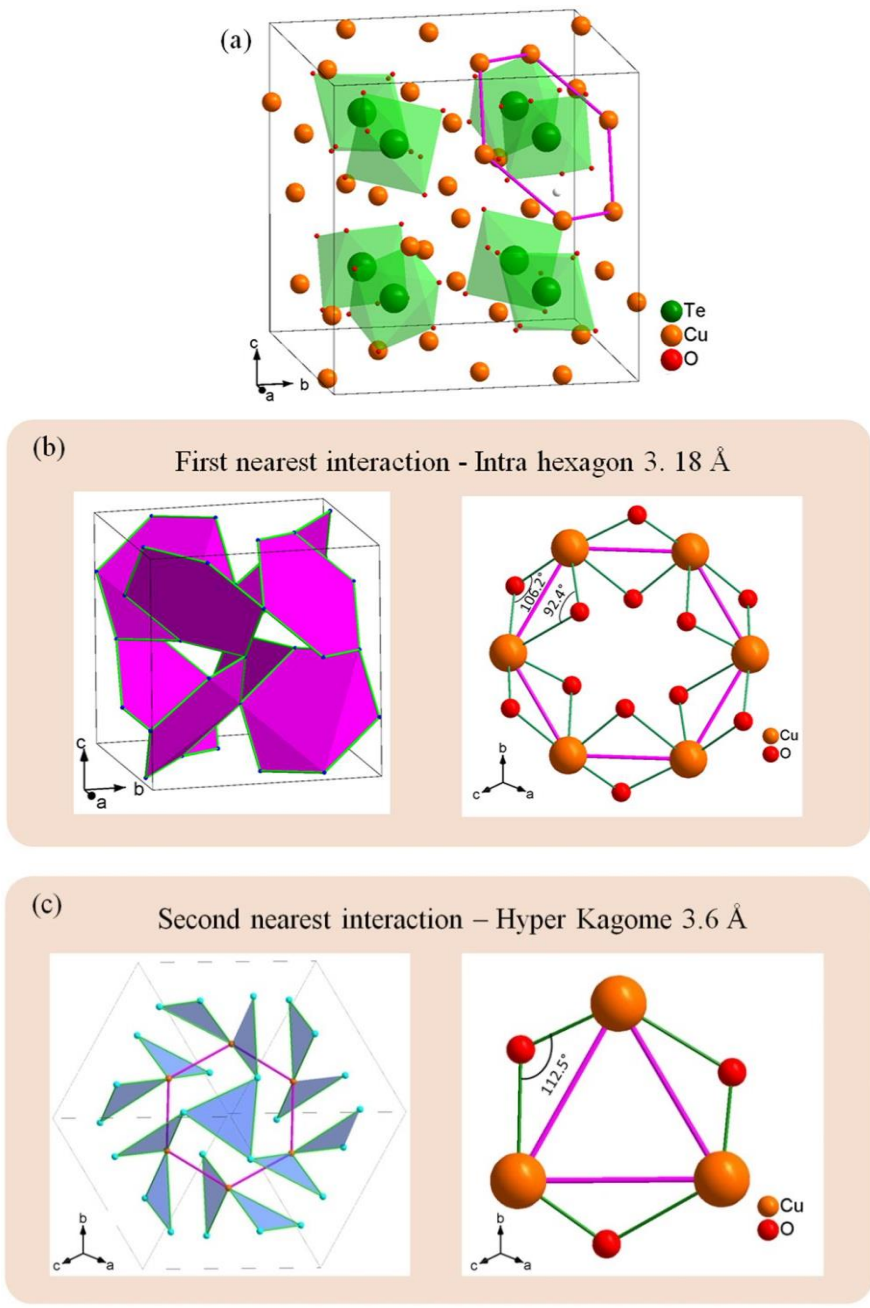


**Figure 5.1** (a) The crystal structure of $Cu_3TeO_6$ including six $TeO_6$ octahedra which are surrounded by Cu hexagon. (b) First and (c) second nearest interchange interactions, with the interaction path and bonding angles of Cu-O-Cu

The first nearest neighbor interaction is between the magnetic $Cu^{2+}$ copper ions in the hexagon (Fig 5.2(b)), whose superexchange path is connected by the Cu-O-Cu ions with angles of 92.4° and 106.2°. Each copper ion also has second nearest neighbor interaction at the distance of 3.6 Å connected by corner shared $CuO_6$ octahedron with a Cu-O-Cu angle of 112.5° (Fig 5.2(c)). The second nearest neighbor copper ions are connected by the hyper kagome network in which the triangular lattices are connected in 3 dimensions by sharing the edge.

## 5.3 Experimental method and results

### 5.3.1. Sample preparation

Single crystals of $Cu_3TeO_6$ were grown using flux method. First, $Cu_3TeO_6$ polycrystalline sample was prepared by solid-state reaction method using the starting materials of CuO and $TeO_2$. They were ground with a molar ratio of 3:1, and calcined at 600 ℃ for 12 hours twice before sintered at 850 ℃ for 24 hours. In order to grow single crystals, the polycrystalline of $Cu_3TeO_6$ and $PbO/TeO_2$ flux (molar ratio 1:1) were mixed with mass ratio of 1:2. The mixture was heated at 950 ℃ for 12 h and then cooled to 700 ℃ at a rate of 1.25 ℃/h. The single crystals were extracted by mechanically hitting the flux with single crystals. We obtained the cubic shaped single crystals of ~1 mm. For the electric measurements, we shaped the single crystal into the thin plate form along each direction for the measurements. The electrodes on the both sides of the plate were made with silver epoxy.

### 5.3.2. Lattice structure characterization of $Cu_3TeO_6$ single crystals

The lattice structure of the grown $Cu_3TeO_6$ single crystals was characterized by the XRD and Laue data. The figure 5.2(a) shows the XRD data of the $Cu_3TeO_6$ single crystal along the [100] direction. This data support that the $Cu_3TeO_6$ single crystal is grown without chemical impurity. Since the $Cu_3TeO_6$ has cubic structure, the crystals have clear rectangular shape with size of ~ 1 mm, as seen in the inlet of the figure 5.2(a). The Laue diffraction data, taken with a Laue diffractometer of Rigaku, in the figure 5.2(b) also confirms the crystallographic structure and its axis of the $Cu_3TeO_6$ by showing the measured data (black dots) well agrees with the theoretical data (red dots).

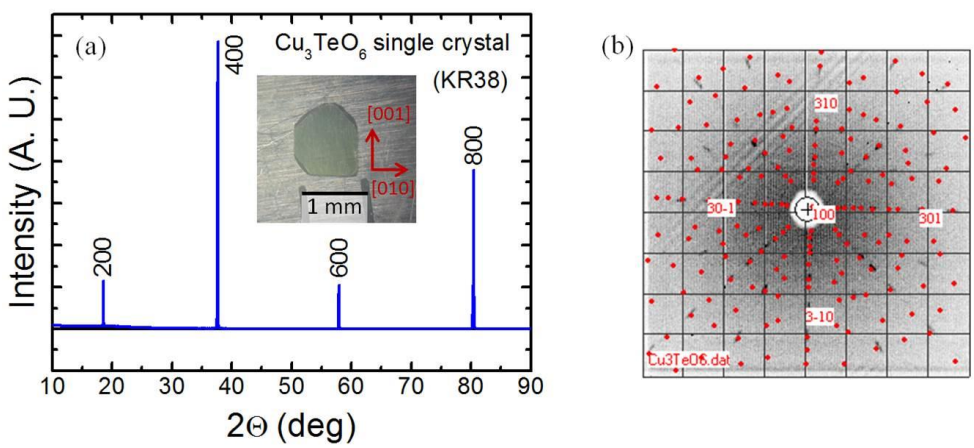


**Figure 5.2** (a) XRD data with the inset picture and (b) Laue diffraction data taken along the [100] crystallographic direction in the $Cu_3TeO_6$ single crystals.

### 5.3.2. Magnetic properties in $Cu_3TeO_6$ single crystals

Figure 5.3(a) displays the magnetic susceptibility ($\chi$) data along each direction which shows a kink at $T_N$ = 62 K, indicating long range antiferromagnetic ordering below $T_N$. The $\chi$ below $T_N$ varies slightly with the crystallographic directions. The lowest $\chi$ for [111] below $T_N$ suggests the [111] is easy axis, however, the magnetic anisotropy is quite week. The Curie-Weiss fitting from the inverse $\chi$ shows the Curie-Weiss constant of $\theta_{CW}$ = 160 K which is higher than the $T_N$. The value of $f = \theta_{CW}/T_N$ (=2.58 in our result) implies how much the magnetic interactions are frustrated. The $f$ of $Cu_3TeO_6$ in other reports 3.55 [12], 2.43 [13], and 2.23 [14] combined with our result indicate moderately frustrated interaction in $Cu_3TeO_6$. In addition, it is further evident that the $\chi$ starts to deviate from Curie-Weiss law

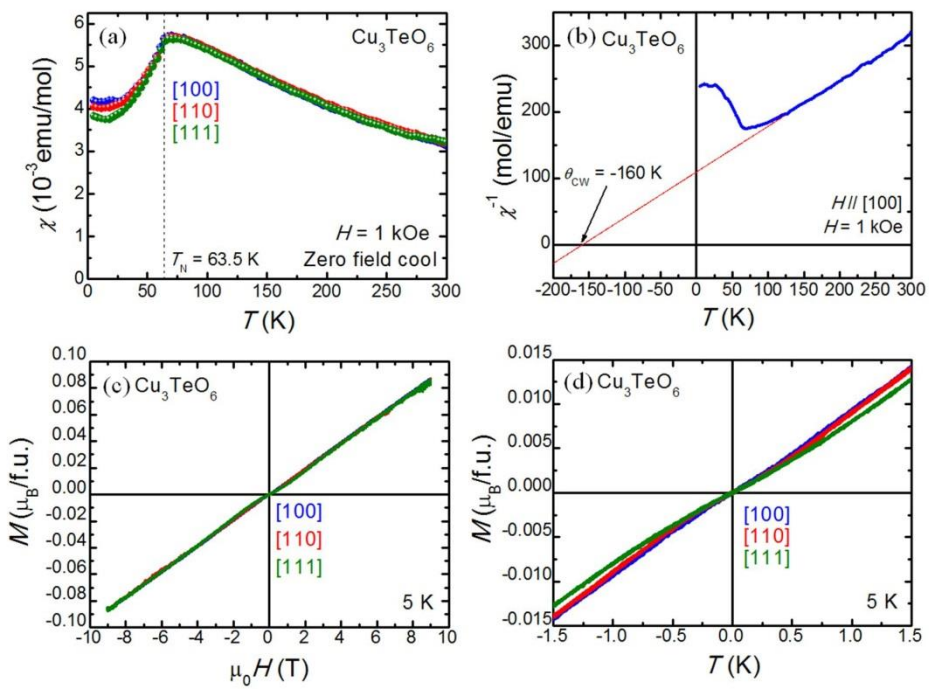


**Figure 5.3** (a) Magnetic susceptibility and (b) inverse susceptibility as a function of temperature and (c,d) magnetic field dependence of magnetization with two field ranges along each direction in the $Cu_3TeO_6$ single crystals .

below 126 K, possibly indicating the onset of a short-range spin order.

In the *M*-*H* data at 5 K, along each direction (fig. 5.3(c)), the magnetization (*M*) almost linearly increase up to ~0.086 $\mu_B$/f.u at 9 T. This is still much smaller than the expected saturation magnetization of $M_s$ = 3 $\mu_B$/f.u.. As we carefully zoom up the *M*-*H* data at 5 K, the *M*-*H* curve along [111] direction shows slight curve between -1.5 T and 1.5 T, whereas it is linear for [100] and [110].

### 5.3.2. Magnetoelectric properties in $Cu_3TeO_6$ single crystals

In order to investigate the magnetoelectric effect in $Cu_3TeO_6$, we measured pyroelectric current for *P* // [110] at several magnetic fields along the *H* // [1-10] direction. As explained in Chapter 2, we poled the sample with electric field at each magnetic field and cooled down to 2 K before electrically shorting and measure the current during warming up with rate of 10 K/min. To confirm whether the signal is intrinsic or not, we measured with both directions of poling. The data up to 9 T was obtained in 9 T PPMS$^{TM}$ and above 9 T data were taken in the 14 T magnet with same piece of sample. At zero field, there is no pyrocurrent visible with noise level of ~3 fA, however, there is a clear peak at ~62 K and a deviation between plus poling (+$E_P$) and minus poling (-$E_P$) from ~20 K. The deviation between the +$E_P$ and -$E_P$ systematically increase under higher magnetic field. In addition, it is noteworthy that the poling dependent pyroelectric current does not change upon changing the sign of *H*. In all of the data, there are background signals which are independent of the poling direction. This background is usually determined by how clean is the electrical ground of the cryostat. Indeed, the data in Fig 5.4 shows that the background in 14 T magnet, in which clean ground is connected, is much

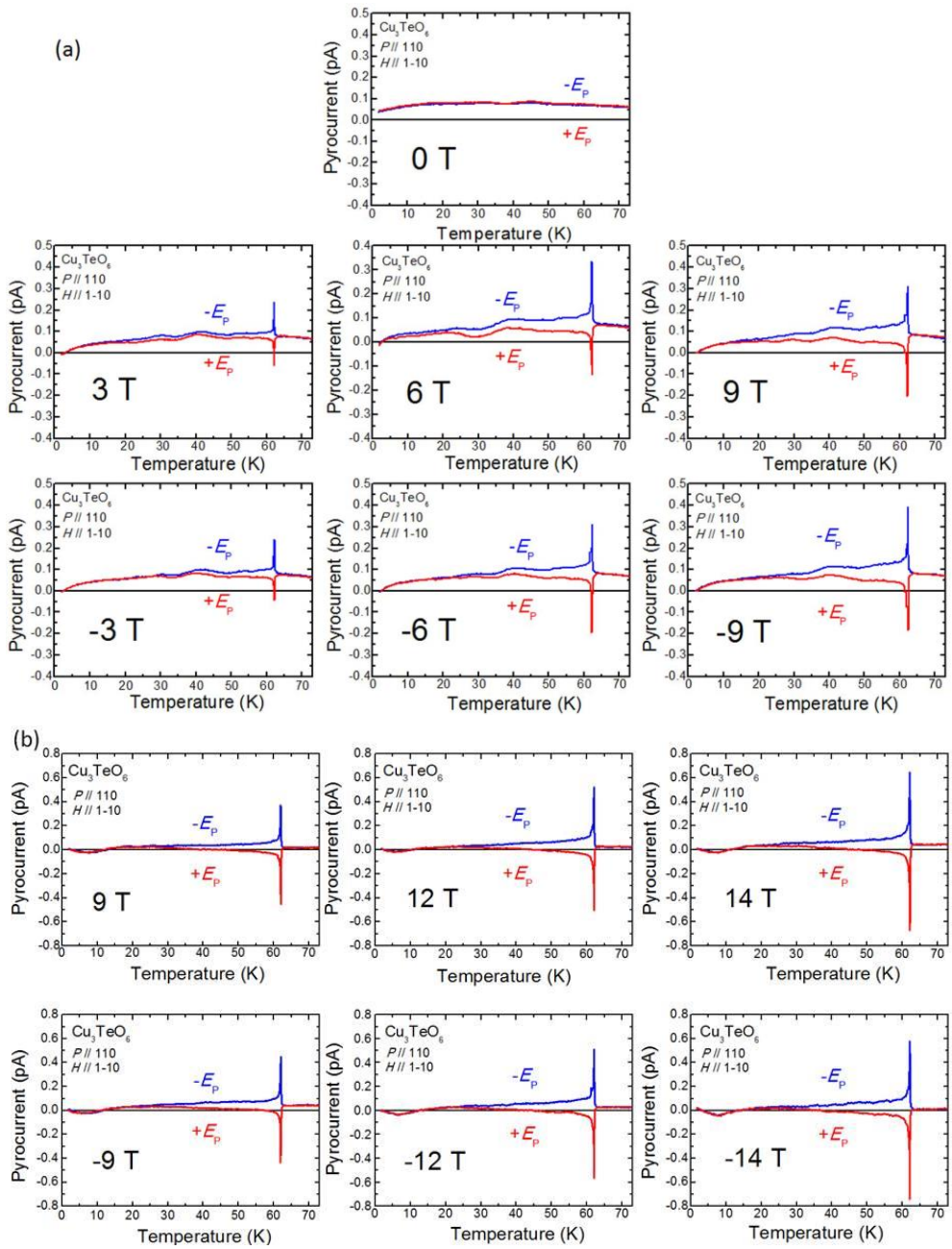


**Figure 5.4** Pyroelectric current data at several magnetic field for *P* // [110] and *H* // [1-10] taken in (a) 9 T PPMS$^{TM}$ and (b) 14 T magnet.

smaller than that of PPMS$^{TM}$ with dirty ground. For the quantitative analysis of electric polarization, we took average of the $+E_P$ and $-E_P$ data which is shown in Figure 5.5(a). By taking the average data, we can remove the background and obtain only the intrinsic pyrocurrent.

Upon increasing the temperature, the pyrocurrent linearly increases from ~20 K before a peak at 62 K, and they become larger and sharper at higher field up to 14 T. The electric polarization *P* (Fig. 5.5(b)) for each *H* which is obtained by integrating the pyrocurrent by time shows that the *P* is almost same below ~20 K and decrease quadratically as the temperature increases before it drastically decreases to zero at ~ 62 K.

The *P* at 2 K under various *H* (Fig. 5.5(c)) displays that the *P* increases linearly under the *H*. showing 20 μC/m$^2$ at 14 T. It is again noteworthy that the sign of *P* is not reversed upon changing the direction of *H*.

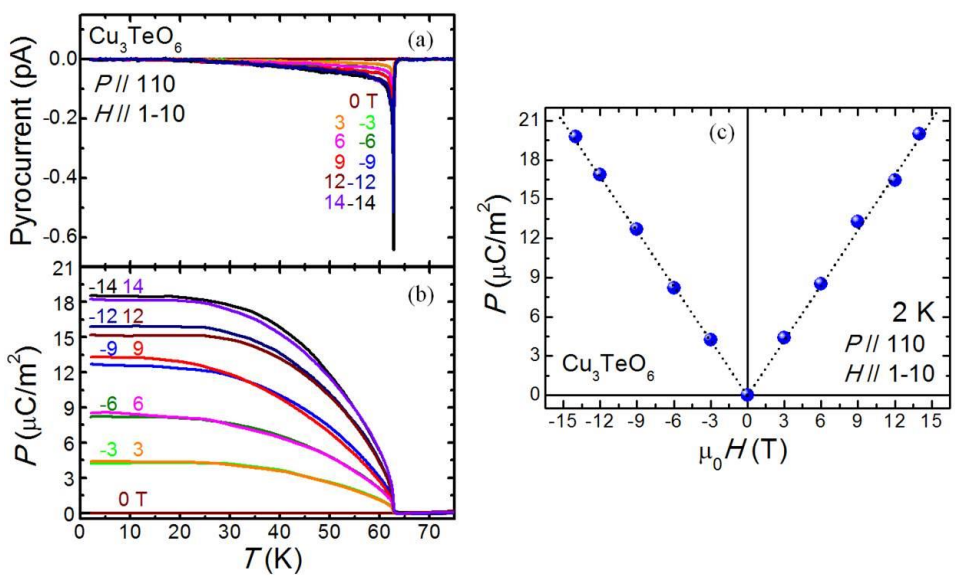


**Figure 5.5** Temperature dependent (a) pyroelectric current, (b) electric polarization for *P*//a and (c) the electric polarization at 2 K at each magnetic field in $Cu_3TeO_7$ single crystals for *P* // [110], *H* // [1-10].

In order to further investigate the magnetoelectric properties in $Cu_3TeO_6$, we measured pyrocurrent for different directions of *P* and *H* (Fig 5.5). The *P*(T) curves integrated from the pyrocurrent shows same line shapes for different directions, however, the *P* perpendicular to *H* is much larger than *P* parallel to the *H*; *P* at 2 K and 9 T for (*P*//110, *H*//1-10), (*P*//110, *H*//110), (*P*//100, *H*//010), and (*P*//100, *H*//100) is 13.3 μC/m$^2$, 1.4 μC/m$^2$, 7.4 μC/m$^2$, and 0.8 μC/m$^2$, respectively. These results suggest that the *P* perpendicular to *H* is intrinsic and the *P* parallel to *H* may come from the misalignment of the sample for measurement. The measurements along all the directions show same linear magnetoelectric effect.

We also measured the pyrocurrent rotating *H* direction on the $Cu_3TeO_6$ single crystal using a rotation probe. We repeated the poling and measurement procedure after rotating 30 degrees at each step under the continuous *H* of 9 T. We first measured the pyrocurrent along [100] and rotate the *H* from [100] to [010] direction (Fig 5.7(a) and also measured along [110] and rotate the *H* from [110] to [1-10]. The shape is not a perfect sinusoidal form, but it is observable that the *P* shows minimum value for *P*//*H* and maximum value for ~*P*⊥*H*. In addition, for more than 180 degree, the *P* does not go negative but increase again, exhibiting roughly $P \sim |sin\theta|$. This result agrees with the *P*-*H* data in the Fig 5.5 (c). When we next measured the pyrocurrent along [110] and rotate the *H* from [110] to [1-10] direction, the directions of *H* for maximum and minimum *P* shows same tendency as that of *P*//[100]. Unfortunately, the rotation data is not perfect because the rotator in the rotation probe is not firmly fixed, thus it can move during the measurement and the background of current in this probe is too high. At least we can roughly monitor the *H* direction dependence of *P*.

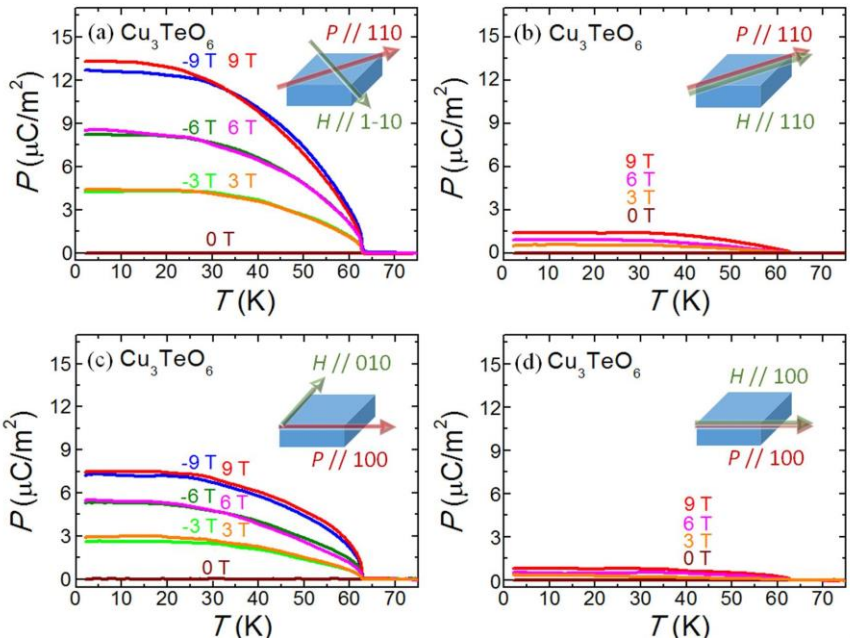


**Figure 5.6** Temperature dependence of electric polarization *P* at selected magnetic fields *H* in $Cu_3TeO_6$ single crystals for various directions of *P* and *H*.

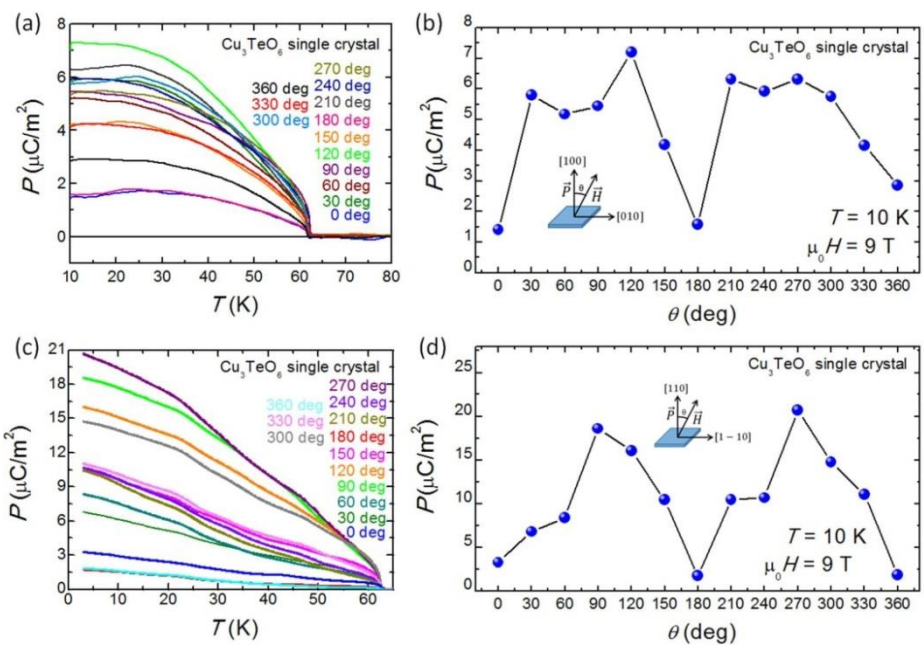


**Figure 5.7** Temperature dependence of electric polarization *P* along (a) [100] and (b) [110] at selected *H* directions, and (b,d) *H* angle dependence of *P* at 10 K and 9 T in $Cu_3TeO_6$ single crystal.

Figure 5.8 shows the dielectric constant $\varepsilon$ for $E$ // [110] at several magnetic fields along the $H$ // [1-10] direction. There is a small kink of $\varepsilon$ at 62 K without $H$. When $H$ of 3 T is applied, there is a jump of $\varepsilon$ at 62 K, and the jump increases largely upon increasing the magnetic field. It is noteworthy that the $\varepsilon$ at 2 K is increased tremendously from 13.35 at 0 T to 29.8 at 14 T. in addition the dielectric loss (tan δ) also largely change under the $H$. The huge magneto-dielectric effect, support that the intrinsic nature of the magnetoelectric effect.

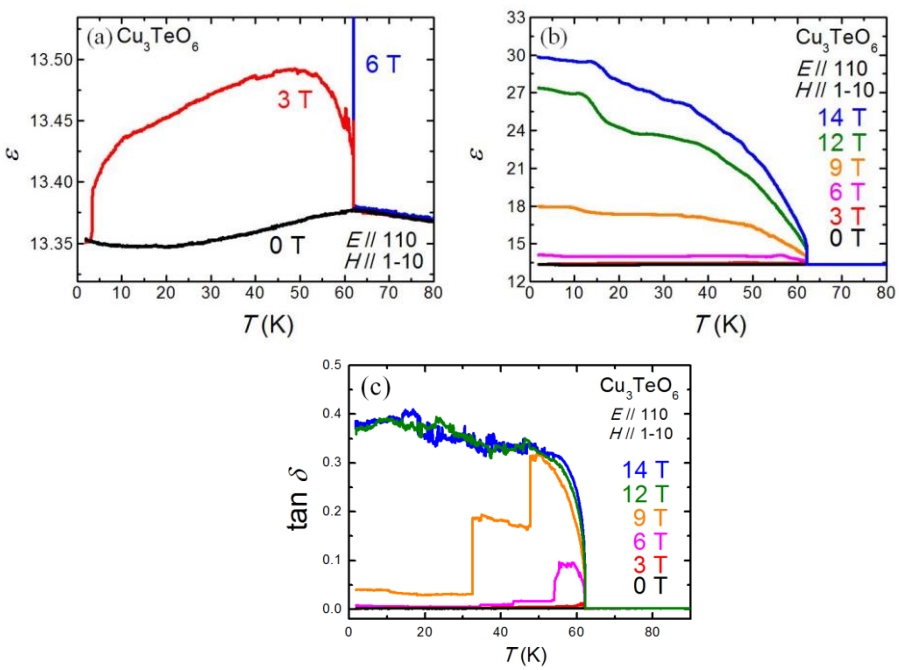


**Figure 5.8** Temperature dependence of dielectric constant $\varepsilon$ (a,b) and dielectric loss (c) at selected magnetic fields $H$ in $Cu_3TeO_6$ single crystals

## 5.4 Discussion

The results in the Figure 5.5,6 claims that linear ME tensor in $Cu_3TeO_6$ has dominant off-diagonal components. In this section, we analyze the linear ME effect of $Cu_3TeO_6$ in the view of off-diagonal ME tensor using the several methods.

### 5.4.1. Analysis of the ME effect based on the magnetic point group

The magnetic point group is closely related to the crystallographic (space) point group since the magnetic spins are put on the atom positions on the lattice. $Cu_3TeO_6$ has space group of $Ia\bar{3}$ and space point group of $m\bar{3}$. The magnetic point group adds the freedom of the time reversal symmetry, thus allowing the $m\bar{3}$, $m'\bar{3}$, $m\bar{3}'$, and $m'\bar{3}'$.

We can obtain the possible ME tensor from the symmetry operation of the magnetic point group. The transformation of the ME tensor $\overleftrightarrow{Q}$ by the symmetry operation A is written as

$$\overleftrightarrow{Q}' = A\overleftrightarrow{Q}A^T, or\ A\overleftrightarrow{Q}A^T \qquad (5.1).$$

According to the Neumann's principle [15], the ME tensors before and after the transformation should be same, $\overleftrightarrow{Q}' = \overleftrightarrow{Q}$. The figure 5.9 summarize the symmetry operation and possible ME tensors. We take the symmetry operation for each components of $m$ and $\bar{3}$,

$$m = \begin{vmatrix} -1 & 0 & 0 \\ 0 & 1 & 0 \\ 0 & 0 & 1 \end{vmatrix}, m' = \begin{vmatrix} 1 & 0 & 0 \\ 0 & -1 & 0 \\ 0 & 0 & -1 \end{vmatrix}, \bar{3} = \begin{vmatrix} 0 & 0 & -1 \\ -1 & 0 & 0 \\ 0 & -1 & 0 \end{vmatrix}, \bar{3}' = \begin{vmatrix} 0 & 0 & 1 \\ 1 & 0 & 0 \\ 0 & 1 & 0 \end{vmatrix}$$

and only the tensors which satisfy $\overleftrightarrow{Q}' = \overleftrightarrow{Q}$ for both operation is ME tensor. For the magnetic point groups, $m\bar{3}$, $m'\bar{3}$, and $m\bar{3}'$, no ME tensor is allowed. Meanwhile, the only $m'\bar{3}'$ allows the nonzero ME tensor with only diagonal components [16]. This is against to the results of the measurements which claims the off-diagonal ME tensor. Therefore, linear ME effect in $Cu_3TeO_6$ cannot be simply explained by the possible magnetic point group.

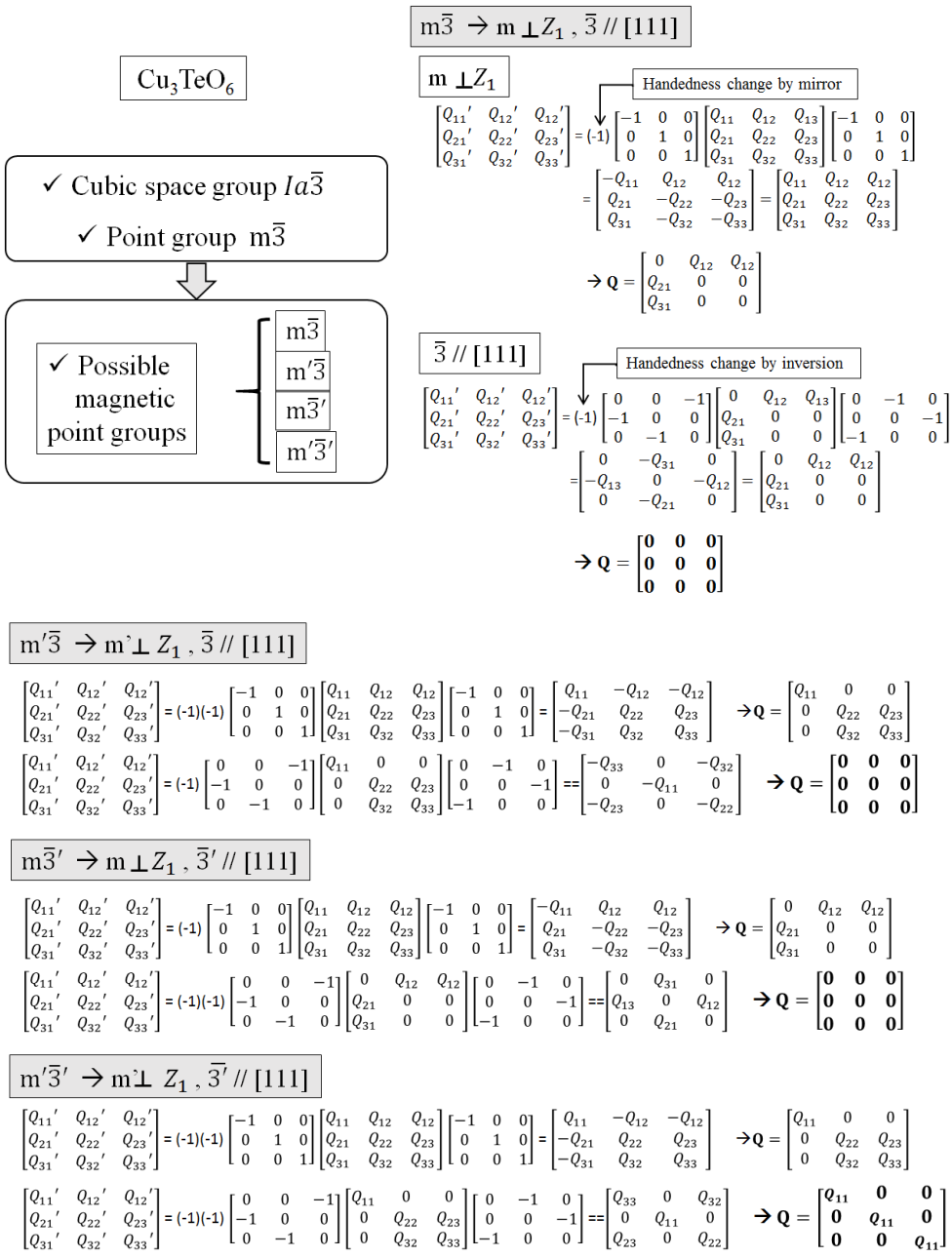


**Figure 5.9** Analysis of the linear magnetoelectric effect in $Cu_3TeO_6$ based on the point group.

### 5.4.2. Analysis of the ME effect based on the toroidal magnetic moment

Among the magnetic multipoles, the monopole, quadrupole and toroidal moment break the space inversion symmetry, thus allowing the linear ME effects.

Among them, toroidal moment is a special spin texture which is usually expressed by spins connected in doughnut shape. The toroidal moment $t$ is defined as

$$t \propto \sum_i r_i \times S_i \qquad (5.2)$$

where $r_i$ represents the locations of $S_i$.

It is sometimes not mentioned in textbook since no magnetic field is generated by it, however, it allows antisymmetric linear ME coupling in the magnetic insulators [17]; the electric polarization *P* is induced by magnetic field *H* according to

$$P = -t \times H \qquad (5.3).$$

As an example, the antisymmetric linear ME effect with $\alpha_{ij} = -\alpha_{ji}$ have been observed in $Ga_{2-x}Fe_xO_3$ [18]. $Ga_{2-x}Fe_xO_3$ has to spin sites of Fe1 and Fe2 which are stacked along b direction have opposite spin along c-direction. Since the sites of Fe1 and Fe2 are shifted from the centrosymmetric positions, the toroidal moment in each site is not canceled out. It is noteworthy that the toroidal moment can be nonzero without doughnut-like spin texture, if $t \propto \sum_i r_i \times S_i$ is not zero, as shown in $Ga_{2-x}Fe_xO_3$. Several compounds showing the linear ME effects from the toroidal moment have been reported including $Ni_xMn_{1-x}TiO_3$ [18], $Ga_{2-x}Fe_xO_3$ [18], $Cr_2O_3$(at high *H*) [19], $Co_3B_7O_{13}Br$ [20], and $LiNiPO_4$ [21].

While a toroidal moment always gives rise to an off-diagonal magnetoelectric response, such a response is not necessarily indicative of a toroidal moment. For example, conical spiral ordering in hexaferrite also give rise to a linear ME effect with antisymmetric contributions [22,23].

The $Cu_3TeO_6$ shows linear ME effect and the *P* perpendicular to *H* is much larger than that parallel to *H*, and this phenomena coincide with the ME effect from the toroidal moment. Therefore, we analyzed the linear ME effect assuming the spin structure in $Cu_3TeO_6$ allow the toroidal moment. The 8 hexagons which made of Cu ions are normal to the [1±1±1] diagonal directions. If the spins are slightly canted and the canted spins from the diagonal give rise to the toroidal moment, the toroidal moments are along the four directions [111], [-111], [1-11], and [11-1]. We can calculate the *P* direction under *H* for each four toroidal moments, which give rise to *P* along [110] when *H* is along [-110], and this is consistent with the

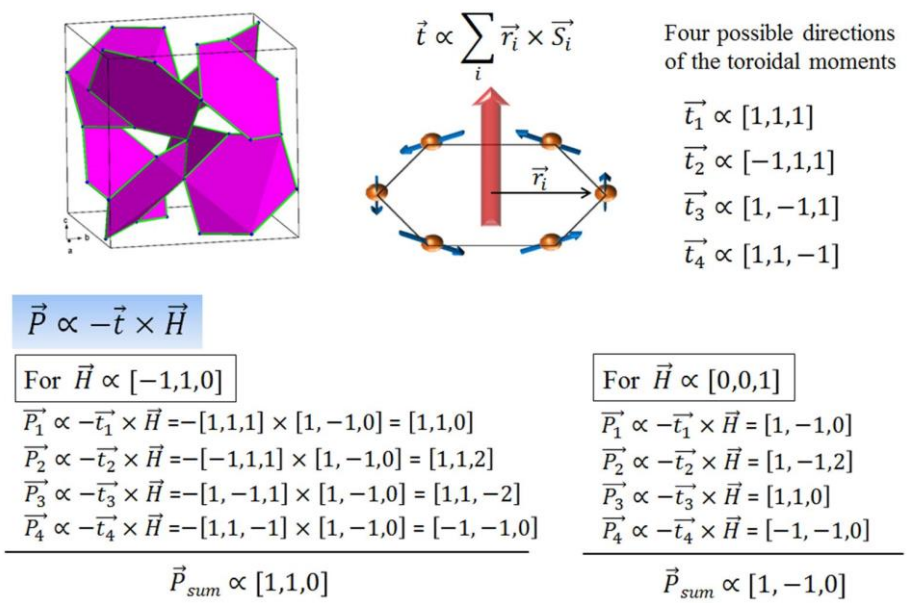


**Figure 5.10** Linear ME effect analysis in $Cu_3TeO_6$ based on the toroidal

experimental data in Figure 5.6 (a). This result is one clue which shows the existence of the toroidal moment as a source of linear ME effect. However, in or der to confirm the toroidal moment, further experiments through the neutron scattering is necessary.

### 5.4.3. Analysis of the ME effect based on the symmetry of magnetic structure

According to the neutron power scattering result [13], the spins most probably align collinearly with antiferromagnetic ordering along the diagonal [1±1±1], or slightly canted from the diagonal directions. Let us assuming the spins are collinear. In a single Cu hexagon, the spatial inversion symmetry ($\bar{1}$) is broken with the

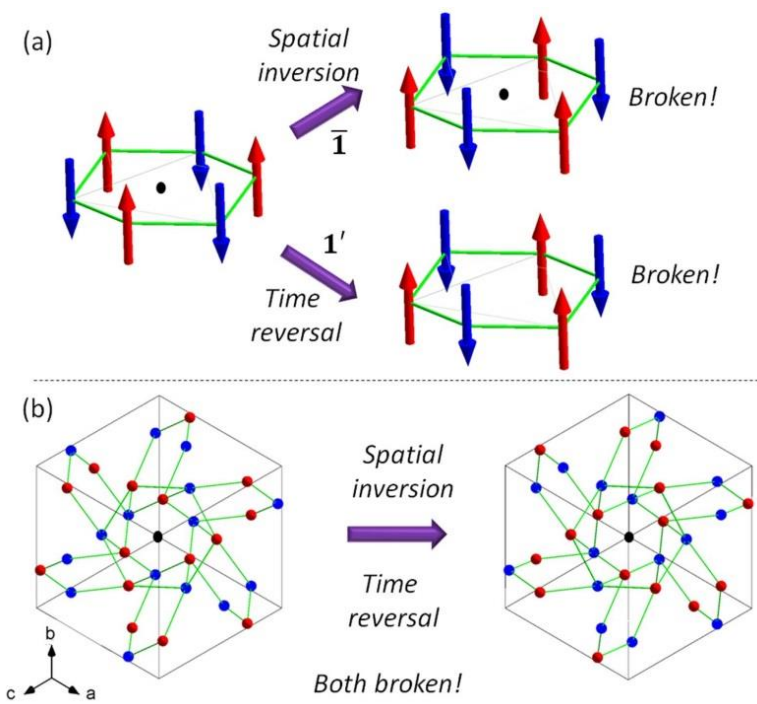


**Figure 5.11** Spatial inversion and time reversal symmetry of collinear spins (a) in one hexagon and (b) in one unit cell.

inversion center at the hexagon center and the time reversal symmetry ($1'$) is also broken (Fig 5.10(a)). In addition, the spin structure return to original when both of spatial inversion and time reversal is done, which satisfies the condition for linear ME effect. The symmetry of single hexagon remains same in the spin structure in the whole unit cell and this explains why the linear ME effect occurs in $Cu_3TeO_6$.

### 5.4.4. Monte Carlo (MC) calculation

In order to understand the linear ME effect in $Cu_3TeO_6$ we are performing *ab initio* calculations. Currently, we obtained the temperature dependent magnetization which indicates the antiferromagnetic order at ~62 K and the Curie-Weiss temperature of -149 K (Fig 5.10(a)). These results closely agree with the experimental data in Figure 5.3. The calculation also shows that the antiferromagnetic order parameter *L* decreases under higher temperature with similar line shape with the *P*. We expect that more details on the aspects and origin of the linear ME effect in $Cu_3TeO_6$ will be revealed by the successive MC calculation.

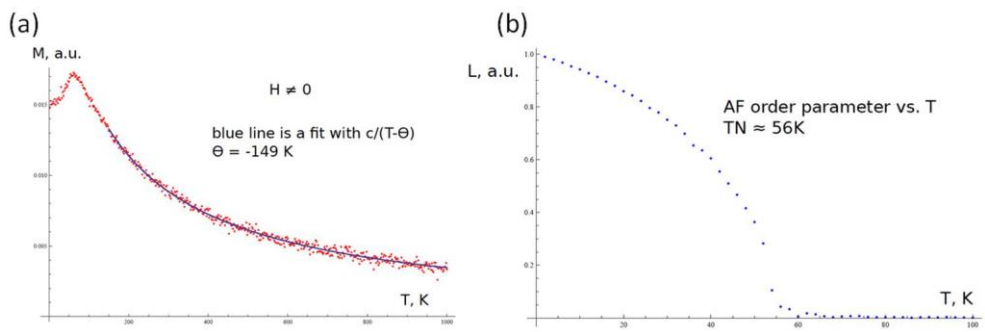


**Figure 5.12** Temperature dependence of (a) magnetization and (b) antiferromagnetic (AF) order parameter obtained from MC calculation.

## 5.5 Summary

In summary, we investigated the linear ME in the cubic system $Cu_3TeO_6$ which has antiferromagnetic ordering below $T_N$ = 62 K. The electric polarization *P* increases linearly by the magnetic field *H* below $T_N$ with linear ME coefficient of 1.8 ps/m at 2 K. The *P* shows ~10 times larger for $P \perp H$ than $P // H$ and shows maximum value of 20 $\mu C/m^2$ at 14 T for *P*//[110] and *H*//[1-10] with linear ME coefficient of 1.8 ps/m at 2 K. We analyzed the linear ME effect based on the magnetic point group, toroidal moment, and symmetry magnetic structure. Additional researches on the neutron scattering, as well as theoretical simulation will be helpful to understand further on the origin of linear ME coupling and the role of quantum effects in this material.

## 5.6 References


[1] Y. Tokura *et al.,* Rep. Prog. Phys. **77,** 076501 (2014).

[2] Y. S. Oh *et al.,* Nat. Comm. **5,** 3201 (2014).

[3] J. W. Kim *et al.,* Phys. Rev. Lett. **115,** 137201 (2015).

[4] M. Hudi *et al.,* Phys. Rev. B **84,** 180404 (2011).

[5] S. A. Ivanov *et al.,* Mater. Res. Bull. **46,** 1870 (2011).

[6] L. Zhao *et al.,* Phys. Status Solidi RRL **9,** 730 (2015).

[7] K. Y. Choi *et al.,* J. Phys.: Condens. Matter **20,** 505214 (2008).

[8] M. Manson *et al.,* Physics Procedia **30,** 142 (2012).

[9] M. Herak *et al.,* Solid State Comm. **151,** 1588 (2011).

[10] Z. He *et al.,* J. Magn. Magn. Mater. **354,** 146 (2014).

[11] G. Caimi *et al.*, Europhys. Lett. **75,** 496 (2006).

[12] Z. He *et al.*, J. Magn. Magn. Mater. **354,** 146 (2014).

[13] M. Herak *et al.*, J. Phys.: Condens. Matter **17,** 7667 (2005).

[14] M. Mansson *et al.*, Phys. Proc. **30,** 142 (2012).

[15] S. H. Chun, Ph. D. thesis (Seoul National University, 2013).

[16] R. R. Birss, *Symmetry and Magnetism* (North Halland Publishing Company, Amsterdam, 1966).

[17] N. A. Spaldin *et al.*, J. Phys.: Condens. Matter. **20,** 434203 (2008).

[18] T. Arima *et al.*, Phys. Rev. B **70,** 064426 (2004).

[19] Y. Yamaguchi *et al.*, Phys. Rev. Lett. **108,** 057203 (2012).

[20] Y. F. Popov *et al.*, J. Exp. Theor. Phys. **69,** 330 (1997).

[21] D. G. Sannikov *et al.*, J. Exp. Theor. Phys. **84,** 293 (1997).

[22] I. Kornev *et al.*, Phys. Rev. B **62,** 12247 (2000).

[23] T. Kimura *et al.*, Annu. Rev. Mater. Res. **37,** 387 (2007).

[24] K. Siratoni *et al.*, J. Phys. Soc. Jpn. **48,** 1443 (1980).

# Appendix A

## Pulse magnet system in Seoul National University

## A.1 Introduction

Magnetic field has been one of the most essential tools for research on physics, especially on condensed matter physics for a long time. Under the magnetic field, various physical properties of materials such as electric, magnetic and optical properties of materials which determine the fundamental parameters and give important information of the materials change. As the higher magnetic field is applied, new physical properties become visible. For example, magnetic field makes the change of parameters drastic and induces phase transition such as spin flip or spin flop transition. Furthermore, the high magnetic field makes it possible to invest peculiar quantum phenomena which are not understood with the classical regime. The quantum effects can be visible as a quantum hall effect, quantum oscillation, upper critical field and so on. Therefore, there have been lots of demands and efforts on the generation of higher magnetic field for the research on condensed matter physics area.

Various techniques to make magnetic field has been developed for more than one century. The most popular legend accounting for the discovery of magnet is that of an elderly Cretan shepherd named Magnes who lived in an area of Northern Greece about 4,000 years ago. He found the nails in his shoes become firmly stuck to a lock called Lodestons which contains magnetite, $Fe_3O_4$. Magnetite has ferrimagnetic order at room temperature showing remnant magnetization at zero

magnetic field and the remnant magnetization generate magnetic field. If the remnant magnetization of well conserved at room temperature, we call it **'permanent magnet'**. Many kinds of stronger permanent magnet such as $BaFe_{12}O_{19}$, MnBi, $SmCo_5$ and $Nd_2Fe_{14}B$ have been discovered. However, these magnets can generate limited and non-uniform magnetic field (maximum ~1 T in $Nd_2Fe_{14}B$).

The efforts to make higher magnetic field starts when Faraday made a **electromagnet** by winding a coil many times on an iron rod. If the electric current flows through the coil around the iron rod, high magnetic field is generated around the tip of the iron rod. From this electromagnet, it became possible to tune the magnetic field by controlling the current of the coil. High and uniform magnetic field ~3 T can be generated easily by cooling the coil with water. At higher field (>3 T), the iron core becomes useless only taking space. Thus, **solenoid magnet** without core has been developed, making it possible to generate up to 38 T recently at HFML-EMFL in Nijmegen, Netherland. However, this solenoid magnet requires tremendous amount of electric power. Since the magnetic field $\boldsymbol{H}$ made in solenoid is proportional to the electric current $\boldsymbol{I}$, the electric power needed to make $\boldsymbol{H}$ is proportional to $\boldsymbol{H}^2$. For example, the 33.5 T magnet in NHMFL of Tallahassee, USA uses electric power of 30 MW. Sometimes the usage of high field solenoid resistive magnets causes power outage of the whole city of Tallahassee. In addition, the resistive solenoid magnet requires efforts to deal with the Joule heating in the coil from the high current.

In order to overcome these problems, a new kind of magnet called **'superconductor magnet'** has been also developed. Since the electric resistivity is

zero in the superconducting phase, there is no power loss as a Joule heating, thus constant magnetic field can be maintained using no additional electric power. Especially, after the superconducting wires like Nb-Ti and $Nb_3Sn$ alloys were invented, the superconducting magnet have been commercialized rapidly so that it can be used in small laboratories. For cooling down to the superconducting states of the wires, usage of liquid helium became necessary and its demand also increased a lot in the condensed matter research area. One of the reasons why the Nb-Ti and $Nb_3Sn$ alloys are useful as the superconductor magnet wire is their high upper critical field. They can generate magnetic field up to 20 T at liquid helium temperature, however, that is limit because the field should not exceed the upper critical field in which the superconducting state turns to the normal state. Recently, superconducting wires using high temperature superconductors like $YBa_2Cu_3O_{7-x}$, $Bi_2Sr_2CaCu_2O_{8+x}$ and $MgB_2$ are under development. Even though there are difficulties of high price and stiffness, it is continuously developing and 32 T superconductor magnet was realized in NHMFL, Tallahassee.

Another important achievement to reach higher magnetic field of resistive and superconductor magnet is 'hybrid magnet', which uses the both the superconducting and resistive magnets. A resistive magnet is set inside and superconducting magnet is put outside because lower field should be applied on the superconducting magnet in order to maintain the superconducting state. The current world best magnetic field reached in NHMFL, Tallahassee, USA is 45 T. Furthermore, continuous research and development is going on to generate field up to 60 T hybrid magnets.

There is another method to make high magnetic field more easily rather than the

previous static magnets. It is **pulse magnet** that generate high magnetic field in short time, less than 1 second. The history of this pulse magnet starts with the Kapiza who generated 30 T pulsed field using a generator, in Cambridge University, in 1923. He measured first time the electric resistivity of Bi under the pulsed field. The pulsed field is realized by flowing extremely high current through a strong solenoid in short time using DC generator or capacitance. The most important problem for generating pulsed magnet is that strong Maxwell stress caused by the high current in short time. The stress increases quadratically upon increasing the maximum field, for example, 1.95 GPa in 70 T and 3.98 GPa in 100 T. In order to let the magnet endure and distribute the Maxwell stress uniformly, choosing an appropriate wire materials and design of the magnet are essential to reach higher pulsed magnetic field. Several copper alloy materials for pulsed magnet wire such as Cu-Be, Cu-Nb, Cu-Ag shows much larger tensile strength than copper. Especially, Kindo in Osaka University reached 80 T non-destructive pulsed field in 2001. The highest magnetic field in the non-destructive pulse magnet reached 100 T in NHMFL in Los Alamos in 2011.

Currently, more than 100 T cannot be realized in the non-destructive magnet, thus destructive method should be used. Several methods such as explosive method, one round coil method and plasma method were developed in 1950s and 1960s. In 1996 and 1997, an international cooperation including USA, Russia, Japan, Austria, Germany, Belgium succeeded to reach 1000 T using the explosive method. In this explosive method, whole experimental set up, coil, cryostat, samples are all destructed, remaining only data. On the other hand, the one round coil method can generate up to ~300 T, destructing only the Coil, thus sample and cryostat is

reusable.

There are several big high magnetic field facilities in the world. They are (1)NHMFL in Los Alamos, USA, (2) EMFL in Dresden, Germany, (3) EMFL in Toulouse, France, (4)WHMFC in Wuhan, China (5) ISSP, Kashiwa, Japan. They are competing each other for the world best record of magnet systems. However, there is no high field facility, thus most high field researchers should rely on the facilities in foreign country.

In this regard, we started to set up a pulse magnet system at prof. Kee Hoon Kim's laboratory in Seoul National University from 2011 with prof. Zeehoon Jang in Kookmin University. We succeeded to generate up to 30 T with full pulse width ~0.1 s and measurement of magnetoresistance became possible under the pulse magnet. In this chapter, we state the details of the pulsed magnet system. In the section A.2,3,4, we explain the detail of each parts of the system and knowhow that accumulated during the construction. In the section A.5,6, we explain procedure of the pulse field experiment including the generation of the field and measurement of physical properties. Some important cautions the experimenter should take in mind and some preliminary results are also included. In the section A.7, we stated how to do maintain the system. we hope that this charter will be helpful to juniors in our laboratory and many students who pursue researches on high magnetic field.


**Figure A.1** Pulse magnet facilities in several countries

## A.2 Pulse magnet system

In this section A.2, we state the details of the pulsed magnet system. The field generating system, measurement system, gas handling system will be included.

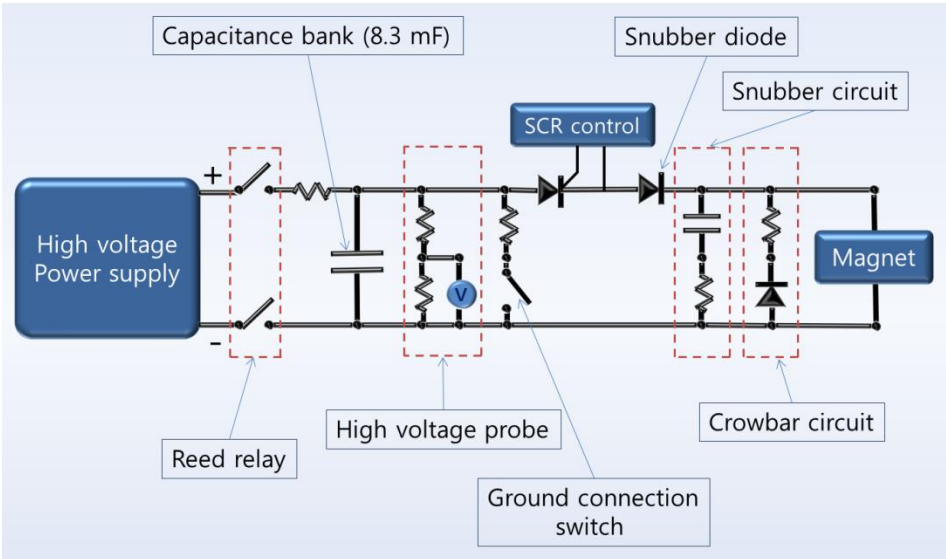


**Figure A.2** Overall circuit for generation of pulsed field

The Figure A.2 shows the overall circuit that makes the pulsed magnetic field with the capacitor bank. The process of pulsed field generation is as below. If we turn on the high voltage power supply and close the reed relay, the electric power is accumulated in the capacitance bank. The charged voltage of the capacitance bank can be monitored by the high voltage probe. After the electricity is charged to the aimed level in the capacitors, we open the reed relay and turn off the high voltage power supply. The charged state is very dangerous state because we usually charge it more than 1000 V. Thus, in order to dissipate the charge automatically in an emergency situation, a high resistor (~500 kΩ) is connected in parallel with the

capacitor bank in real circuit. Now, there are two choices to discharge the electric power in the capacitance bank. First choice is to dissipate as heat in resistors by closing the ground connection switch. This choice is used when the electric power cannot be flowed to the magnet because of some emergency situation. Another choice is to switch the Silicon Controlled Rectifier (SCR) to let the electric power to flow to magnet as a high current. Here, the snubber diode and snubber circuit is for preventing the counter flow of the current because of the inverse voltage due to the Lenz's law in the magnet coil. In the real circuit, the snubber circuit is not included because the only snubber diode is sufficient to avoid the counter flow. The crowbar circuit let the current from the magnet flow when the magnetic field is decreasing. By changing the resistance of the crowbar resistor, we can also tune the decreasing speed of the magnetic field.

### A.2.1 Principle of the pulse field generation

The circuit can be simplified to include the capacitance *C*, (crowbar) resistance *R*, and (magnet) inductance *L*. In order to understand the magnetic curve, we have to analyze the current flowing through the magnet coil separating the case of increasing current and decreasing current. When the SCR is turned, the current starts to flow from capacitance to the magnet coil. In this time, the current cannot flow through the crowbar circuit because the voltage of upper line is higher. Thus, during the current on the magnet increases, the circuit can be considered as a *LC* circuit in which the current oscillate with the frequency of $f_{\mathrm{LC}}$.

$$f_{LC} = {}^{1}\!/_{2\pi\sqrt{LC}} \qquad \text{(A.1)}$$

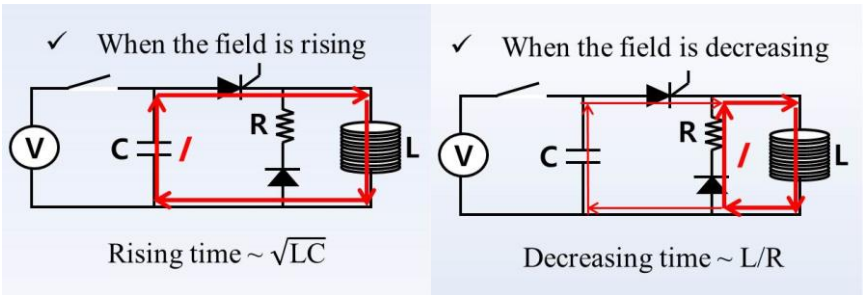


**Figure A.3** Schematic of current path in the pulse magnet system for increase and decreasing time

Thus the time from turning on of the SCR to reach the maximum current in magnet (proportional to magnetic field) is proportional to $\sqrt{LC}$. Until the time of maximum current of magnet, all of the electric energy accumulated in the capacitance bank was transferred to the magnet coil. After that, the sign of voltage between the upper line and lower line change and the current of magnet flows through the crowbar circuit. Here we set up the snubber circuit, so that the current cannot flow back to the capacitance because the capacitance can be damaged if it is charged with inversed voltage. Therefore, when the current (magnetic field) decreases, the current flowing circuit can be considered as *RL* circuit. Thus, the

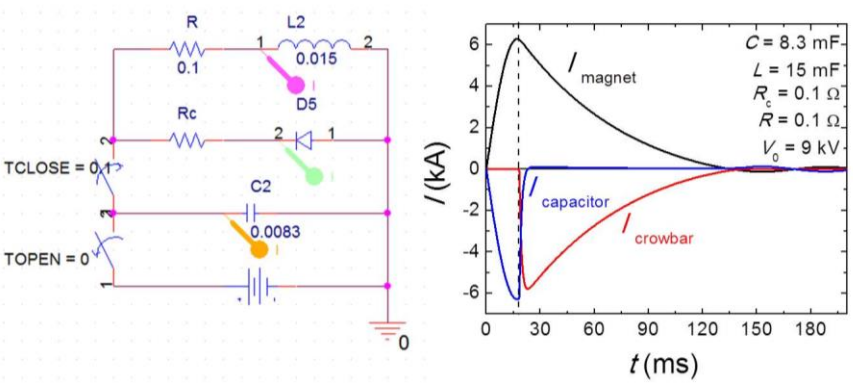


**Figure A.4** Pspice simulation of the current in the pulse magnet circuit. (left) Pspice simulation circuit. (right) result of simulation of currents on magnet, crowbar and capacitor.

current decreases exponentially, with the time constant proportional to the *L/R*. As we can easily notice, the pulse width of the magnetic field increases as the R decreases.

We conducted simulation of the pulse magnet circuit using software called 'pspice' (Fig. A.4). In the simulation, the parameters of each devices was set as some proper and similar value with real values. $R_c$ is crowbar resistance and $R$ is resistance of connection between each devices. As we expected, the increasing current flows between capacitance and magnet, whereas the decreasing current mainly flow between the crowbar circuit and magnet. When the current of the magnet (proportional to the magnetic field) starts to decrease, the current of capacitance decreases and the current of the crowbar increases rapidly.

The pspice simulation was done with change of the $L$, $R$ and $R_c$ as well. When the inductance is increased, the pulse width is increased, however, the maximum current decreased. This character can be used for designing the pulse magnet coil. First, if the inductance $L$ of the pulse magnet coil increases, the pulse width increases, but the maximum field decreases. With this result, we can know that more coil winding can generate larger magnetic field per unit current, however, the inductance of the coil increases, thus the maximum generated current decreases

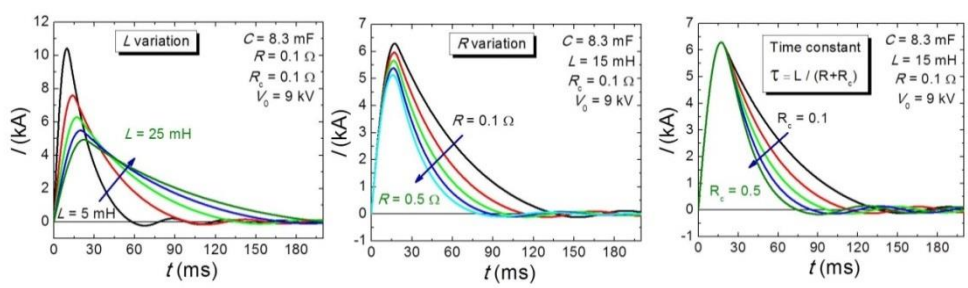


**Figure A.5** Pspice simulation of the current in the pulse magnet circuit changing the parameters, $L$, $R$, $R_c$.

again. If the *R* increases, both of the maximum current and pulse width decreases. The *R* is related to how the electric connections between the devices are well done. For example, we usually connected each part electrically by pressing copper block. If the surfaces of the copper are get lusted, *R* will increase resulting in decrease of maximum magnetic field and pulse width. At last, if the crowbar resistance $R_c$ increases, the magnetic field decreases more rapidly. Thus we usually use the lowest crowbar resistance to realize the longest pulse that can be generated. Meanwhile proper setting of the crowbar resistor can rather prolong the lifetime of the capacitor bank. Even if this simulation gives some important qualitative information, we should keep in mind that the actually magnetic field simulation is much more complicated taking account of temperature, tensile strength and so on.

Let me show a magnetic field curve that obtained from the pulse magnet system in Seoul National University. This curve was obtained by integrating the induced voltage signal from a pick up coil. I explained more detail in Chapter A.3, experimental part. By increasing the charging voltage, the maximum magnetic field increase linearly. This is reasonable result because the energy accumulated in the

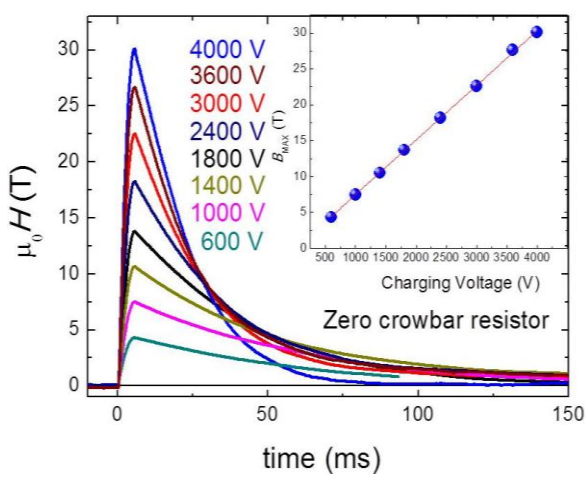


**Figure A.6** Magnetic field curve in the pulse magnet system in Seoul National University

capacitors is proportional to $V^2$ and the energy of magnetic field in the magnet is proportional to the $B^2$. In the magnetic field curves, we can notice that the pulse width decrease as the maximum field increases. For $B_{max}$ ~ 5 T, the full width of field is more than 200 ms, whereas the full width decreases to ~ 100 ms (FWHM ~25 ms) for $B_{max}$ ~ 30 T. This phenomenon occurs due to increase of resistance of the magnet coil by heating of the coil during the pulse. Maybe slight increase of the magnet radius can also decrease the inductance resulting in the shorter pulse width.

### A.2.2 High voltage power supply and reed relay

High voltage power supply is an essential part to charge the capacitors. We should consider the maximum voltage ($V_{max}$) and maximum current ($I_{max}$) for choosing the proper power supply for pulsed field. We chose a domestic company to purchase a power supply with $V_{max}$ = 10 kV and $I_{max}$ = 500 mA. It is also possible to use high voltage transformer and rectifier which works as a power supply. In the high voltage equipment like the power supply, the insulation of the cables connected to the capacitor bank should be specially taken care with silicon, rubber and Teflon. In addition, the distance between the high voltage and ground line is more than 10 cm.

For switching and charging to the capacitor bank, high voltage relay should is set between the power supply and cap bank. We used four high voltage reed relays, two for high voltage line and two for ground line. This is for safety when one of the reed relay break down. We chose the reed relays with break down voltage of 15 kV and $I_{max}$ of 3 A which are larger than them of the power supply. The reed relays are switched by applying 24 V on the coil with control of lab view program. It is

noteworthy that we should choose option of 'Normal open', which means 'open' without voltage in coil, in order to open at the time of electrical breakdown. The box of the reed relay is made of plastic, so that it can insulate between the devices.

We also set a charge resistor to prevent the over-current when we charge the capacitor bank. The chosen resistor is a heat sink resistor TAP 2000 series (500 Ω) which has a flat surface for the heat sink. In order to reduce the heating of the resistor, we used an aluminum block with large surface area.

### A.2.3 Capacitor bank

In this section, I explain what kind of capacitor bank we used and how we should deal with them.

We used 10 capacitors of 830 μF (total 8.3 mF) of maximum voltage 9 kV which were purchased from ICAR, an Italian company. I set the capacitor bank with the sequence written below. The frame for storing the capacitor bank was made by hand with Aluminum frame and CRC boards which are incombustible, impact resistive, decay resistive, light and cheap. At each joint, I put the aluminum molding and applied the industrial epoxy which can be cured at room temperature.

The connectors between the capacitors were made with braided wires and terminal lug which are sufficiently big ($d$ ~ 3 cm). I used the braided wire to make the connection flexible so that the capacitors are not damaged when they moves during the pulse. The

**Figure A.7** Capacitor bank of 8.3 mF with $V_{max}$ = 9 kV.

braided wires and terminal lug should be pressed well together and also soldered by lead. The terminal lug should be grinded very flat so that the electrical conduction can be maximized.

We should take special cares when we deal with the capacitor bank. First, we should make sure that the ceramic part of brown color is not damaged. A whole capacitor can become useless because of a small crack of the ceramic part. Especially, when we connect the braided wires, torque wrench should be used so that the torque more than certain amount will not be applied to the ceramic part. Second, when we do not use the capacitors, the plus and minus electrodes of the capacitors should be electrically connected. Since the capacitors can be automatically charged slightly because of some reasons like humid weather, this can result in electrical shock. Third, we should decide which electrode is plus and which one is minus and should not change it. The capacitors can be charged only in one direction, thus it can be damaged if it is charged more than 20 % of maximum voltage inversely. Forth, when we charge, it should be clean around the electrode without dust before charging the capacitors. The dusts can case the electrical shock when charging the capacitors. At last, since the maximum operation voltage is 9000 V, it is safe to charge up to 6000 V (We are using up to 4000 V currently). If we charge close to maximum voltage for a long time, the capacitors can be broken.

※ Siren - For the pulse magnet system, the safety is the most important. In the National High Magnetic Field Lab in the Los Alamos, a siren is alarmed when the capacitor bank is charged so that people cannot get close to the high voltage system. We also set a siren which operate during the capacitor banks is charged.

### A.2.4 Switching unit of the pulse field

After we charge the capacitors, we need to deal with the electricity, switch it to magnet or discharge to the ground directly. I put together the devices including the high voltage probe, SCR, diodes and so on. The design and construction of this switching unit was done carefully to be operated safely with the high voltage.

The aluminum frames with the wheels to support the switching unit were prepared from the same company as that of capacitor bank. On the aluminum frame, five ceramic insulators were set to support the devices and insulate between flour and high voltage parts. We chose the ceramic insulators which can endure high voltage up to 60 kV (TR-208). On the insulators, we put two G10 plates (1 cm) and one Cu plate (0.5 cm) with sandwich geometry. The copper plate is to connect electric ground. On the plates, we put 3 cages to put the SCR and diodes in. These cases are to contact the devices with copper plates uniformly by pressing with certain force. The SCR and diodes are connected with the thick (t = 1 cm) copper plates. Before connecting the devices, we should make sure that surfaces of the copper plate are polished well so that they shine like a mirror. When we connect the devices, the height of the each connection should well match and the contact with the devices should be uniform. Otherwise, the devices can be damaged at the

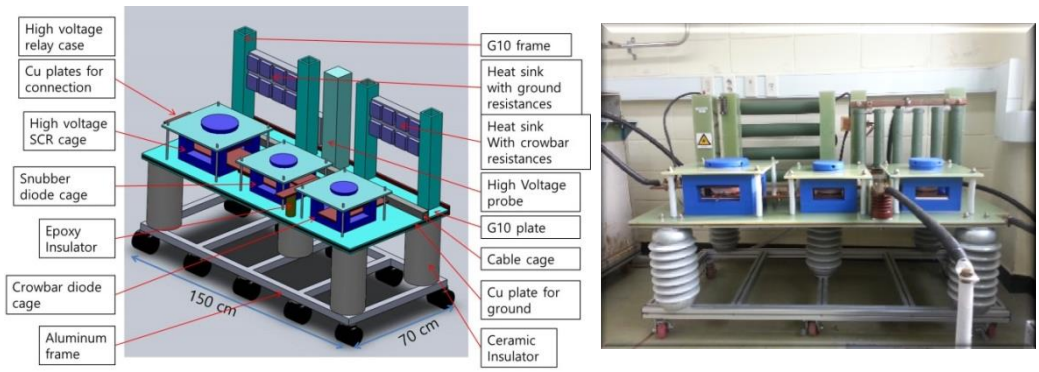


**Figure A.8** Original design (left) and constructed (right) switching unit

time of pulsing. Other devices, ground resistors, high voltage relay, crowbar resistors was set on the back side of the switching unit with the G10 frames.

### A.2.5 High voltage probe

The high voltage probe is for measuring the voltage charged in the capacitor bank. We need a special device to measure such high voltage up to 10 kV. We chose a FLUKE 80K-40 which can probe voltage up to 40 kV. The high voltage probe is simply made of a voltage divider with the input resistance of 1 GΩ and divide ratio of 1000 : 1. Thus, if 1000 V is charged in the capacitors, the output voltage we measure is 1 V. We made a frame with G10 to use the probe safely. The tip part of the probe is connected to the high voltage. At the bottom of the probe, there is a connector to ground and two connectors for output. The output signal is directly read by a panel meter which is included in the pulse control circuit.


**Figure A.9** Housing of the high voltage probe

### A.2.6. Ground resistors and ground connection switch

The ground resistors are used to discharge the electric power of capacitor bank without pulsing to the magnet and ground connection switch is to switch it to the ground. In order to choose proper ground resistors, we should understand how the charge dissipates in the time scale. When the switch is close, the current suddenly increase to the maximum and decreases exponentially, with the maximum current of $V_o/R$ and time constant of $RC$. The total energy in the capacitor is $(1/2)CV_o^2$. In our case, the maximum voltage to charge is 4000 V and chose the four resistors of 500 Ω with each 2000 W that means 2000 Ω with 8000 W. In this case, the maximum current is less than 2 A and the maximum power will be less than 8000 W. Thus the resistor will be operated safely. In actual case, because the current will decay exponentially, it can be operated using the smaller resistance, with 1500 Ω of 6000 W. We have to use power resistor which is designed to dissipate high power as heat. The power resistor shown in the figure is made by winding metal wire on a ceramic cylinder. We have tried to use the TAP 2000 series first time, however, they broken even though the spec of the series is 2000 W. The TAP 2000 serious does not satisfy its spec, because it is film resistor, possibly.

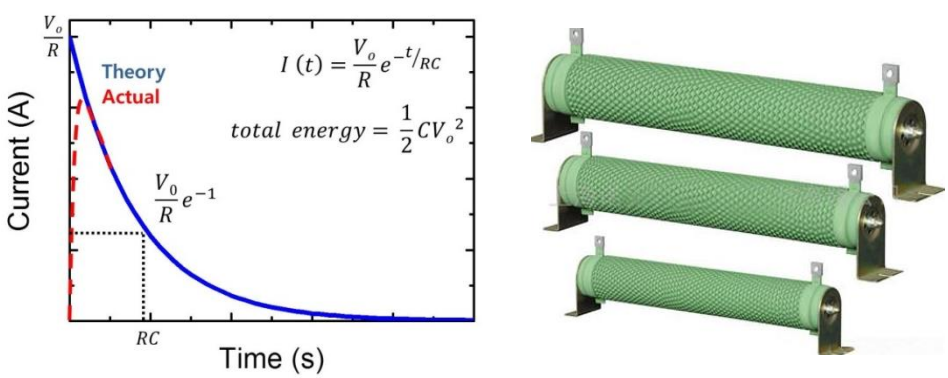


**Figure A.10** Current curve on the ground resistors (left) and the high power resistors

We used a high voltage relay for switching to the ground whose break down voltage and maximum current are 10 kV and 5 A, respectively. The switching is done by applying 12 V to the coil. It should be 'normal close' to discharge automatically at the time of electrical breakdown. In this case, we have to connect thick wire because of the high current, however, the relay itself was too small. First, we made the connector bigger using terminal lugs. Second, we made a box with acrylic plates. Third, put the high voltage relay with the large connector into the acrylic box. Fourth, pour out the industrial epoxy and fill up the acrylic box. At last, dry it for a day.

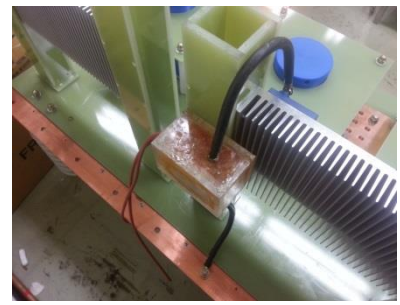

**Figure A.11** ground switching relay

### A.2.7. Silicon Controlled Rectifier (SCR)

In order to switch the charged capacitor bank into the magnet, we used a SCR. SCR is a four-layer solid state device that is controlled by current. The SCR is general electric's trade name for a type of thyristor. SCR include four semiconductor layer, forming NPNP or PNPN structure. In PNPN structure, the anode is connected to the P type and the cathode is connected to the N type while

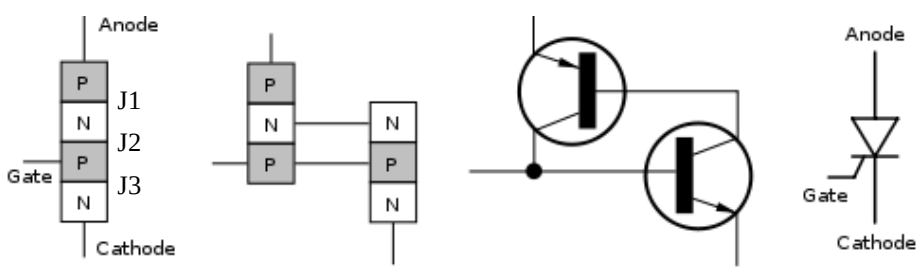


**Figure A.12** Diagram of silicon controlled rectifier

the gate is connected to P type which is the nearest to the cathode. The operation of an SCR can be understood in terms of a pair of tightly coupled bipolar junction transistors, arranged to cause the self-latching action. There are three modes of the SCR as listed below.

1) Forward blocking mode: Anode positive voltage, cathode negative voltage, gate disconnected. J1 and J3 are forward biased, while J2 is reverse-biased. J2 make high resistance, the blocking mode.

2) Forward conduction mode: anode positive voltage, cathode negative voltage, gate pulse current. Due to the pulse current between gate and cathode, J2 undergo breakdown and start to be conducting. In this case, the short time (~ms) of the gate current is enough to trigger the SCR.

3) Reverse blocking mode: anode negative voltage, cathode positive voltage, gate pulse current J1 and J3 are reverse biased. And they cannot become conductive due to the pulse current in the gate.

In the pulsed magnet experiment, we make the forward conduction mode to flow the high current to the to the pulse magnet coil. Therefore, the SCR should be high current type. We used a SCR of mode 'T1901N80TOH' from Infineon, whose maximum voltage between anode and cathode is 8000 V and maximum RMS on-state current is 3300 A. Note that we should apply certain force between anode and cathode. The resistance between the gate and cathode becomes ~5 Ω if we apply force whereas it is insulating before the force. We should take care not to apply to much force between the SCR.

### ※ Triggering of the SCR

- The triggering of the SCR is one of the most crucial parts in the pulse magnet system, thus it should designed and conducted carefully. It is important to make the triggering parts are all separated with any other electric devices. This is because some noise from other devices can give rise to unintended trigger of the SCR. Therefore, the laser generator and triggering circuit should be operated only by battery. In addition, the trigger signal is generated by laser which is guided by optical fiber since the laser is not disturbed by radiation noisy from lots of noisy sources inside the room. The triggering circuit converts the light (laser) from the laser generator to the electric voltage to flow current between the gate and cathode and mainly made of the plastic fiber optic photologic detector (IF-D97) and the PECL (positive emitter coupled logic) to TTL (transistor-transistor logic) (MC100ELT21).

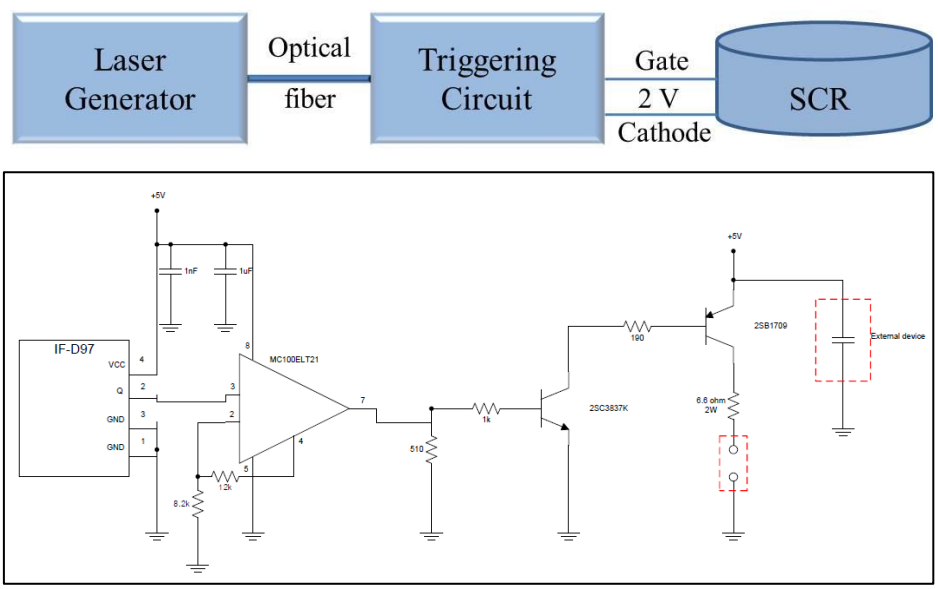


**Figure A.13** (upper) connections for the triggering (lower) triggering circuit

### A.2.8. Snubber diode and snubber circuit

The term ‘snubber’ include the meaning of suppress (“snib”), and the snubber is a device to which suppress the sudden change of voltage of the circuit. In the pulse magnet system, the snubber diode and snubber circuit is used for preventing the counter flow of the current because of the inverse voltage due to the Lenz’s law in the magnet coil. The snubber circuit usually made of a resistor (R) and a capacitor (C) which are connected in series. By the way, in our circuit, we did not use the RC snubber circuit and only used the snubber diode because it is sufficient to prevent the inverse voltage. In addition, it is noteworthy that the SCR also works as another snubber diode. For the high current operation, we used a diode of model D2601N85T (Infineon) whose maximum voltage is 9000 V and the maximum RMS on-state current is 4820 A.

### A.2.9. Crowbar circuit

As we stated above, the crowbar circuit make current path during the field decreases. This is done by using a crowbar diode which prevents the current at the field rising time and arrow the current at the field falling time. The same high voltage diode as that of snubber circuit (D2601N85T, Infineon) is used here. The decreasing time can be controlled by the magnitude of the crowbar resistor ($R_c$); low $R_c$ increases, and high $R_c$ decreases the falling time of field. We usually do not connect the crowbar resistors in order to maximize the pulse width. However, appropriate $R_c$ (~0.1 Ω) can make the lifetime of the capacitor bank longer. The crowbar resistors should be also the high power resistor since high current flow through them.

### A.2.10. Pulse magnet

The design and construction of the high field pulse magnet is the most important and difficult part among the pulsed magnet system. For other parts, it is not difficult to improve the spec for higher magnetic field whereas it is extremely tricky to design the magnet to overcome the magnetic pressure and prevent destruction of the magnet. Therefore, the maximum non-destructive pulsed magnetic field is determined by the design of the magnet. The magnetic pressure is written as

$$P = \frac{1}{2\mu} B^2 \qquad \text{(A.1)}$$

where the *P* is magnetic preessure, and the *B* is magnetic field. For example, *P* is 0.36 GPa for 30 T , 1 GPa for 50 T and 4 GPa for 100 T.

In order to overcome the magnetic pressure, we need to use wires with high tensi le strength. We can see that the tensile strength of Cu is ~250 MPa and is more than 4 times larger in the Ag or Nb doped wires even though the resi stivity and stiffness are higher. The Kindo's group in ISSP generated up to

| Material | UTS [MPa] | | Strain [%] | | $\rho$ [μΩ·cm] | |
|---|---|---|---|---|---|---|
| | 293 K | 77 K | 293 K | 77 K | 293K | 77 K |
| Cu | ~250 | 400 | ~20 | ~40 | 1.77 | 0.214 |
| Strengthened Cu | 400 | 450 | 8 | 20 | 1.67 | 0.25 |
| Cu-24% Ag | 1070 | 1250 | 2.9 | 2.5 | 2.1 | 0.75 |
| Cu-18% Nb | 1100 | 1300 | 5.4 | 4.4 | 2.6 | 0.58 |
| Cu 45 % Steel clad | 956 | 1290 | 1.8 | 2.2 | 3.4 | 0.53 |
| GlidCop AL60 | 620 | 850 | 9.2 | 16.6 | 2.1 | 0.54 |
| GlidCop AL15 | 450 | 590 | 7.0 | 18 | 1.86 | 0.36 |
| S2-glass fiber | | 2600 | | 3.7 | | |
| Carbon fiber | | 3000 | | 1.2 | | |
| Zyloc fiber | 2800 | 3200 | | 1.4 | | |
| MP35N ribon | | 2600 | | 1.1 | | |

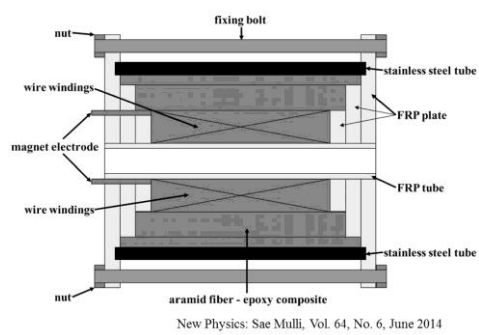


**Figure A.14** Ultimate tensile strength (UTS), Strain and resistivity of materials used for pulse magnet (left) and the cross-section view of the pulse magnet in SNU (right)

80 T using the Ag-planted Cu wire. In addition, we can use the glass, carb on, Zylon fibers to reinforce the magnet.

The pulse magnet in SNU was designed and constructed by prof. Zeehoon Jang in the Kookmin University. We used Cu wire with rectangular cross sect ion of 3 mm x 2 mm and reinforced using E-glass fiber, aramid fiber and Stycast 2530. The wire wound magnet structure is enclosed in the nonmagnetic stainless steel 316 tube and the gap between the stainless steel tube and wire wound magnet structure was filled with epoxy. We should note that the actual design of a pulse magnet is much more complex, since we should consider and calculate many variables such as temperature, resistivity, stiffness of wire and stress distribution. More details of the magnet design are written in a published paper [1].

### A.2.11. Control circuit and control program

Most of the pulse magnet system such as relays, power supply should be operated from a separated place. The diagram and details of the control circuit are written below.

First, in order to control and read signals of pulse magnet system from computer we used a DAQ board (BNC 2110, National Instruments), DAQ is extremely convenient to control and read the analog and digital signal of 5 V. BNC 2110 consists of a main board, a cable and a PC board. We use the analog ports to control and read the voltage and current of the high voltage power supply. And we use the digital ports to control the relays. The board installed in the computer enables us to control DAQ with the Labview program.

Second, we used the reed relays for relays 1 to 5, which can be switched by

applying 5 V, the digital signal of DAQ. These small relays are used to switch the 24 V and 12 V power to the high voltage relays.

Third, the power supplies (SMPS 12 V, SMPS 24 V) are used to switch the high voltage reed relay and ground connection. When we choose the power supplies, we should consider the available currents of them. We used power supplies with maximum currents 0.4 A, 0.34 A, and 0.6A for 24 V, and two 12 V, respectively.

Fourth, we used a panel meter (MT4W, Autonics) to read voltage signal from the high voltage probe. The range is from 0 V to 10 V.

Finally, I give several tips to make the control circuit efficient and well working. 1) Use the PCB fixing the devices to make the devices removable when one of them is broken. 2) Use the terminal block and terminal lug to connect wires. It is efficient to make all of the wires detachable easily with one driver. 3) Use the wires with different thickness according to the current and voltage we use. 4) Use the co-axial wire to read and control the analog signal since the DAQ is quite noisy.

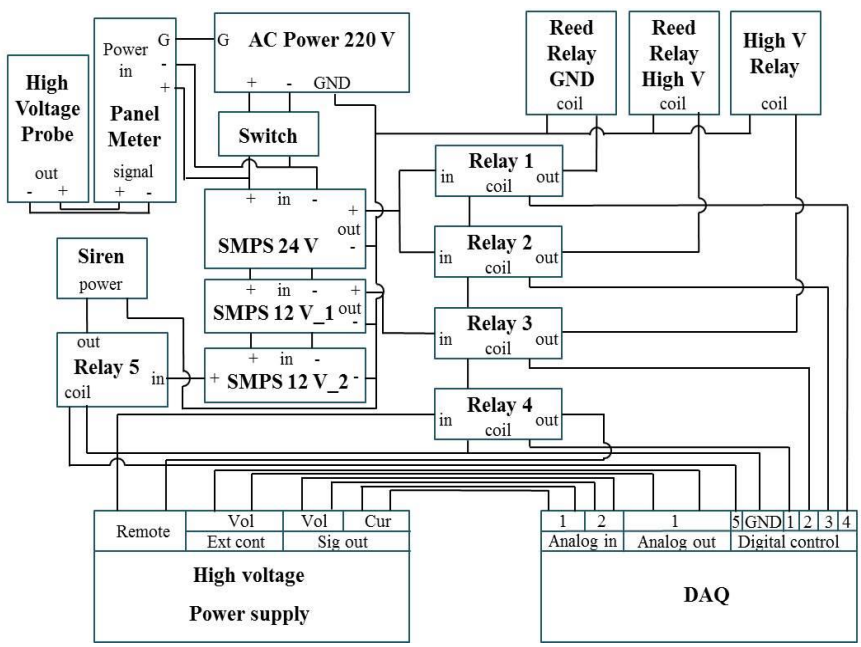


**Figure A.15** Diagram of the control circuit of the pulse magnet system


**Figure A.16** Picture of inside (left) and front (right) of the control circuit of the pulse magnet system

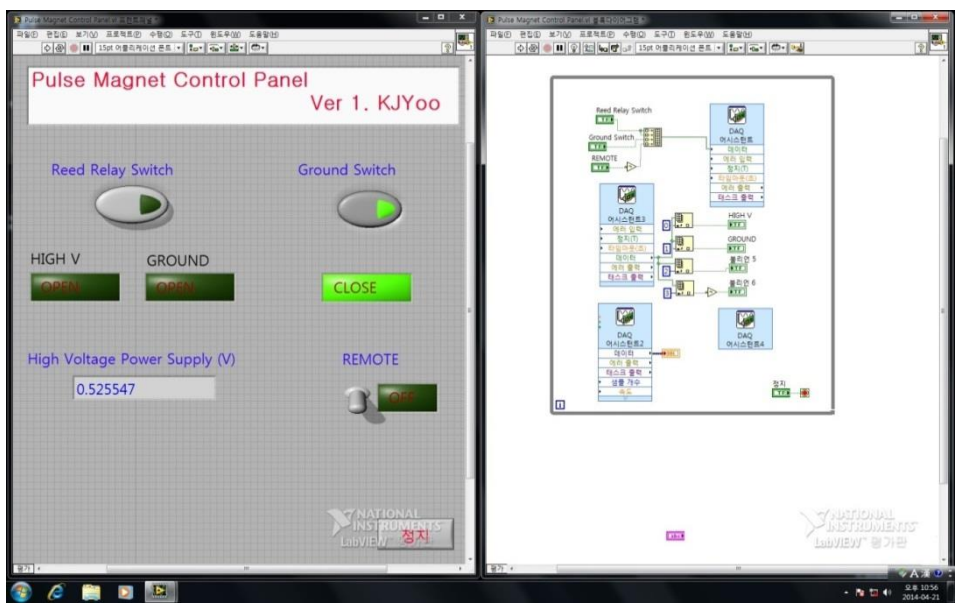


**Figure A.17** The Labview program for the control circuit of the pulse magnet system

※ Labview program of the control circuit.

- The Labview program is easily made by use the DAQ assistant. The ‘REMOTE’ tap switches the high voltage power supply so that we can control it using the Labview program. We can switch the reed relay and ground relay. And we can also apply high voltage by putting number in the ‘High Voltage Power Supply’ tap. Note that 2000 times larger voltage than the input number will be applied.

### A.2.12. Items for safely

- Since the pulse magnet experiment uses high voltage and thus is extremely dangerous experiment, we should use special items for safety. The ground stick is used to confirm that the each part is completely discharged. The tip part of ground stick is connected to ground and other parts are insulated with plastic and insulating tape. In addition, we should wear insulating glove (max 17000V) and boots (max 20000V) when we are close to the pulse magnet system. In addition, we need to prepare the fire extinguisher for the emergency. Especially, it should be ‘C’ type for the fire from electricity.


**Figure A.18** The items for safety. Ground stick (left), insulating glove and boots (middle), and fire extinguisher (right).

## A.3. Cryogenic systems

In order to investigate the quantum phenomena in the condensed matters, thermal fluctuation, which come from the nonzero temperature, should be minimized. Therefore, high magnetic field experiments are often done at low temperature. Since expensive helium 4 and helium 3 are used to cool down to ~0.5 K, and in order to conduct stable low temperature experiment, we should design and make the cryostats and gas handling system carefully. In our cryogenic system includes liquid nitrogen/liquid helium 4 cryostat, helium 3 cryostat and helium 4/helium 3 gas handling system.

### A.3.1. Liquid nitrogen/liquid helium 4 cryostat

The figure below shows the design of the liquid nitrogen/liquid helium 4 cryostat. There are vacuum layers between room temperature and liquid nitrogen ($LN_2$) area and between $LN_2$ area and liquid helium 4 ($L^4He$) area for thermal insulation. The vacuum layers should be vacuumized down to 1E-7 mbar before experiments. The pulse magnet is set in the $LN_2$ area so that the thin tip part of $L^4He$ area goes inside of the magnet. This means the magnet is cooled down to 77 K during the operation. The tip part of $^4He$ area is connected by indium seal. Note that the whole cryostat should consist of totally nonmagnetic Stainless. Since most of domestic products are slightly magnetic, we purchased the thin SUS 304 tube with $t$ = 0.5 mm from a Japanese company. The amount of $L^4He$ in the cryostat is 7.67 L. All of the in/out ports are made with NW 40 and O-ring seal. However, the sealing of the O-ring part is not perfect.

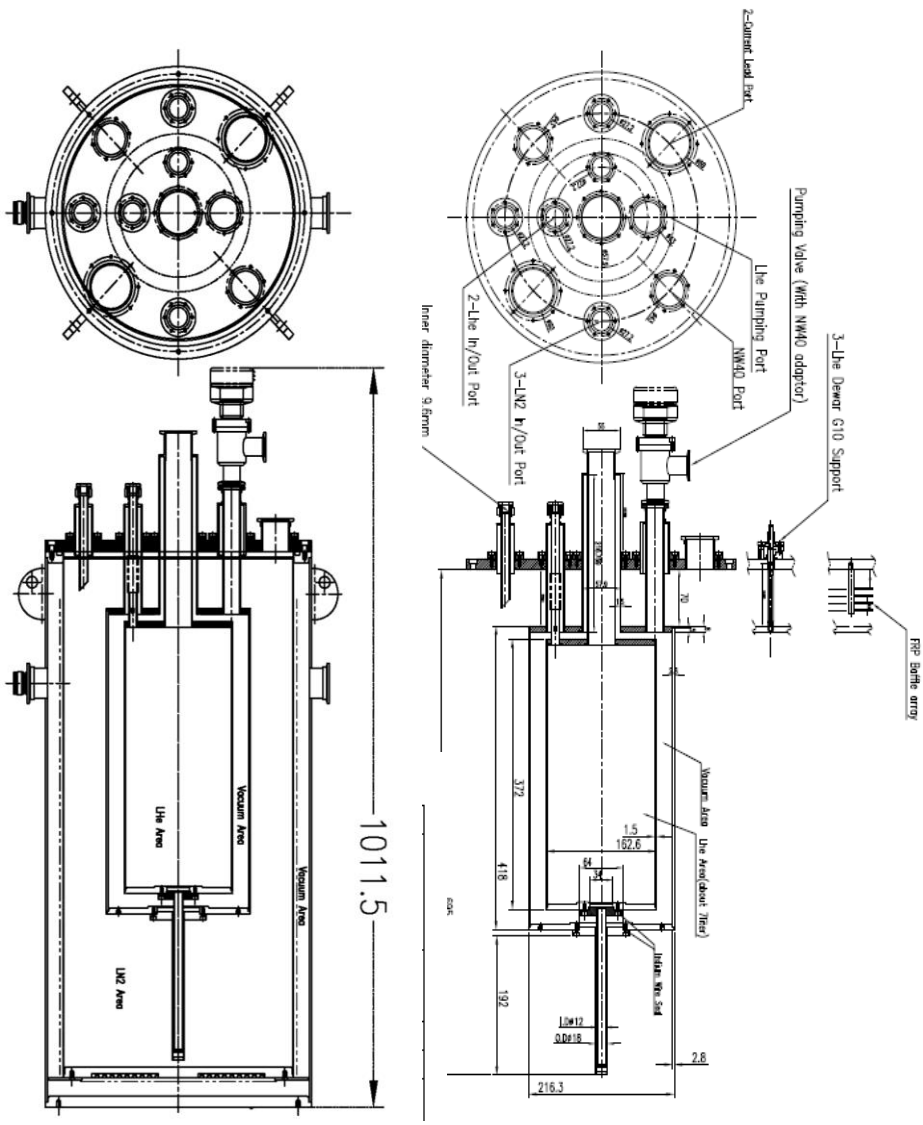


**Figure A.19** The design of the $LN_2$/$L^4He$ cryostat (designed by prof. Jang)

**※ Setting of the cryostat inside of a hole.**

There are several advantages to set the cryostat in a hole of flour. First, it is better for safely. In the case, the pulse magnet is destroyed, the stuffs outside of the cryostat can be also damaged, therefore, setting it in a hole can protect other equipment from the magnet. Second, the cryostat can be fixed more firmly inside the hole. At last, the hole can protect the measurement from the radiation noise. Because the hole was too deep at first time, we filled it with sand up to appropriate height for setting of the cryostat and put an aluminum plate with thickness of 1 cm. The cryostat in the hole was further fixed on the bottom and wall of the hole by G10 plates.

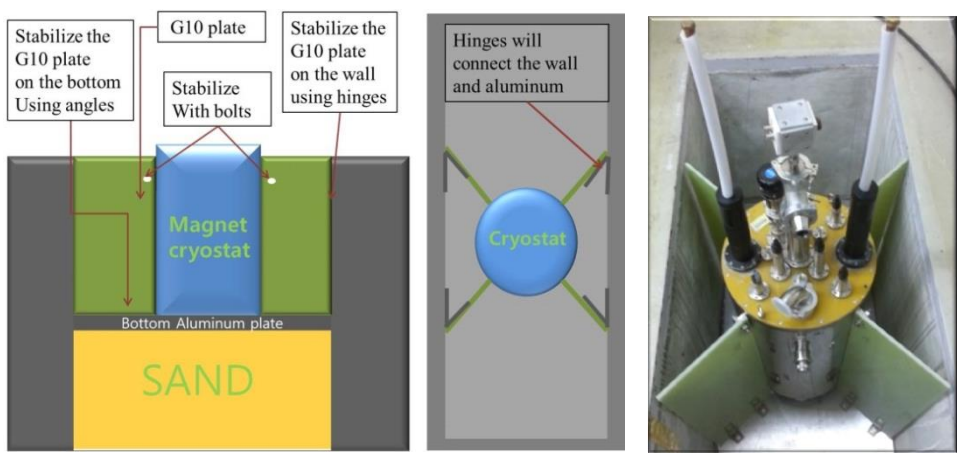


**Figure A.20** [left] The design of setting the $LN_2$/$^4$He cryostat, and [right] picture of the cryostat in the hole.

### ※ Connections for the $^4$He recovery

In order to save the expensive liquid helium, we have to recollect the helium gas and liquefy it. Proper connections to recovery line without leakage are essential for the successful recycling. Figure A.20 shows the way of connections from the $^4$He cryostat. When we cool down to 4.2 K with the liquid helium 4, the cryostat is over pressurized, thus we have to direct connect to the recovery line by opening the ball valve and close valve in $^4$He gas handling system (GHS). However, when we cool down to 1.5 K, we pump out the cryostat using the $^4$He GHS. In this time, we should close the ball valve and recover the helium gas from the outlet of the pump in $^4$He GHS. An additional relief valve is connected to the cryostat to prevent the overpressure. Here, using the bigger tube for the recovery is better, because the gas conductivity is sensitive to the inner radius of the tube. The gas conductivity is proportional to the $r^3$ for molecular flow ($<10^{-3}$ mbar) and to the $r^4$ for viscous flow ($>10^{-2}$ mbar) ($r$ = inner radius of the tube).

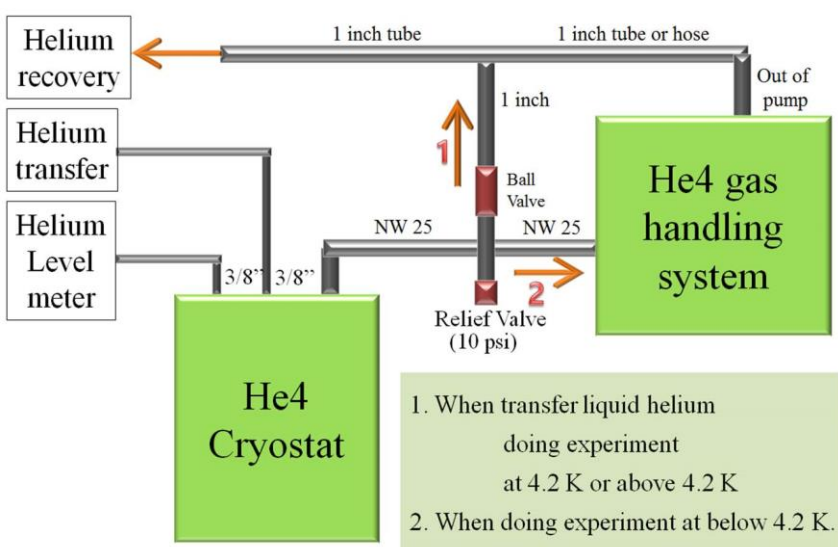


**Figure A.21** Schematic illustration of connections to the recovery line.

### A.3.2. Helium 3 cryostat

In order to cool down below 1 K, we need to use Helium 3($^3$He) gas. However, we should handle the $^3$He gas carefully so that we do not lose the gas since the $^3$He gas is extremely expensive (~$ 3000 per liter). Therefore we should make the cryostat without leak source. In addition, the cryostat should be well designed so that the $^3$He gas be liquefied and cooled down to ~0.4 K efficiently. The picture below shows the overall design of the $^3$He cryostat. On the head part, there are two NW25 fitting, one for inserting the probe and another one for pumping out the cryostat. For making the two connectors, 1-inch T-connector was welded also with long 1-inch tube. On the 1-inch tube, there should be a Wilson seal with NW40 fitting to connect to the $^4$He cryostat. On the tip part of 1-inch tube, thin tubes are connected. There are two thin parts, one is 1 K pot with 1 layer tube and another is 2 layers in which the intermediate area become vacuum at low temperature. 1 K pot is the place where the $^3$He is liquefied. (The detail how to handle the $^4$He and $^3$He is written in the gas handling system session)

An important part is the thin part of the cryostat. There are several Version of the cryostat we tried and will try according to how to make the thin part.

1) Version 1 – make the 2 layers part with G10.

- In this first try, we made the 2 layer part with G10. All parts between G10 and

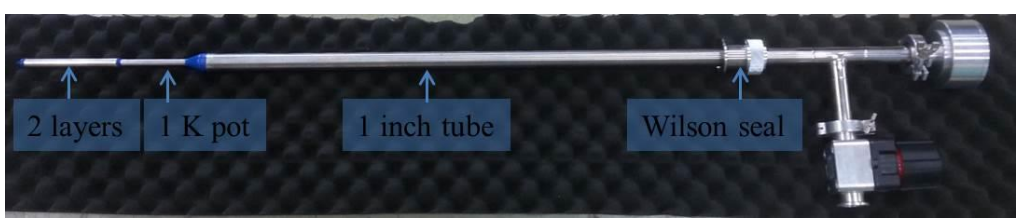


**Figure A.22** Picture of the Helium 3 cryostat (Version 2)

SUS were connected using t. he blue epoxy (Stycast 2850). We put the charcoal in the intermediate area of the two layers. This charcoal makes pressure in the intermediate area lower by absorbing the gas. Since absorption rate of the charcoal increases at low temperature, the charcoal acts as a cryogenic pump. One advantage of this Version is that the measurement will be free from the eddy current since G10 is insulating. Because the magnetic field changes drastically in the pulse magnet, it can generate eddy current that severely affect the measurement if the 2 layer parts are made of conducting metal. Another advantage is that the minimum temperature of liquid $^3$He will be lower because the sample space is thermally well separated from other parts of higher temperature. However, this Version makes us difficult to seal the cryostat. In our case, the vacuum situation was good at room temperature. However, after cooling down and warming up several times, it burst at the time of warming up. It was because there became leak at low temperature, thus the charcoal absorbed too much gas and also emitted too much gas when it was warmed up resulting in the high pressure at the intermediate area. The leakage at low temperature seems to be due to the different thermal shrinkage of the G10 and the blue Stycast. Therefore, it is really difficult to make it leak tight at low temperature. Another drawback of this version is that the sample space becomes too small ($d$ ~ 5 mm) because it is difficult to make the G10 tube very thin (~0.5 mm). In addition, we have to paint the whole G10 tube part with

**Figure A.23** The tip part of the helium3 cryostat of Version1 which consists of G10 and SUS tube.

blue Stycast since the G10 tube itself can be porous at low temperature. This makes the G10 tube thicker.

2) Version 2 – make the all tube with SUS.

In this second try, we made the all tube with SUS. In this case, changed all of the tube of $He^4$ and $He^3$ cryostat to the thin SUS tube(t ~ 0.5 mm). The SUS tube should be completely non-magnetic, however, we could not purchase nonmagnetic SUS tube with low thickness domestically. Thus we bought them from Japan(Yamamoto special steel)and USA (Oxford). In this case, we could enlarge the sample space to the diameter to ~8.4 mm. Because of the large sample space, we could also make the probe bigger. However, this version can generate eddy current because of higher conductivity of SUS. In our experiment of transport, with this version, we could not see clear evidence of eddy current. This version also had problem of cold leak between the G10 and SUS. The vacuum sealing was good at room temperature, but there became leakage at low temperature possibly due to different thermal shrinkage rate.

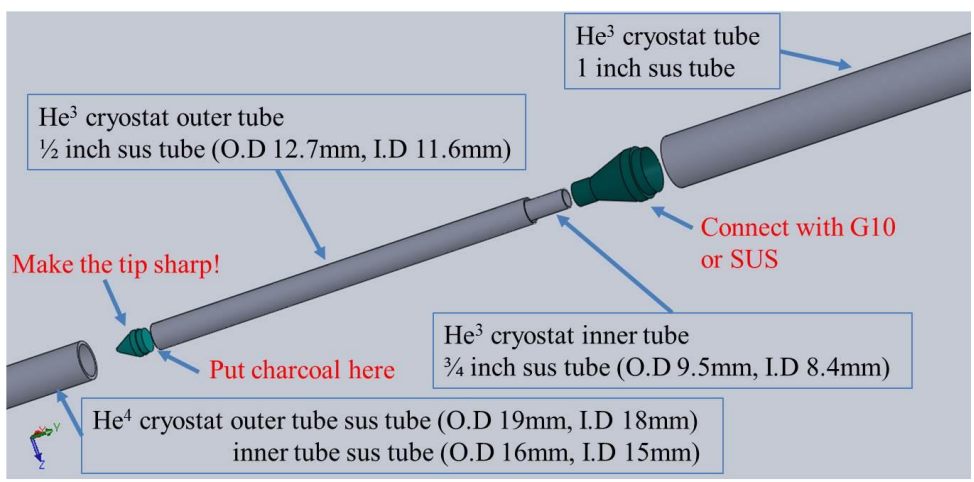


**Figure A.24** Design of the Helium 3 cryostat (Version 2)

3) Version 3 – make the all tube and joint with SUS

In this version, we changed the joint part to the SUS as well. This is for making the sealing perfect. We did silver welding for connecting the SUS parts. We use the silver welding because it can be done in laboratory and it does not make the SUS magnetic. TIG welding, another welding method, melt the SUS itself, thus make the SUS magnetic. In this version, the sealing is supposed to be perfect, even though the eddy current can affect the measurement.

**Figure A.25** Picture of the Helium 3 cryostat (Version 3)

4) Version 4 – make only the inner tube with G10.

In this version is to make the inner tube of tip part of $^{3}$He cryostat with G10. The G10 part is the most close to the sample space, thus the eddy current will be reduced. This version is also used in NHMFL in Los Alamos as well. However the joint between the SUS and G10 tube will be tricky. One of the solution is to make the SUS tube extremely thin (< 0.4mm) so that the SUS tube can stick well to the G10 tube regardless of the different thermal shrinkage. Another solution is to use special low temperature glue from Japan call '二トフィックス' for this place. In this version, we also need the thin G10 tube (~0.5mm) which is available from Japanese machine shop. This version will be tried in the future.

### A.3.3. Gas handling systems (GHS)

For investigation of the quantum phenomena in the condensed matter physics, it is crucial how low temperature we can cool down. The lowest temperature we can reach with conventional equipment is ~ 10 mK using dilution bridge which use the mixture of $^3$He and $^4$He. However, complicated gas handling and long time is necessary to cool down to such low temperature. Another, relatively easier, way is condensing the $^3$He to cool down to ~300 mK. The boiling point of $^4$He and $^3$He is 4.2 K and 3.2 K, respectively. However, we can cool down to lower temperature by pumping out the liquid helium according to the vaper pressure curve in Figure A.24. In this section, I deal with detailed design and construction of the $^4$He and $^3$He gas handling systems which is learned from that of NHMFL in USA.

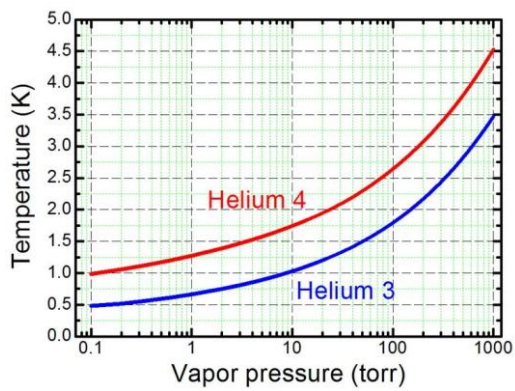


**Figure A.26** Vapor pressure of Helium

#### A.3.3.1. Helium 4 gas handling system

The function of the $He^4$ gas handling system is to control, maintain, and monitor the pressure of $He^4$ cryostat. It consists of pump and several valves and regulator between the cryostat and pump. Details of each parts are as below.

1) Pump. Low vacuum pump can be used. In NHMFL, big vacuum house is used but sometimes big rotary pump is also used. The pump should have high pump speed to reduce the base temperature. For example, we tried a rotary pump with 100 L/min, the helium temperature went down to 2 K, only. After that, we changed

the pump with >1000 L/min pump.

2) Ball valve (Swagelok SS-65TS16). Ball valve has the highest flow rate among the valves. Thus this valve is used to pump out rapidly down to base pressure and cool down to base pressure.

3) Niddle valve (Swagelok SS-18RS8). Niddle valve has small flow rate, only 5 % of ball valve in the system. Thus this valve is used to control the pressure, slowly. For example, if we want to stabilize the temperature at ~ 3.5 K, it is better to close ball valve and control with nibble valve.

4) Vacuum regulator (LJ engineering, 329H). Vacuum regulator is used to stabilize the pressure in vacuum. Especially, it is essential for the pulse field measurement. Since it cannot cover the whole pressure range, it should be used with other valves in parallel. There is a vent port in the vacuum regulator, thus we need to connect the helium gas to the port.

5) Plug valve (Swagelok, SS-8P6T). The plug valves are open only when the vacuum regulator is used. The plug valves are O-ring sealed and cheap.

6) Toggle valve (Swagelok, SS-1GS4). It is used to supply little amount of helium gas in short time. It is on/off valve with small gas conductivity.

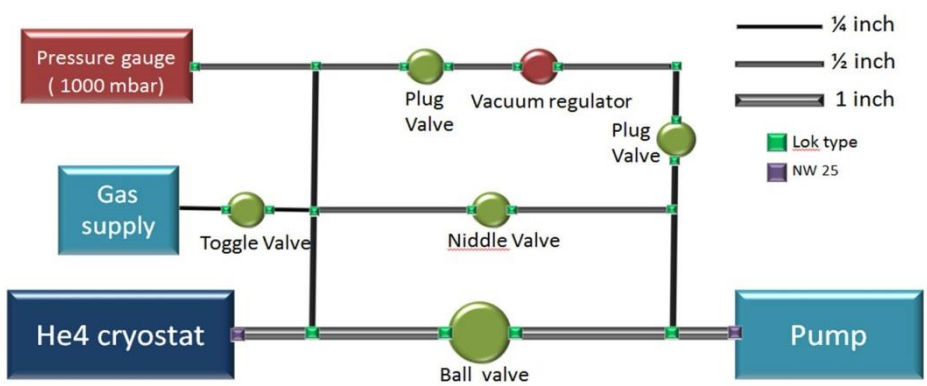


**Figure A.27** Schematic of Helium4 gas handing system**.**

7) Capacitance gauge (Atovac, ACM 200). We use the capacitance gauge for monitoring the pressure because the measurement of pressure of independent of the kinds of gas.

### A.3.3.2. Helium 3 gas handling system

The $^3$He gas handing system is used to input the $^3$He gas in to the $^3$He cryostat, condense the gas and pump back for controlling the temperature between 0.4 K ~ 1.5 K. We can use this system to input and pump out the $^4$He gas as well. First, here I explain the principle of operation. Before using $^3$He gas, we can control the $^4$He gas using $^4$He gas supply and roughing pump with valves (1)~(3). When we start to use the $^3$He gas, the $^4$He gas in the $^3$He cryostat is completely pumped out with the roughing pump. Then, we can input the $^3$He gas by opening the valves (4) and (5). In order to liquefy the $^3$He, the temperature of liquid $^4$He in the $^4$He cryostat should be less than 3.2 K. If the $^3$He is liquefied, we can cool down to ~0.4 K by pumping out through the sealed pump and by opening the valves (6)~(8). The check valve (9) is for safety. The pumping power and the temperature between 0.4 K and 1.5 K can be controlled by whether we use the valve (6) or (7) and how much we open the value (6). When we finish the $^3$He experiment by pumping up the $^3$He gas to the $^3$He dump, we should turn off the sealed pump and open shortly the ball valve (10) to prevent the oil back flow.

I list below some details of important parts in the $^3$He gas handling system.

1) Sealed Pump (Hermatic sealed pump, Adixen 2005-H1). In order to minimize the loss He3 gas, sealing of the pump also should be perfect. The hermatic sealed pump from Adixen is sealed with 5 o-ring-like sealing parts (2 parts in normal

pump) and also oil part to seal. We should supply the oil for both pumping and sealing separately.

2) Bellows valves (Swagelok 6LV-BNBW4, SS-4BK-TW). The bellows valves contain metal bellows that completely separate between inside and outside of the valves. Model 6LV-BNBW4 is 90 degree open and close type, thus used for simple on and off. Model SS-4BK-TW is niddle valve type, thus the flow can be specifically controlled.

3) Speed valve (Edward, SP25). Edwards SP Speed valve are diaphragm sealed in-line, isolation valves. The construction consists essentially of a flexible elastomeric diaphragm which is sealed onto a lightly polished seat by a screw thread mechanism. The mechanism is isolated from the system by the diaphragm.

4) $^{3}$He dump. The most important requirement of $^{3}$He dump is of course containability without leak. We prepared the hydrogen dump of 10 L for containing the $^{3}$He.

5) Pressure gauge for $^{3}$He dump (Panel gauge, Swagelok, PBG-63-AC0-AQ). This gauge is for monitoring the remaining amount of $^{3}$He gas in the $^{3}$He dump.

6) Pressure gauge for $^{3}$He cryostat (Capacitance gauge, Atovac, ACM 200) We use the capacitance gauge same as the gauge in $^{4}$He system, however, we use two gauges of different range, 1000 mbar and 100 mbar.

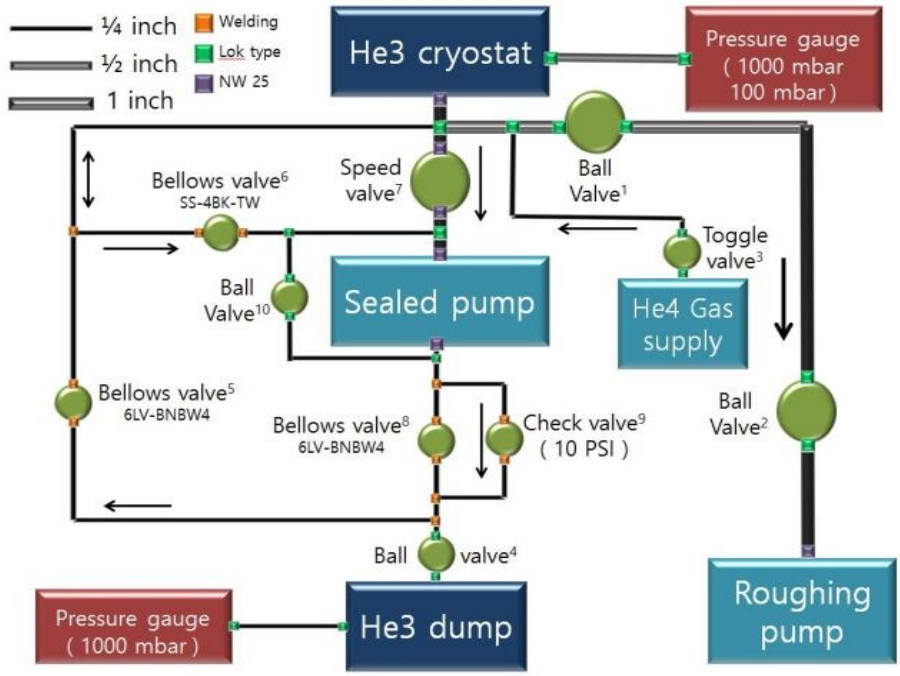


**Figure A.28** Schematic of Helium 3 gas handing system

**Figure A.29** Picture of rear panel (left) and front panel (right) of the gas handling systems (GHS). The upper part is $^{4}$He GHS and lower part is $^{3}$He GHS.

## A.4. Measurements systems in the pulsed field

### A.4.1. Transport probe

For measurements of physical properties, careful design and manufacture of probe are necessary. Especially since high frequency (<100 kHz) measurements are inevitable in the pulse magnet experiment, we should more careful to avoid the electrical loop and eddy current. In this section, we show the design and picture of each part of the transport probe.

(1) Head part

There are connectors made in the head part of probe are thermometer (4 pin, LEMO), heater (2 pin, LEMO), pick up coil (2 pin, LEMO), and connectors for measurement (6 pin, SMA). The LEMO and SMA connectors and cables are usually used in the pulse magnet experiment, for reducing the current loop and minimizing the noisy. Because the two or four core wires are assembled and sealed together in LEMO, the noisy from electric loop can be minimized. This head part is

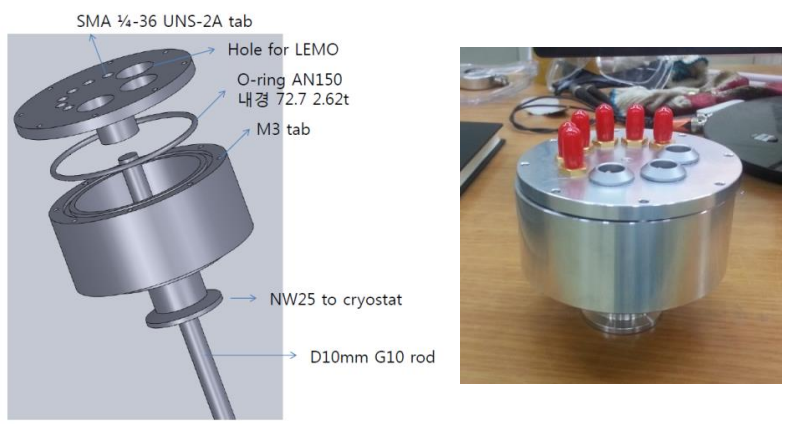


**Figure A.30** Design (left) and picture (right) of the head part of the transport probe transport probe. (Designed and made by Dr. S. Khim).

made of duralumin which is light and strong. The cap and body parts are sealed by the O-ring using the M3 tabs. The cap part is connected by G10 rod directly, or by 3/8 inch SUS tube which is again connected by G10 rod (actual probe was made by the later method). The bottom of head part is NW 25 connector to put the probe inside the $^3$He cryostat.

(2) Probe part

The probe part is made of G10 which is insulator and has small thermal extension. We used the G10 rod with diameter of 8 mm. We made the G10 rod flat in both side to put the wires straightly. The heater, pick up coil, thermometer and 4-probe contacts are connected with twisted phosphor bronze (PB) wires and two micro-coaxial wires are connected is polarization/dielectric constant measurement. The wires are stick on the flat sides of the G10 rod with the GE varnish. (It is better to further shield the wires with thin SUS tubes later). Since the resistivity of phosphor bronze at room temperature is ~6.5 times larger than that of copper, the PB wires are usually used in the low temperature experiment for thermally separating between probe part and head part. The heater is wound with the Ni-Cu wire above the sample space and covered by the blue epoxy (Stycast 2850) to prevent the electrical short. The sample space is made of a big piece of sapphire which has high thermal conductivity and low electrical conductivity. In order to monitor the exact sample temperature, we put the Cernox thermometer just beneath the sapphire. We cut a groove for the path of pick up coil on the tip part and side of the G10 rod. We wound the pick-up coil 5 times with the copper wire, to read the magnetic field change. The vary tip part is made sharp so that the probe goes into the $^3$He cryostat smoothly without blocking.

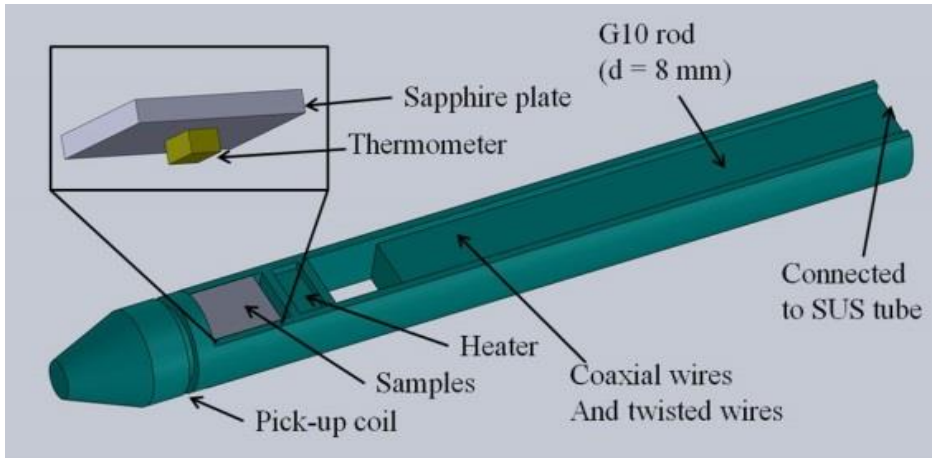


**Figure A. 31** Design of probe part of the transport probe

**Figure A.32** Pictures of the probe part of the transport probe

### A.4.2. Digitizer

Digitizer is one of the essential devices for the pulsed magnet experiment. Since the measurement is done in short time, the sample rate should be high. We chose the digitizer from Spectrum (M2i, 4932). Here I list the required spec and spec of M2i, 4932 digitizer for the pulsed magnet.

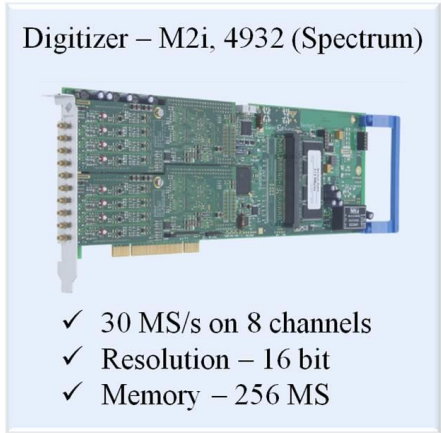


**Figure A.33** Picture and spec of digitizer

(1) Sample rate – how many data taking in one second → 30 MS/s

- Assuming the rising time of field is 5 ms, 50 kS can be measured.

(2) Resolution – how the resolution is high → 16 bit

- $2^{16}$ = 65536, if range is 10 V, resolution = 10/65536 = 150 μV

(3) The number of channels → 8 channels

- One for pick up coil, two for transport, one for polarization,
  One for dielectric constant…

(4) On board memory – data acquisition x sample rate → 256 MS

(5) Band width, triggering…

※Oscilloscope vs Digitizer

- Oscilloscope and digitizer have fundamentally same function to measure the waveform of the signal. However, they have several differences on their usage. Oscilloscope is used for high speed and low resolution measurement often with its own display. Digitizer is computer based device, thus data acquisition and process

can be done with software. Much more channels then that of oscilloscope is available and synchronization with other instruments is also possible. In addition, while the most oscilloscopes have limited resolution of 8 bit, much higher resolution ~24 bit is available in the digitizers.

### A.4.3. Software for measurements

The digitizer manufacturer Spectrum offers convenient Labview program for measurement. Thus, based on the Labview sample programs, I made the program for pulsed field measurement.

(1) Setting for measurement

- loop – continuous measurement whenever the triggering is done.
- single – one time measurement when triggering is done.
- stop – stop the measurement. -force – force the triggering.
- Mem – sampling number of the measurement
- Post – sampling number after the triggering
- Sampling rate – usually done with > 1000 kHz
- Triggering setting – triggering is done by the rising signal of the pick-up coil signal.
- Channel setting – set the signal range (200 mV, 500 mV, 1 V, 2 V, 5 V and 10 V) and offset.

(2) Display of the signals.

- Pick up coil signal – directly measured from the pick-up coil of the probe, conventionally use the channel 0.

- Field curve – calculated by integrating the pick-up coil signal. If the field value does not converge to zero after the shot, we can adjust offset of the pick-up coil signal.

- Displays for measurement – Figure A.33 shows the data of X and Y from the SR830 lock in amplifier which use the channel 1 and 2. We can add more measurements using other channels.

※ The picture of Labview program in Figure A.33 shows the data of magneto-resistance of YBCO single crystal for magnetic field direction *H*//c up to *H*~30 T at 91 K. The channel 1 shows the in-phase signal which shows breaking of superconductivity at low field. The channel 2 shows the out of phase signal which is not changing and demonstrating the reliability of the measurement.

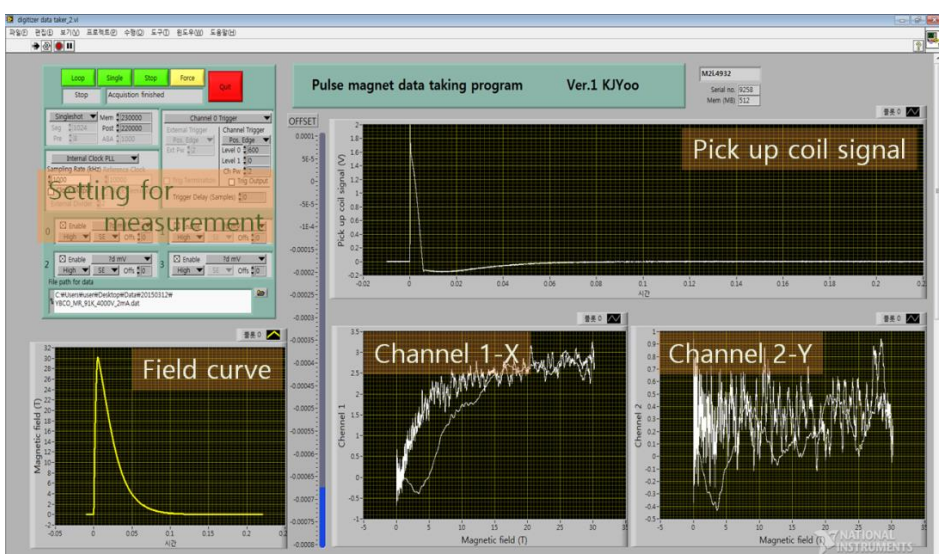


**Figure A.34** Picture of labview program for the pulsed field

### A.4.4. Ground connection

For a couple of reasons, it is very important to connect the ground properly. First, since the pulse magnet system generates very high current, we should make sure that the system does not affect sensitive experiment in other laboratories. Second, the high frequency measurements in pulsed field are generally more apt to be affected by various sources of noisy than that of static measurements. In our system, we separated the ground of pulsed field generating system and measurement system. The ground of pulse magnet system is connected to a dirty ground which is connected to out of building. Meanwhile, the ground of electronics for measurements is connected to a clean ground. For this very purpose, we made a first class ground digging out a field around 2 meter deep. The power cable comes from the building for running the electronics, but ground is separated from both of magnet system and measurement system.

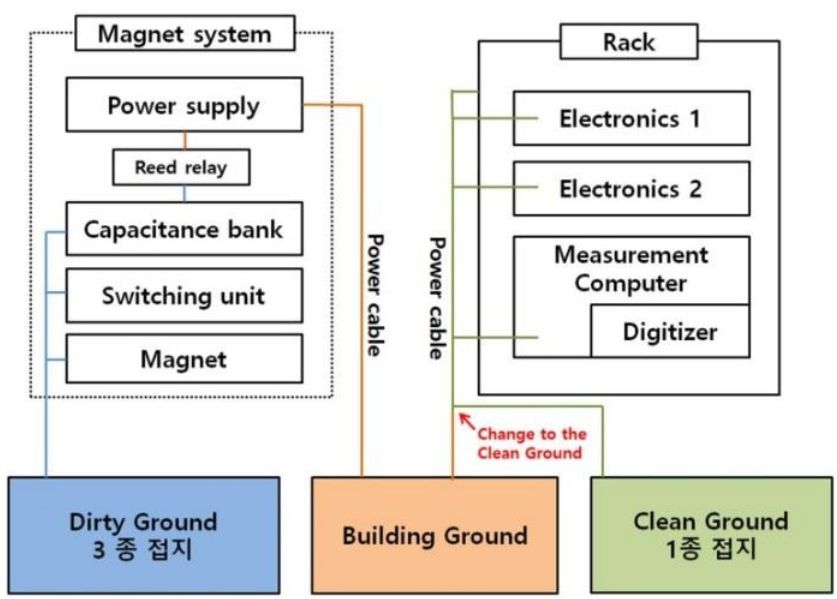


**Figure A.35** Diagram of the ground connections.

### A.4.5. Preparation for the electric resistivity measurement

There are a couple of methods to measure resistivity in the pulsed field, conventional four-probe measurement and contactless measurement using tunnel diode oscillator (TDO) or proximity detector oscillator (PDO). In this section, we mainly explain how to use the four-probe method in pulsed field comparing that in the static field.

- Sample dimension – According to the resistivity of the sample, it is better to shape the sample to realize appropriate resistance. For example, superconductor samples normally has low resistivity (~μΩcm), thus we would better make it thin and long rod shape. This is because the resolution of resistance measurement in pulsed field with high frequency (>100 kHz) is lower (~ 10 mΩ) than that of the static field.

- Four probe contacts – Since this is high frequency measurement, the effect of small capacitance ($C$) and inductance ($L$) components on the contact become not negligible. Therefore the out of phase in the ac lock-in measurement which does not represent intrinsic resistance becomes significant. In order to minimize the $C$ and $L$ components, we should make the contact resistance small (few ohms) so that the out of phase component is few degrees. The silver paste contact is usually better for making contact resistance lower than the silver epoxy contact. For the current contact, the silver epoxy/paste should be applied on the whole side of the sample, and it is better to make the distance between the voltage contacts long for making the voltage signal bigger.

- Wire arrangement – It is important to minimize loop made by the wires, since it can make the huge noise due to the fast field change. For this, the wire should be

twisted from near the sample contacts. In addition, the wires should be firmly fixed on the probe so that the wires do not vibrate in the fast field change. N-grease which solidifies at low temperature or GE varnish can be used for this purpose.

- Electronics – We use lock-in amplifier which is affordable for high frequency (>100 kHz). We used the lock-in amplifier SR 830 which is conventionally used for static field measurement in the lab. And the signal from the SR 830 is read by the digitizer, from the output slot of the SR 830.

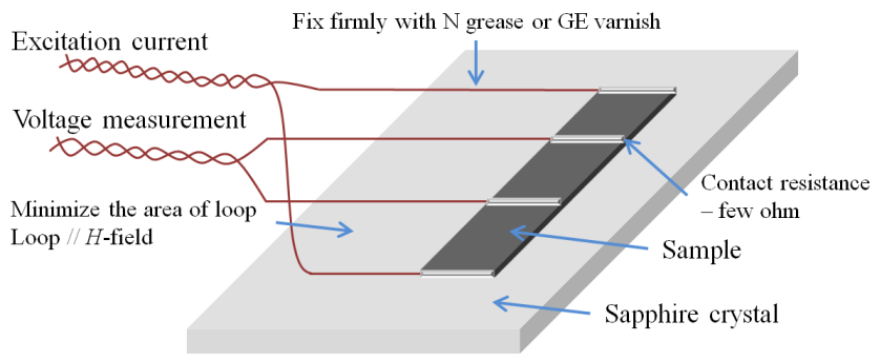


**Figure A.36** Preparation scheme for the four probe measurement in the pulsed field

## A.5 Experiment procedure in the Pulse magnet

In this section A.5, we state details of sequence of the pulsed field experiment. It includes whole progress of preparation, measurement.

### A.5.1. Preparation for the experiment.

There are several prerequisite things to do before the experiment. We should check the list before each experiment.

1) **Pump out the vacuum layers in the cryostat.** The vacuum layers in the cryostat should be pumped out down to $10^{-7}$ mbar order with turbo molecular pump.
2) **Clean up the parts of pulse magnet system.** The small dust can be source of electric shock because high voltage (more than 1000V) is used in the experiment.
3) **Check that all of the connections of pulse field generation circuit** are properly done. Each connection should be tightly connected so that the contact resistivity is minimized.
4) **Check that all of the gas control components are connected properly.** Especially, leak test of gas handling systems and helium recovery line should be completely done.
5) **Check that the fire extinguisher is available.** Confirm the existence and place and remaining, and sufficient contents in it.
6) **Measure the inductance of magnet with LCR meter.** This is one simple way to monitor the condition of the pulse magnet.

## A.5.2. Setup of the probe and cryostats.

**1) Prepare the probe for measurement.**

Prepare the samples and check the connections of sample, thermometer, pick-up coil and heater and put the probe in to the helium 3 cryostat.

**2) Pump out the Helium 3 cryostat**

After putting the prepared probe inside the $^3$He cryostat, we pump out the $^3$He cryostat before cooling down. Turbo pump is usually used to vacuumize down to ~$10^{-5}$ mbar. Otherwise, air inside will become ice and affect the measurement.

**3) Insert the Helium 3 cryostat into the Helium 4 cryostat**

The time to insert the $^3$He cryostat is depends on the situation. It can be inserted before transfer the $LN_2$ and also after the transfer of the liquid $^4$He. In the latter case, the pressure of the $^4$He cryostat should be larger than the atmosphere pressure before opening it. It is better to insert the $^3$He cryostat slowly to minimize the evaporation of the liquid $^4$He.

## A. 5.3. Magnet test

Before each measurement, we should check whether the pulse generation circuit and magnet is working without problem. Here I list the sequence of the test.

1) **Supply liquid nitrogen ($LN_2$).** During the pulse magnet experiment, the magnet should be cooled down in the liquid nitrogen. Before first discharge to the magnet should be in the $LN_2$ at least for 2 hours.

2) **Turn on the power supply, control circuit, and computer for control circuit.**

3) **Check that the ground switch relay is working well.** This is important check, because it becomes dangerous if it does not work when high voltage of charged in the Cap bank. First, close the ground switch relay with Labview program and check that relay is electrically shorted. Second, open the ground switch relay and measure the resistance between terminals before and after the relay. It should be same as the ground resistor, ~ 900 Ω.

4) **Check that the reed relay is working well.** First, close the ground switch relay with Labview program and check whether the terminals before and after the relay is electrically shorted. (The relays of high voltage and ground line are controlled together). Second, open the ground switch relay and measure the resistance between terminals before and after the relay. It should be same be insulating (We should check the ground line after disconnecting the connections)

5) **Check the function of SCR triggering.** Press the SCR until the resistance between gate and cathode becomes ~5 Ω. We should be careful not to press too much, otherwise, it can be broken.

6) **Check the laser generator makes sufficiently strong laser.** If it is too weak, change the battery.

7) **Connect the laser to the triggering circuit and measure the voltage change on the triggering by the laser.** The triggering voltage should be

monitored by oscilloscope or digitizer, since it will be applied only for several milliseconds, which is sufficient to trigger the SCR. If ~2 V is applied by the laser triggering, it is working well. Voltage of battery in the triggering circuit should be sufficient (larger than 5 V), otherwise, change the battery.

8) **Wear the high voltage insulation glove and insulation boots.** A person who control and get close to the pulse generating system should wear the high voltage insulation glove and insulation boots. In addition, we should touch any high voltage parts even with the insulating glove and boots, after confirming the complete discharge with ground stick.

9) **Charge the capacitor bank.**

- Open the reed relay and ground connection relay.
- Turn on the high voltage power supply and turn on the 'remote' tap in the software. (It will be turned on only after the remote tap is on)
- Wait for 10-20 minutes to stabilize the power supply.
- Close the reed relay.
- Enter the setting voltage. The entering value is 2000 times smaller than the actual applying voltage. For example, if we enter the value 0.25, then 500 V would be applied. We should not charge to the desired voltage at once. We should stabilize the charged voltage (monitored by the panel meter on the control circuit) and charging current at each step of 200 V. This is for preventing the charging current goes above 500 mA, when current is larger than 500 mA, the power supply will sound and can be damaged. During the capacitor bank is charged, we should sound a siren so that no one come close.

10) **Discharge the capacitor bank to the ground**

- After we charge the capacitor bank, there are two ways to discharge it. One is discharging to the ground and the other is discharging to magnet generating pulsed field.

- Close the ground connection relay, then it will be discharged to the ground. The time constant of the discharging curve will be RC = 900 Ω · 8.3 mF = 7.47 seconds.

11) **Discharge the capacitor bank to the magnet.**

- Set the probe with pick-up coil in the magnet and connect the probe to the digitizer.

- Turn on the Labview program for measurement and enter the setting values.

- Be ready for the triggering by clicking the 'single'.

- Trigger the SCR by turning on the laser. If the triggering is done without problem, the field curve will be taken as in the Figure A.6.

12) **Adjust the probe to the center of the magnet.** Repeat the pulse shot with 1000 V changing the position of probe and adjust the position that shows the highest magnetic field, in which the pick-up coil places in the magnet center.

### A.5.4. Cool down the sample

- After magnet test is done successfully, we have to set the temperature for measurement, which is usually low temperature. In this section, we explain how to prepare the cryostat, cool down to 0.4 K safely and effectively.

**1) Supply the liquid helium 4**

Prepare several things below before supplying the liquid helium in the cryostat.

- Make sure that the pressure of the $^4$He cryostat is higher than the pressure of atmosphere or the air will go in and ruin the experiment. If the cryostat is in low pressure, supply the helium gas.
- Turn off the pump or close all valves in the $^4$He GHS.
- Connect the level meter to the cryostat. But do not turn on the level meter until the level meter probe works properly at the liquid $^4$He temperature.
- Wear the goggle for safely.

If the preparation is done we can transfer liquid $^4$He with following procedures.

- Insert the tip part of the transfer tube in the $^4$He Dewar and insert deeper slowly. Then the helium gas will come out of another tip of the transfer tube. If the $^4$He cryostat is empty, connect the tube to the cryostat right after the helium gas comes out. But if there is some liquid helium in the cryostat already, insert to the Dewar more until the liquid comes out and quickly connect to the cryostat. If the tube is connected just after gas comes out, the ‘warm’ gas will goes in and evaporate the already existing liquid helium. After inserting the transfer tube, the helium recovery valve should be opened soon.
- Monitor whether the helium is being transferred properly. If the transfer is too slow or not transferred insert the $^4$He gas into the helium Dewar and pressurize the Dewar. We should not over-pressurize the Dewar, or the transfer will be too fast and the helium in the cryostat will be blow out. Slower transfer is better.
- When the transfer is almost done (if the level gauge indicate ~90%), quickly

take out the transfer tube from the Dewar and $^4$He cryostat. If we do not take out soon after the cryostat is full, the liquid $^4$He will start to evaporate fast.

**5) Cool down to the 4 K**

After we transfer the $^4$He, the temperature will not go down quickly because the $^3$He cryostat is in vacuum. Thus the $^4$He gas should be inserted as an exchange gas after purging the bellouse connected to the $^3$He cryostat 3 times. Usually, the exchange gas of ~5 Torr is the most appropriate since too much exchange gas can be liquefied which can make the measurement unstable.

**6) Cool down to 1.4 K**

We can control the temperature between 1.4 K and 4.2 K, by controlling the pressure inside the $^4$He cryostat with the $^4$He GHS. First we should close the valve of the $^4$He recovery line, and turn on the pump of $^4$He GHS and adjust the pressure with the ball valve, niddle valve, and the vacuum regulator. The liquid $^4$He becomes superfluid at 2.172 K, the so-called λ-point of $^4$He. In the superfluid state, the $^4$He has zero viscosity and it becomes very difficult to warm up again. Therefore it is better to finish all the measurements at higher temperatures before cooling down to the superfluid state.

**7) Cool down to 0.4 K**

The $^3$He is used to cool down to 0.4 K. Only well-trained people should control the $^3$He following the sequence below, since its price is high.

- The $^4$He in the $^3$He cryostat should be pumped out completely with the roughing pump in the gas handling system, and with heating it up to 30 K.
- Close the valve of the roughing pump in the $^3$He GHS. This valve must be

closed during the $^3$He experiments to prevent pumping the $^3$He out by mistake.

- Write down the pressure in the $^3$He gauge, which should be always smaller than the atmosphere pressure so that we don't lose the $^3$He.
- Open the valve of the $^3$He dump and insert the $^3$He gas into the $^3$He cryostat. And if the $^3$He is liquefied, pump out the $^3$He cryostat so that cooled down to 0.4 K.
- When we finish using the $^3$He, we should pump back the $^3$He dump completely with warming up to ~30 K. After that, close all of the valves of dump and GHS and check the pressure of the dump which should became almost same with that before using the $^3$He gas. It is natural that the pressure in the $^3$He dump will increase slowly as we repeat the experiment many times, because other gases such as $^3$He is pumped back together with $^3$He gas.

### A.5.5. Measurement and finish the experiment

After the magnet test is done without problem, we check the setting of probe and electronics for measurement and connect the output signal to the digitizer. Then, we set the temperature at which we want to measure and stabilize for ~ 5 minutes before repeat the sequence A5.2 9) and 11) to measure the magnetic field dependence of physical properties. We should ~1 hour after the maximum field (30 T) measurement in order to cool down the magnet.

After all of the required measurements, completely pumped out the $^3$He cryostat and make the pressure of $^4$He cryostat higher than that of atmosphere before disconnecting the bellows lines of the helium cryostat and take out.

## A.6. Preliminary measurement results

### A.6.1. Upper critical field of the YBCO single crystal

We first measured the resistance of the YBCO single crystal to measure the upper critical field ($H_{c2}$). Because the critical temperature is high (~92 K) and the $H_{c2}$ at the liquid helium temperature is too high (over 100 T), we could measure $H_{c2}$ using liquid nitrogen. We made 4 probe contacts with silver paste on a big single crystal with length of ~ 4 mm and checked that the contact resistance is several ohms, which is appropriate to the pulsed field experiment (the picture contact is shown in the transport probe section). The measurement is done with SR830 lock-in amplifier with 100 kHz. The pulsed field is applied along the c-direction since the $H_{c2}$ along that direction is lower than that of the other.

The resistance data of zero-field shows the critical temperature as 91.5 K. When we applied the pulsed field at 91 K, the superconductivity completely destroyed at 5 T, while the resistance gradually increases up to 30 T at 89 K. This data is taken during the field is decreasing. The phase diagram was drawn with the fields that the resistance deviates from zero at several temperatures. It roughly agrees the reported phase diagram. When we repeat the measurement with changing the charging voltage of the capacitor bank, the magneto-resistance data was reproduced, which supports the reliability of the data. In addition, we also compared the data of rising field and falling field. The rising field data does not follow the trajectory of destruction of superconductivity. This is possibly because the eddy current flow or sample moves, due to the high field change rate. From this measurement, we confirmed that we can take reliable data of magnetoresistance even though the data is noisy due to the low resistivity of YBCO.

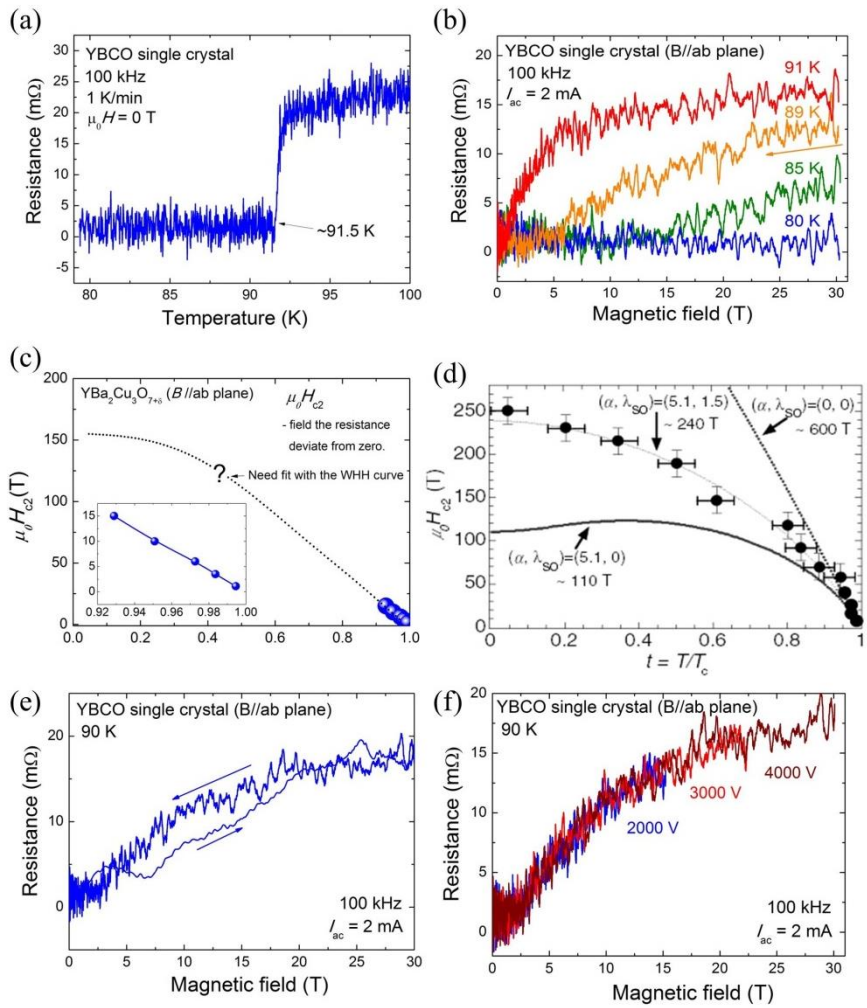


**Figure A.37** (a) Temperature and (b) magnetic field dependence of resistance of YBCO single crystal for *H*//c at selected teamperatures. (c)Upper critical field data of the YBCO single crystal compared with (d) reference data [2]. Magnetoresistance curve (e) comparing rising and falling field and (f) with different charging voltage in the YBCO single crystal

### A.6.2. Upper critical field of the $Nb_2Pd_{1.3}Se_5$ single crystal

As a test experiment at the liquid helium 4 temperatures, we measured magnetoresistance of the $Nb_2Pd_{1.3}Se_5$ single crystal. We made contacts of several pieces of the sample and chose a best piece by measuring the temperature-dependent resistance in the PPMS. The measurement was done by the same method as that of YBCO with the driving current of only 10 μA applying field along c-direction.

Since the sample has thin needle shape, the resistance above the critical temperature (onset ~ 5 K) is relatively high resistance (~40 Ω). The superconducting transition is not sharp and stays nonzero until 4 K. We took magnetoresistance data at several temperatures between 2 K and 5 K. The superconductivity is destroyed at higher field at decreasing the temperature. However, the increasing curve of the magnetoresistance is too broad compared to other reports on $H_{c2}$. We draw phase diagram from the magnetic field showing 10 %, 50 %, and 90 % of normal phase. The measured $H_{c2}$ at 2 K is much smaller (~7.5 T) than the reported $H_{c2}$ (~14 T) which is from 50 % of normal resistivity value.

By the way, the temperature want down to only 2 K when we pump out the helium 4, while it normally goes down to 1.4 K. There were a couple of possible reasons for this. First, the pumping power of the pump we used (Adixen 2005-H1, 5.4 $m^3$/h, 90 l/min) is not enough, thus we bought a big pump (Kodivac 1300K, 1300 l/min). Second, the vacuum level of the cryostat is not good; turbo pump can pump out only down to 10E-2 mbar level. We have to the leak problem as well.

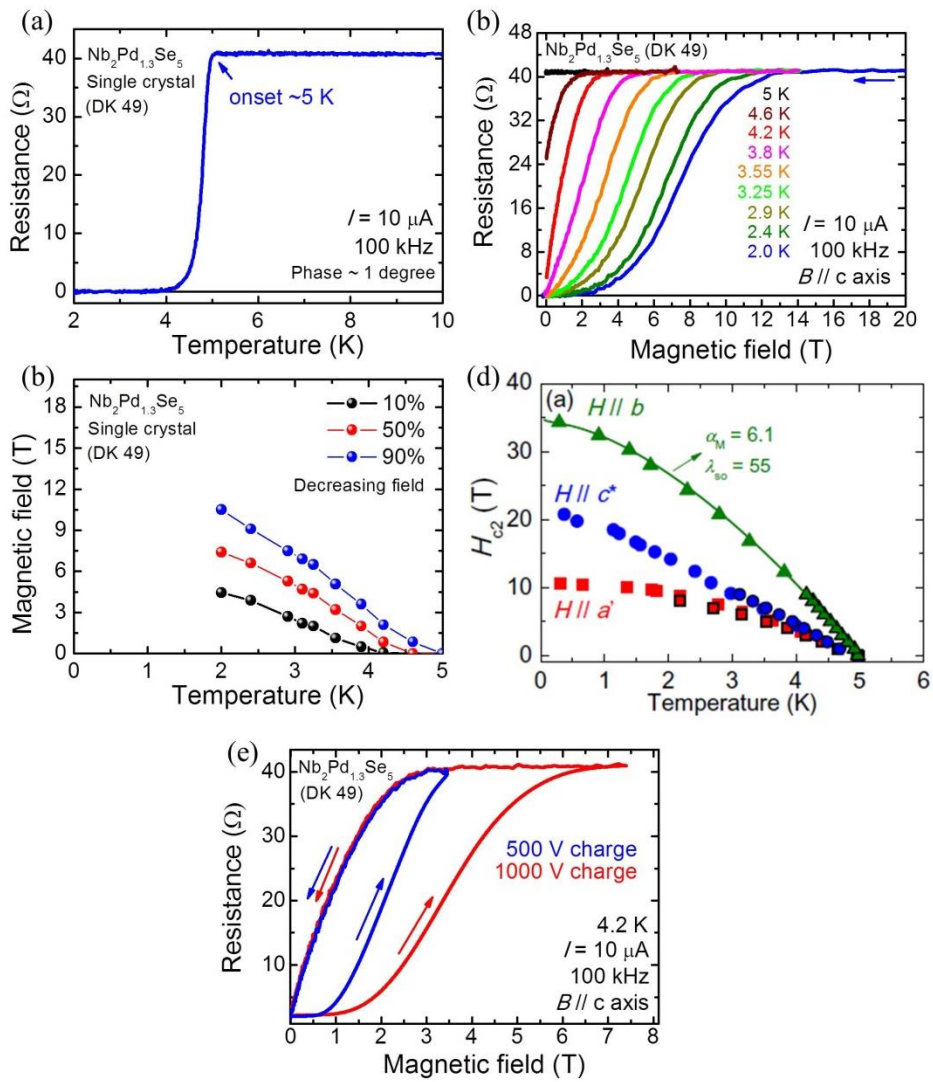


**Figure A.38** (a) Temperature and (b) magnetic field dependence of resistance of $Nb_2Pd_{1.3}Se_5$ single crystal for *H*//c at selected temperatures. (c)Upper critical field data of the $Nb_2Pd_{1.3}Se_5$ single crystal compared with (d) reference data [3]. (e) Magnetoresistance curve with different charging voltage.

Another problem in this measurement we found is that the data of rising field and falling field is completely different. At least the falling field data is reproducible in the various charging voltage in the cap bank, thus draw $H_{c2}$ from the falling field data. However, the rising field data strongly depends on the charging voltage. We considered several possible reasons. One is eddy current due to the fast field variation. The eddy current increases the sample temperature and break the superconductivity in lower field. However, in our result, the superconductivity breaks in higher field, when we apply higher maximum field. Thus, we could not still find reasonable analysis on the error of the measurement.

## A.7 Maintenance of the Pulse magnet system

In order to operate the pulse magnet system safely for a long time, we need to inspect the system regularly. In this chapter, we explain how to do the maintenance.

### A.7.1. Pulse magnet

The pulse magnet has lifetime according to how frequently and how much field is generated by the magnet. Since the pulse magnet receive high Lorentz force during the application of magnetic field, the magnet coil slowly and slightly changes at the experiments. When we use the magnet long time, there will be defect which causes explosion of the magnet. The explosion not only makes huge sound, but also mechanically damages the cryostats. Therefore, it is better to predict and prevent the explosion by monitoring the magnet before and after each measurement.

#### A.7.1.1. Monitor the inductance of the magnet

As the degradation of the pulse magnet changes, the inductance of the magnet changes. According to the advice of prof. Zang, the 5% change of the inductance indicates the lifetime of pulse magnet. The change of the inductance ($L$) so far is as below.

2015. 03. 12 $L$ = 1.31 mH

2015. 03. 38 $L$ = 1.319 mH

#### A.7.1.2. Monitor the curve of current on the magnet

As we measure the change of k'applied' magnetic field using the pick-up coil in the probe, we can measure the current in the coil with 'applying' magnetic field. Here I introduce a couple of ways to measure the high current, current transformer and Rogoskii coil. Both consist of toroidal coil which detect the high current-induced magnetic field. The former measures the current from the coil and the later measures the voltage. Thus, during each measurement, we can monitor the current curve on the magnet coil and diagnose what is happening in the magnet. The NHMFL in the Los Alamos is already monitoring the magnet current, thus we also need to install this monitoring system.

### A.7.2. Switching unit

#### A.7.2.1. Cleaning the copper plates (once in several months)

In order to realize high field safely, conduction of all connections in the system should be maximized. However, the copper plate naturally oxidized as time passes for several months. The sequence for the cleaning is as below.

- Make sure the capacitor bank is discharged completely and disconnect all the

connections to the switching unit.

- Disassembly the copper plates and high voltage devices following the sequence shown below.

① → SCR → ② → ③ → Diode 2 → ④ → Diode 1 → ⑤ → ⑥ → ⑦

- Dilute the sulfuric acid with water by ratio of 1 : 10 after wearing the Nitrile glove.

- Clean the copper plates with the diluted acid and wash them with water soon. Here, we should completely wash them with water otherwise there will become stains on the plates. Then, dry the surface of the plates with dry papers.

- Install the copper plates and devices (SCR and diodes) following the reverse sequence of the disassembly. Here, take care that the direction of the anode and cathode of the device is correct. In addition, the contacts between devices and copper plates must be uniform, otherwise the device can be broken when the high voltage is applied.

- Connect all necessary cables to the switching unit.

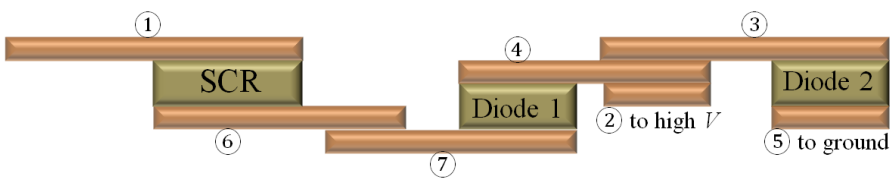


**Figure A.39** Schematic of positions of the copper plates and high voltage devices

### A.7.3. Gas handling systems

#### A.7.3.1. Monitor the amount of helium 3 gas

- After each experiment, we should write down the remaining amount of helium 3 gas in the helium 3 dump and monitor the gas. And we can estimate the purity and loss of the gas.

#### A.7.3.2. Recharge the helium 3 gas

- As we repeat the pulse magnet experiment, the amount of $^3$He gas changes. If the impurity gas is added, amount will increase. And if the $^3$He gas flows out of the GHS, the amount will decrease. If the amount of pure $^3$He gas is not enough, we have to recharge it following the sequence below. First, connect the dumps and pump like the Figure A.40. Second, open Valve 3 and pump out the tube and close the valve. Third, fill up the tube by opening the Valve 2 and close the valve. Forth, input the gas in the tube to the dump in GHS by opening the Valve 1 and close. Fifth, check how much $^3$He is recharge and repeat the third and the forth sequence until it is sufficient.

#### A.7.3.3. Maintenance of the rotary pumps (once in several months)

- We should monitor the oil level of the rotary pumps before experiment and refill, if it is empty.

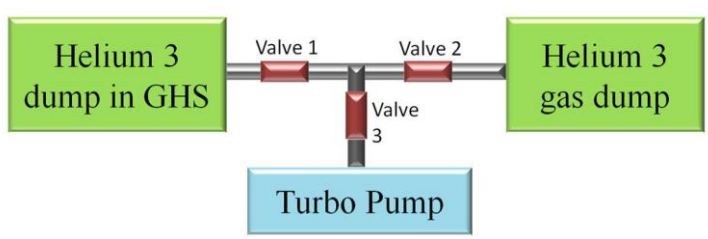


**Figure A.39** Schematic of the connections for the $^3$He gas

- We should check the condition of the oil trap filter and if it is filter capacity of full, change it to new one.

## A.8 References


[1] K. Son *et al.,* New Physics: Sae Mulli **64,** 638 (2014).

[2] T. Sekitani *et al.,* New Journal of Physics **9,** 47 (2007).

[3] S. Khim *et al.,* New Journal of Physics **15,** 123031 (2013).

# 국문 초록

자기전기 효과란, 자기장에 의해 전기 분극이 혹은 전기장에 의해 자율이 변화되는 현상을 말한다. 2000년대 초반부터 자기전기 효과는 스핀에 의한 강유전성의 기저 물리 대한 관심과 저 에너지 전자소자로의 높은 응용가능성으로 인해, 많은 관심을 받아왔다. 따라서, 수 천편의 폭넓은 실험 결과들과 이론적인 모델관련 논문들이 발간되어, 자기전기 효과에 대한 이해가 정립되어 왔다. 하지만, 나노 사이즈의 입자와, 높은 양자효과가 기대되는 스핀 $S$=1/2 시스템에서의 자기전기효과에 관한 정량적인 연구가 부족한 상황이다.

이 학위논문에서 나는 $Fe_3O_4$ 나노 입자와 $Cu^{2+}$ ($S$=1/2) 이온이 들어간 새로 발견된 자기전기 물질인 $PbCu_3TeO_7$ 와 $Cu_3TeO_6$ 에 집중하였다. 처음으로, 절연물질에 넣은 3 나노미터에서 15 나노미터에서의 일정한 직경의 구형 $Fe_3O_4$ 나노 입자에서, 민감한 자기전기 감수율 측정장비를 이용하여 정량적인 자기전기효과를 연구하였다. 본질적인 자기전기 감수율이 측정되었으며, 직경 15 나노미터에서 5 K 에서 최대값 0.6 ps/m가 측정 되었다. 나노 입자의 직경을 줄임에 따라서, 자기전기 감수율이 점점 줄어들다가 5 나노미터 아래에서 사라지는 것을 발견하였는데, 이것은 Verwey 전이가 사라지는 직경인 6 나노미터와 비슷하다. 또한, 나노 입자의 직경을 줄임에 따라, 자기전기 감수율이 사라지는 전이 온도는 벌크에서는 9.8 K 이다가 7 나노미터에서는 19.7 K 으로 점점 높아졌으며, 이 현상은 코어쉘 효과를 보여준다.

또한 나는 $Cu^{2+}$ ($S$=1/2) 이온이 들어간 계산모양 카고메 구조를 가진 $PbCu_3TeO_7$ 에서 자기장에 의해 전기 분극이 나타나는 현상을 연구하였다. 이 물질은 이방적인 자기교환 상호작용과 스핀 쩔쩔맴으로 인해 $T_{N1}$=35 K 와 $T_{N2}$=24 K 두 개의 Neel 온도를 가진다. $T_{N2}$ 아래에서 자

기장이 c 방향으로 8.3 T 이상 걸었을 때, a 방향 전기 분극이 15 $\mu C/m^2$ 까지 생겼으며, 이것은 자화율 데이터를 보았을 때 스핀플롭 전이가 생겨하는 자기장에서 일어난다. 또한 자기장을 a 방향으로 걸었을 때, 14 $\mu C/m^2$ 의 전기 분극이 15 T 에서 생겨났다가 38 T 에서 사라졌다. 몬테카를로 계산 결과 두 가지 반자성 정렬을 함을 알 수 있었는데, $T_{N1}$ 아래에서는 사인파 모양의 정렬을 하다가, $T_{N2}$ 아래에서는 부정합한 나사형 스핀 회전을 가진다. 또한 계산결과는 a 와 c 방향으로 자기장을 걸었을 때 ab면에서 나선형 정열을 하며, 자기장 a 방향에서는 스핀 회전면이 bc면으로 바뀌는 전이가 추가로 존재함을 보여준다. 실험결과와 이론계산 결과를 이용하여 각각의 자기장에 따른 상평형도를 그릴 수가 있다.

마지막으로 나는 $Cu^{2+}$ ($S$=1/2)가 들어간 물질 중에서 처음으로 발견된 선형 자기전기물질인 $Cu_3TeO_6$ 에서의 자기전기 효과를 연구하였다. Neel온도 62 K 아래에서 전기 분극은 자기장에 따라 선형으로 증가하며, 자기장의 방향이 바뀌어도 전기 분극 방향은 바뀌지 않는다. 공간반전대칭 깨어져 있는 스핀구조는 이 물질에서 선형자기전기효과가 나타나는 이유를 설명하여 준다.

이 결과들은 새로운 측정 방법을 제안하고, 새로운 자기전기 물질을 발견함으로써, 자기전기효과 연구분야에서 새로운 후속연구의 장을 열었다는 점에서 의미가 있다.

주요어 : 자기전기성체, 강 자성체, 나노입자, 자기 쩔쩔맴, $S$=1/2 스핀, 선형 자기전기성체

학번 : 2010 - 23148